Fundamental analysis and optimization of barrier-pumped GaAs-based VECSELs

Dissertation

Zur Erlangung des Doktorgrades der Naturwissenschaften

(Dr. rer. nat.)

dem

Fachbereich Physik
der Philipps-Universität Marburg

vorgelegt von

Christoph Möller

aus

Hildesheim (Deutschland)

Marburg/Lahn, 2016

Vom Fachbereich Physik der Philipps-Universität Marburg

als Dissertation angenommen am:

Erstgutachter:	Prof. Dr. Wolfgang Stolz
Zweitgutachter:	Prof. Dr. Martin Koch

Tag der mündlichen Prüfung:

Hochschulkennziffer 1180

Zusammenfassung

Im Jahr 1960 berichten T. H. Maiman et al. von dem ersten Laser, ein mit einer Blitzlampe optisch gepumpter Rubinlaser [1]. Die Demonstration dieses ersten Lasers war ein großer Erfolg für ein neues Wissenschaftsgebiet. Noch im selben Jahr wird der elektrisch gepumpte Helium-Neon-Laser demonstriert, der auch heute noch in Laboren zu finden ist und oft als Beispielmodell in Vorlesungen präsentiert wird [2]. Im weiteren Verlauf der 60er Jahre rücken auch Halbleiterlaser immer mehr in den Fokus. Pionierarbeit leisten hier H. Krömer und Z. I. Alferov, die die Entwicklung von Halbleiterlasern mit Doppelheterostruktur nachhaltig geprägt haben und dafür im Jahr 2000 den Nobelpreis erhielten [3]. Die nächste Entwicklung bei den Halbleiterlasern war die Realisierung von Quantenfilmen als optisches Gewinnmedium in den 70er Jahren [25]. Dieser Entwicklungsschritt war zudem auch eng mit den großen Fortschritten in der Wachstumstechnologie von Halbleiterschichten verknüpft. Im Jahr 1975 wird schließlich der erste optisch gepumpte Quantenfilm-Laser von J. P. van der Ziel realisiert [4]. Das Gewinnmedium beinhaltet dabei 50 GaAs/(AlGa)As Quantenfilme, musste zu der Zeit aber noch auf 15 K gekühlt werden und das Erreichen der Laserschwelle erforderte hohe optische Pumpintensitäten von 36 kW/cm^2. Erste elektrische Quantenfilm-Laser wurden ebenfalls in den 70er Jahren demonstriert, hier lag der Schwellenstrom aber bereits in Größenordnungen, die nicht fernab von heutigen Lasern sind.

Bis heute wurden Halbleiterlaser stetig weiterentwickelt. Insbesondere konnten nicht nur die Laserschwelle, -Effizienz und Ausgangsleistung verbessert werden, sondern es wird mittlerweile auch ein sehr großer Wellenlängenbereich durch Halbleiterlaser abgedeckt, der sich vom ultravioletten über den gesamten sichtbaren und nah- bis ferninfraroten Bereich erstreckt. Weiterhin wird heutzutage mit Diodenlasern ein Massenmarkt bedient. Sie sind, oft unmerklich, in den Alltag integriert. Typische Anwendungen finden sich in Computermäusen, in Bar-Code-Scannern, in CD-, DVD- oder Blu-ray-Laufwerken und in Smartphones [6]. Hervorzuheben ist allerdings die Verwendung als Transmitter in glasfasergestützten Netzwerken für Telekommunikation und Datentransfer. Der mit Abstand am weitesten verbreitete Halbleiterlaser ist der VCSEL (englisch: vertical-cavity surface-emitting laser). Im Jahr 2014 wird die Zahl der verkauften VCSEL, seit der Erfindung in den 80ern, auf über eine Milliarde geschätzt [7].

Das Akronym VCSEL beschreibt wesentliche Merkmale dieses Lasers. Gleichzeitig dient es als Abgrenzung von einem Kantenemitter, bei dem die Laser-Strahlung in der Ebene der Quantenfilme propagiert und senkrecht zu den Bruchkanten der Halbleiterstruktur austritt. Ein VCSEL besitzt hingegen monolithisch gewachsene Laserspiegel, die einen Resonator (Kavität) senkrecht, bzw. vertikal, zu den Quantenfilmebenen bilden. Die Laserstrahlung tritt demzufolge vorzugsweise aus der Oberfläche anstatt aus den Kanten der Struktur aus.

Diese Arbeit befasst sich mit einem dem VCSEL sehr ähnlichen Laser, dem VECSEL (englisch: vertical-external-cavity surface-emitting laser). Im Vergleich zum VCSEL besitzt der VECSEL nur einen monolitisch gewachsenen Spiegel. Der nun fehlende zweite Resonatorspiegel wird dafür durch einen externen Laserspiegel ersetzt. Zudem werden die meisten VECSEL mittels eines anderen Lasers optisch gepumpt. Die resultierende Anordnung entspricht somit der eines Scheibenlasers, weswegen der VECSEL alternativ auch oft SDL (englisch: semiconductor disk laser) oder OPSL (english: optically pumped semiconductor laser) genannt wird [8, 9].

Auch wenn VECSEL bereits kommerziell erhältlich sind, ist der Markt bei weitem nicht vergleichbar mit dem der VCSEL. Gründe dafür sind unter anderem höhere Produktionskosten und das durch die Erfordernis des Pumplasers auch komplexere und größere Produkt. Dafür hat der VECSEL aber andere vorteilhafte Eigenschaften, die sich in einzigartiger Weise kombinieren lassen. Beispielsweise eröffnen sich vielfältige Möglichkeiten durch den externen Resonator. Zum einen können Variationen der Spiegel genutzt werden, um den Laserstrahl in seiner Strahlqualität zu optimieren. Andererseits können aber auch optische Elemente in dem Resonator arrangiert werden, wie etwa doppelbrechende Filter, um schmale Linienbreiten zu erzwingen, nichtlineare optische Kristalle für die hocheffiziente intra-kavitäre Frequenzverdopplung oder auch sättigbare Absorber-Spiegel für Modenkopplung. Diese Vielfalt trifft nun auf den bereits erwähnten großen Wellenlängenbereich, der durch Halbleiterlaser erreicht wird. Entsprechend wurde seit der ersten Demonstration des VECSELs im Jahr 1997 von M. Kuznetsov et al. [10] eine Vielzahl unterschiedlicher VECSEL Systeme präsentiert. Einen sehr guten Überblick über die bisher realisierten Emissionswellenlängen und Lasereigenschaften geben die bereits (zu unterschiedlichen Themen) erschienenen Reviews [8–9, 11–14].

In Abhängigkeit von der Anwendung ist die Erfordernis der optischen Pumpquelle im Gegensatz zu elektrischem Pumpen nicht zwingend ein Nachteil. Ein VECSEL kann als ein Konverter von dem Pumplicht zu der eigentlich emittierten VECSEL Strahlung gesehen werden. Diese Umwandlung betrifft aber nicht nur die Strahlqualität oder beispielsweise die Linienbreite, sondern insbesondere auch die Wellenlänge. Dies ermöglicht die Wahl eines Pumplasers, der nicht zwingend eine bestimmte Wellenlänge besitzen muss, aber dafür kosteneffizient sein kann. Eine ausgereifte und kosteneffiziente Lasertechnologie ist beispielsweise in Form von (AlGa)As/GaAs Diodenlasern mit einer Emissionswellenlänge bei 808 nm verfügbar. Viele der bisher erforschten VECSEL sind daher auf diese Pumpwellenlänge optimiert.

Um einen effizienten Laser zu erhalten, muss ein möglichst großer Teil des Pumplichts von dem VECSEL Chip absorbiert und in Ladungsträger umgewandelt werden, die dann für den Laserprozess zur Verfügung stehen. Durch die geringe Schichtdicke von nur einigen Nanometern absorbieren die Quantenfilme allerdings nur einen Bruchteil des Pumplichts. Das führt zu dem häufig verwendeten Prinzip des Barrierepumpens, also des Pumpens der Schichten, welche die Quantenfilme umschließen und um ein vielfaches dicker als die Quantenfilme sind. Die Bandlücke des Barrierenmaterials kann zudem so gewählt werden, dass eine hinreichende Absorption des Pumplichts vorhanden ist. Mit dieser Methode konnte beispielsweise eine Lasereffizienz von 60 % erreicht werden [15]. Der alternative Ansatz, das direkte Pumpen der Quantenfilme, ist also mit einer deutlich geringeren Lasereffizienz verbunden und wurde daher auch weitaus weniger erforscht [8, 16–18].

In der vorliegenden Arbeit, werden 808 nm barrierengepumpte VECSEL auf GaAs-Basis untersucht. Ein etabliertes Quantenfilmdesign ist das (GaIn)As/GaAs Materialsystem. Hiermit wurden bisher Emissionswellenlängen zwischen 920 nm – 1.2 µm realisiert. Dieser Bereich ist allerdings auf der kurzwelligen und langwelligen Seite fundamental begrenzt. Je kurzwelliger die Emissionswellenlänge etwa wird, desto flacher werden die Potentialtöpfe für die Elektronen und Löcher in den Quantenfilmen. Dies kann zu einer erheblichen Reduktion der Ladungsträgerlebensdauer führen, die dann nicht mehr strahlend über den Laserübergang rekombinieren. Auf der langwelligen Seite ist das System hingegen durch die Kristallverspannung begrenzt, die das Wachstum von hochqualititativen Quantenfilmen nur bis zu einer gewissen Indiumkonzentration ermöglicht.

Ziel dieser Arbeit ist die Optimierung von VECSELn in drei verschiedenen Wellenlängenbereichen aus dem genannten Spektrum zwischen 920 nm – 1.2 µm. Zunächst werden dafür VECSEL bei 1 µm Emissionswellenlänge untersucht. Bei dieser Wellenlänge wurden die effizientesten und leistungsstärksten VECSEL demonstriert. Die Rekordausgangsleistung liegt bei über 100 W [20, 21]. Die maximale Ausgangsleistung bei 920 nm hingegen ist 12 W [15], und bei 1180 nm 50 W [19]. Daher dient die bereits ausführlich untersuchte Schichtkonfiguration für 1 µm Emissionswellenlänge in dieser Arbeit als Referenz. In Kapitel 2 werden hierfür zunächst die Grundlagen des VECSELs zusammengefasst. Anschließend, in Kapitel 3, wird ein experimentelles Analyseverfahren entwickelt, um eine vollständige Charakterisierung von VECSEL Chips zu ermöglichen. Eine besondere Größe eines VECSELs ist das sogenannte Detuning. Kapitel 3 widmet sich ebenfalls der experimentellen Bestimmung dieses Parameters anhand von temperaturabhängigen Reflexions- und Photolumineszenzmessungen. Der Einfluss des Detunings auf die Lasereffizienz wird insbesondere in Kapitel 4 untersucht. Hierfür wird ein Experiment entwickelt, in dem das Detuning gezielt manipuliert werden kann. Mit einer für dieses Experiment ausgewählten Probe wird so der starke Einfluss des Detunings auf die Lasereffizienz quantifiziert.

Kapitel 5 befasst sich mit VECSELn für Emissionwellenlängen zwischen 920 nm – 950 nm. Dafür werden zwei verschiedene Quantenfilmdesigns und die damit verbundenen Quantentopftiefen diskutiert und experimentell untersucht. Der entscheidende Parameter, bei dem sich die Designs unterscheiden, ist daher die Zusammensetzung der Barriere. Als Resultat können leistungslimitierende Faktoren identifiziert werden, auf dessen Grundlage in Zukunft optimierte VECSEL für diesen Wellenlängenbereich realisiert werden können.

Der letzte Teil der Arbeit, Kapitel 6, befasst sich mit VECSELn für Emissionswellenlängen um 1.2 µm. Im Speziellen wird hier ein Typ-II Quantenfilmdesign untersucht, das sogar Emissionswellenlängen über 1.4 µm ermöglicht. In einem solchen Design sind Elektronen und Löcher räumlich voneinander getrennt. Das hier vorgestellte Design besteht aus zwei (GaIn)As Quantenfilmen, die einen Ga(AsSb) Quantenfilm umschließen. Der Verlauf des Leitungsbands über die drei Quantenfilme gleicht einem „W", worin der Name „W"-Quantenfilm seinen Ursprung hat. Dementsprechend ist die Aufenthaltswahrscheinlichkeit der Elektronen in den beiden äußeren (GaIn)As Quantenfilmen konzentriert, wohingegen sie im mittleren Ga(AsSb) Quantenfilm deutlich reduziert ist. Genau der gegenteilige Verlauf liegt im Valenzband vor, d.h. die Aufenthaltswahrscheinlichkeit der Löcher ist in dem Ga(AsSb) Quantenfilm konzentriert. Insgesamt ist aber ein ausreichender Überlapp der Elektron- und Lochwellenfunktionen vorhanden, sodass die Ladungsträger bildlich gesprochen über die Grenzfläche der Quantenfilme rekombinieren können. Die Energie dieses räumlich indirekten Übergangs ist aber, wie in Kapitel 6 gezeigt wird, deutlich kleiner als die der direkten Übergänge in den separaten Quantenfilmen. Dieses Prinzip ermöglicht es, Materialien mit großer Bandlücke zu kombinieren, um eine langwellige Emission zu erhalten. Das Konzept ist besonders attraktiv für Emissionswellenlängen im mittleren Infrarotbereich, für den es ursprünglich auch konzipiert wurde. Obwohl bereits einige Laser mit solch einem Quantenfilmdesign demonstriert wurden, ist dessen Anwendung für VECSEL noch unerforscht. Der erste VECSEL mit dem beschriebenen Quantenfilmdesign wird in dieser Arbeit demonstriert. Die Methoden aus Kapitel 3 werden angewandt, um das neue Lasersystem vollständig zu charakterisieren. Es wird offengelegt, dass ein Typ-II VECSEL fundamental andere Funktionsmechanismen im Vergleich zu Typ-I VECSELn besitzt. Dies bezieht sich insbesondere auf die Abhängigkeit der Lasereffizienz vom Detuning. Das Ergebnis des Kapitels sind Optimierungsvorschläge für künftige Typ-II VECSEL, mit denen die Entwicklung effizienter Typ-II VECSEL mit Emissionswellenlängen über 1.2 µm als erfolgversprechend angesehen werden kann.

Danksagung

Ich möchte mich an dieser Stelle ganz herzlich für die Unterstützung bedanken, die ich während meiner Promotionszeit erhalten habe.

Ganz besonderer Dank gilt meinen beiden Betreuern, die eine der wichtigsten Voraussetzungen für solche Arbeiten geschaffen haben: Arbeitsgruppen in denen man gerne arbeitet und in denen es grundsätzlich an nichts mangelt. Prof. Dr. W. Stolz danke ich dafür, dass er mir direkt nach der Masterarbeit den Einstieg in die Promotion ermöglicht hat und mir die Möglichkeit gab, diese spannenden Projekte zu bearbeiten. Prof. Dr. M. Koch unterstützte mich bereits seit meiner Bachelorarbeit im Jahr 2010 und hat mir ebenso den Auslandsaufenthalt in den USA im Jahr 2012 zur Masterarbeit ermöglicht.

Außerdem möchte ich mich bei Prof. Dr. S. W. Koch und Prof. Dr. C. von Hänisch bedanken, die sich, ohne zu zögern, bereit erklärt haben, die Prüfungskommission zu vervollständigen.

Auch den Erfahrungen und Erkenntnissen vor der Promotionszeit kommt eine gewisse Bedeutung zu. Die Erfahrungen aus der Zeit am Optical Science Center in Tucson, Arizona, haben mir während der Promotion sehr geholfen, wofür ich Dr. Maik Scheller, Dr. Alexandre Laurain und Prof. Dr. J. Moloney danken möchte. Besonderer Dank gilt auch Dr. Bernardette Kunert und Dr. Bernd Heinen, die mich im Jahr 2012 in das Gebiet der VECSEL eingeführt haben und mir auch später noch mit Rat zur Seite standen, obwohl Sie das Institut inzwischen verlassen hatten.

Unmöglich ist eine solche Arbeit ohne die Kolleginnen und Kollegen. Hier sind insbesondere Antje Ruiz Perez von der NAsP III/V GmbH und Christian Fuchs, die Experten von der MOVPE, zu nennen. Ihre Tätigkeiten gehen weit über die Herstellung von Halbleiterschichten (mit ausgezeichneter Qualität!) hinaus. Mit Antje hatte ich seit Beginn der Promotion etliche erhellende Diskussionen, die immer einen Fortschritt mit sich gebracht haben. Dies bezieht sich insbesondere auch auf die Untersuchungen der 930 nm VECSEL. Gleiches gilt für Christian, der viele Überstunden in das Wachstum der Typ-II Strukturen investiert hat und mit seinem guten, kritischen Blick jedes Vorhaben bereichert.

Ebenso wichtig für die Umsetzung der Typ-II Laser war die theoretische Arbeit von Dr. Christian Berger. Die Wechselwirkung zwischen Experiment und Theorie über die „Schnittstelle“ Christian hat mir nicht nur sehr viel Freude bereitet, sondern hat auch anstehende Experimente motiviert, spannender gemacht und die Arbeit so erleichtert.

Während meiner Promotionszeit habe ich eine Vielzahl von VECSEL Chips prozessiert, was einen erheblichen zeitlichen Aufwand bedeutete. Ohne die technische Hilfe von Stefan Reinhard und die tatkräftige Unterstützung von Ulrike Häuplik wäre der zeitliche Aufwand noch um einiges höher gewesen. An dieser Stelle möchte ich mich auch bei den restlichen Kollegen vom STRL bedanken, die immer hilfsbereit sind.

Neben den in meiner Dissertation verfassten Themen hatte ich auch die Freude, an anderen Projekten mitwirken zu dürfen. Besonders bedanken möchte ich mich bei Dr. Mahmoud Gaafar und Max Vaupel für die Zusammenarbeit auf dem Gebiet der selbst-Modengekoppelten VECSEL, sowie bei Fan Zhang für die Zusammenarbeit auf dem Gebiet der Single-Frequency VECSEL und der intrakavitären Frequenzkonversion. Mit Fan Zhang zusammen habe ich im Übrigen das Experiment zur Untersuchung des Detunings entwickelt. Die gemeinsame Arbeit und Zeit auf der Konferenz in San Francisco wird mir positiv in Erinnerung bleiben. Auch die gemeinsamen

Diskussionen über die Messungen des zeitlich aufgelösten Gewinns an VECSELn mit Christian Lammers und Markus Stein waren sehr spannend.

Dankbar bin ich auch Dr. Jan Balzer und Alexander Kalinger, mit denen ich den Messplatz zur Charakterisierung des optischen Gewinns in Halbleiterlasern entwickelt habe. Es war mir eine Freude, die Masterarbeit von Alex zu betreuen. Gleiches gilt auch für Sascha Kress, dessen Bachelorarbeit ich betreuen durfte.

Bezüglich des universitären Umfelds möchte ich mich auch noch bei Dr. Arash Rahimi-Iman bedanken, der die VECSEL-Aktivitäten am Renthof erfolgreich lenkt, sowie voranbringt und auch mir mit einigen Diskussionen eine Hilfe war. Auch die Kollegen aus der Spektroskopie waren mir eine Hilfe, wie etwa mein ehemaliger Büro-Kollege Dr. Stefan Busch, aber auch Sina Lippert, Dr. Steffen Schumann, Marina Gerhard, Dr. Khaled Shakfa, David Jahn, Ralf Gente, Stefan Sommer, Arno Rehn, Amin Soltani und Eva-Maria Stübling.

Für die administrative Unterstützung bedanke ich mich bei Maya Strobel, Anne Ehlers und Elke Vaupel.

Zuletzt möchte ich mich bei meiner Familie bedanken, die mich immer unterstützt hat. Auch wenn die Anzahl der Studienabschlüsse und Promotionen allgemein über die letzten Jahre gestiegen ist, ist es nicht selbstverständlich, diesen Weg gehen zu können. Insbesondere danke ich daher meinen Eltern, und meinem Bruder, die mich vor allem im Studium aus voller Überzeugung unterstützt haben. Ich freue mich, dass ihr mir diesen Weg ermöglicht habt.

Besonderer Dank gebührt auch meinem Onkel, Christian Pfitzner, ohne den ich im Wintersemester 2007 vielleicht gar nicht in Marburg gelandet wäre. Auch er hat mich stets in meinen Zielen bestärkt und seit dem Studienbeginn unterstützt.

Der letzte Dank gilt meiner Freundin, Christina Salland. Sie war immer da und hat mir immer den Rücken freigehalten, wenn es mal stressig wurde. Das hat mir vieles erleichtert. Ich hoffe, dass ich dir das während deiner Promotionszeit zurückgeben kann.

Contents

1. Introduction ... 1

2. Physics of VECSELs ... 5
   2.1 Operation principle ... 5
   2.2 VECSEL chip structure ... 6
      Distributed Bragg reflector ... 7
      Longitudinal confinement factor ... 9
      Material gain ... 10
      Modal gain and threshold condition ... 12
      Detuning ... 12
   2.3 Thermal management ... 14
   2.4 Resonator geometries and operation modes ... 19

3. Methods of fundamental VECSEL studies ... 21
   3.1 Reference Sample ... 22
   3.2 Laser power curves ... 23
   3.3 Determination of the detuning ... 25
      Reflectance measurements ... 25
      Reflectance and longitudinal confinement factor simulation ... 28
      Edge photoluminescence measurements ... 29
      Detuning summary ... 32
   3.4 Quasi-equilibrium gain measurements ... 33
   3.5 Thermal resistance measurement techniques ... 37
      Shift-rate method ... 38
      Roll-over method ... 40
      Virtual roll-over method ... 41
   3.6 Summary ... 42

4. Detuning dependent performance of quantum well VECSELs ... 45
   4.1 Basic theoretical considerations ... 48
   4.2 Experimental study of the detuning dependent performance ... 50
   4.3 Summary ... 57

5. The development and characterization of VECSELs with novel emission wavelengths....... 59
5.1 Quantum well design 60
5.2 VECSEL samples 63
5.3 Laser studies 65
5.4 Detuning studies 68
5.5 Gain measurements 73
5.6 Summary and outlook 76

6. Properties of type-II VECSELs 79
6.1 Type-II quantum well design 80
6.2 Photoluminescence studies 82
6.3 VECSEL design and samples 87
6.4 Detuning studies 89
6.5 Laser studies 94
Wavelength dependence, thermal resistance, and thermal roll-over 97
Detuning dependences of a type-II VECSEL 100
High beam quality TEM_{00} mode operation 104
6.6 Summary and outlook 106

7. Summary and outlook 109

Bibliography 113

List of contributions 121
Publications 121
Conferences 122

List of acronyms

BQW	bilayer quantum well
BRF	birefringent filter
CVD	chemical vapor deposition
CBO	conduction band offset
DBR	distributed Bragg reflector
ECHS	extra-cavity heat spreader
FEM	finite elements method
FWHM	full width at half maximum
HR-XRD	high-resolution X-ray diffraction
ICHS	intra-cavity heat spreader
LCF	longitudinal confinement factor
MBE	molecular beam epitaxy
MOVPE	metalorganic vapor-phase epitaxy
MQW	multiple quantum well
PL	photoluminescence
PR	photomodulation reflectance
QD	quantum dot
QW	quantum well
RPG	resonant periodic gain
SAM	saturable absorbing mirror
SDL	semiconductor disk laser
SNR	signal-to-noise ratio
SQW	single quantum well
TDR	temperature dependent reflectance

TEM transverse electromagnetic

VBO valence band offset

VCSEL vertical-cavity surface-emitting laser

VECSEL vertical-external-cavity surface-emitting laser

1. Introduction

The first laser, built from a flash lamp pumped ruby, was reported in 1960 by T. H. Maiman [1]. Its demonstration was a great success in an emergent research field. In the end of the same year, the demonstration of the more popular helium neon laser followed, which is still found in many laboratories or used as a practical laser model in lectures [2]. Still in the 60's, also attention is drawn to semiconductor lasers. Pioneering work was performed by H. Krömer and Z. I. Alferov who obtained the Nobel prize for the development of the double heterostructure diode lasers [3]. Then, in the 70's, it was realized that the semiconductor lasers could be significantly improved, if quantum wells (QWs) are employed as gain media. However, the underlying physical mechanisms were not well known and subject of ongoing research. Especially, the growth of QWs and the therewith connected development of the epitaxy was a challenge. The next milestone in the development of semiconductor lasers was accompanied by the research on epitaxy techniques. In 1975, the first optically pumped QW laser was demonstrated by J. P. van der Ziel et al. [4]. The laser gain region comprises 50 GaAs/(AlGa)As QWs and had to be cooled to a temperature of 15°K in order to achieve threshold with pump intensities of 36 kW/cm². First electrical pumped devices were also demonstrated at the end of the 70's. For instance, in 1979, room temperature operation was reported with a single QW as gain medium and with a threshold current of 2 kA/cm² by Tsang et al. [5].

To date, QW lasers have been steadily improved concerning the thresholds, output powers, power consumption, and also concerning the range of accessible emission wavelength. Laser operation has been demonstrated from the ultraviolet, to the optical, near- and mid-infrared wavelength regime. In particular, diode lasers have become a mass product and are found in many everyday life's electronics. For example, they are used for sensors in computer mice, barcode scanners, CD, DVD or Blu-ray disk drives, and smartphones [6]. However, the most important application today is their utilization as transmitters in fiber-optic communications, which satisfies the need for the transmission of high data volumes. The by far widest spread diode laser is the vertical-cavity surface-emitting laser (VCSEL). In 2014 it was estimated that the number of sold VCSELs, since its invention in the late 80's, has passed the one billion mark [7].

The term VCSEL is related to its basic operation principle and its differentiation to edge emitting diode lasers. In an edge-emitter, the laser resonator is formed by inherently existing edges of the cleaved semiconductor structure. Consequently, the directionality of the laser is in the plane of the QWs and perpendicular to these edges. In contrast, the VCSEL comprises monolithically grown high reflective laser mirrors, which form a laser *cavity* perpendicular, or *vertical*, to the QW planes. The laser light is emitted from the *surface* instead from the edges.

This thesis is dedicated to a very similar kind of semiconductor laser, namely the vertical-*external*-cavity surface-emitting laser (VECSEL). In comparison to a VCSEL, one of the monolithic laser mirrors is removed and replaced by an external mirror. Moreover, VECSELs are optically pumped, resulting in a scheme which is similar to other solid state disk lasers. Accordingly, the VECSEL is also often referred to as semiconductor disk laser (SDL), or optical-pumped semiconductor laser (OPSL) [8, 9].

Although VECSELs are also commercially available, the market is not comparable to the above-mentioned scale in case of VCSELs. The reasons are essentially higher manufacturing costs and more specific fields of application. Instead, a VECSEL can provide a unique, highly specialized laser source, optimized for a desired application. Since the first demonstration of the VECSEL in

1997 by Kuznetsov et al. [10], several reviews and text books have been published, which summarize the achieved results in these fields [8, 9, 11–14]. Owing to the external cavity, it combines the great wavelength versatility of semiconductor lasers with outstanding properties of other solid state lasers. Examples are their high beam quality with almost ideal circular beam profile, or a low intensity noise. Moreover, the intra-cavity elements can be used to manipulate the VECSELs operation mode. Birefringent filters can be applied to force single-frequency operation, saturable absorbing mirrors for mode-locking, or nonlinear crystals for highly efficient intra-cavity frequency conversion. Selected highlights of these results will also be presented at the relevant sections in the course of this thesis.

As mentioned, a VECSEL is usually optically pumped. Depending on the application, the requirement of an additional pump source in comparison to electrical pumped diode lasers is not necessarily a disadvantage. A VECSEL can also be regarded as a converter between the pump light and the actually emitted VECSEL light. This kind of conversion cannot only involve the above-mentioned features, like a rectification of the beam quality or intensity noise of a pump laser, mode-locking or single-frequency operation. More importantly, also the emission wavelength of the pump laser can be converted. This enables the application of a pump device, which is not necessarily bound to a specific wavelength, but cost-efficient. A mature and cost-efficient laser technology is for instance provided by fiber-coupled GaAs/Al(GaAs) laser diodes with emission wavelength at 808 nm and which is used for most VECSEL devices.

However, to obtain an efficient device, a strong absorption of the pump light is required, which is not provided by the absorption of the thin quantum wells. Instead, a high absorption can be provided by the barriers which enclose the QWs. This concept is called barrier-pumping, accordingly, and turned out to be very effective. At room temperature operation optical input to output efficiencies close to 60 % are achieved [15]. The opposite concept, namely “in-well” pumping, involves critically reduced laser efficiencies and, thus, is less attractive and has been studied to a smaller extent [8, 16–18].

In the present thesis, 808 nm barrier-pumped VECSELs on GaAs-substrates are investigated. A QW design for these devices is the well-explored (GaIn)As/GaAs system. The functionality, physics and capabilities of these devices are introduced in chapter 2. In fundamental operation, i.e. without intra-cavity frequency conversion, the accessible wavelength range with this material system reaches from 920 nm to 1.2 µm [15, 19]. However, close to the borders of this range, the output powers are significantly impaired due to fundamental limitations. At 1 µm, the most powerful VECSELs have been reported, so far. Output powers in excess of 100 W could be achieved [20, 21]. In contrast, a maximum output power of 12 W is achieved at 920 nm [15] and an output power of 50 W at 1180 nm [19]. Interestingly, there are no reports of (GaIn)As/GaAs VECSELs emitting either below 920 nm, or beyond 1.2 µm. The interest in efficient devices in the mentioned wavelength range, is primarily driven by highly efficient intra-cavity frequency-doubling, which gives access to Watt level output powers in the visible range. So far, output powers in the order of 20 W can be achieved with VECSELs emitting green and yellow wavelength [22, 23]. Nevertheless, due to the restriction of the fundamental emission from the (GaIn)As/GaAs QWs, there is still a lack of high-power devices in the blue and red. In this thesis, it is investigated how VECSELs can be optimized to provide more powerful devices in the future.

VECSELs from three regimes within the mentioned wavelength range are investigated in chapters 3 – 6. A mature 1 µm emitting sample used is to demonstrate the experimental methods for fundamental studies on VECSELs (chapter 3). The methods comprise the evaluation of laser

power curves and spectra, detailed structural studies using photoluminescence and reflectance measurements, modal gain studies, and also thermal resistance analysis. Such complete study of a 1 µm sample yields a reference which enables detailed comparisons to the samples at other wavelengths, also applying other design concepts (chapters 5 and 6). Accordingly, these studies will also be carried out for all other samples throughout the chapters 4 – 6.

One key parameter in VECSELs is the so called detuning (cf. chapter 2). Due to its importance, its influence is discussed and studied in chapter 4, also by means of a mature 1 µm emitting sample. The knowledge of its impact on the VECSEL's performance will also help to identify or exclude performance limitations in chapters 5 and 6.

Chapter 5 deals with the short-wavelength limitation of barrier-pumped GaAs-based VECSEL structures around 920 nm. It is discussed that the shallow QW depth is a factor which fundamentally limits the material gain, as charge carriers can be thermally reemitted from the QWs into the barriers. Possible QW designs for emission wavelength between 920 nm – 950 nm are discussed. The performances and properties of VECSELs with the discussed designs are studied and compared to the 1 µm emitting reference sample.

The other border of accessible wavelength with the (GaIn)As/GaAs system is at the wavelength of about 1.2 µm. Indeed, an excellent confinement potential is found here, but it is the crystal strain which sets stringent limitations to the growth of the QWs. An alternative QW design on GaAs substrates and for the emission at 1.2 µm and beyond is provided by a type-II QW. In such a QW, electrons and holes are spatially separated. If designed appropriately, their recombination happens across the material interfaces which causes a reduced transition energy in comparison to the materials band gaps. Although diode lasers based on type-II QW designs have already been realized and studied, this concept is not explored yet for the application in VECSELs. Instead, other approaches have been followed in the past, such as (GaIn)(NAs)/GaAs QWs or QDs. In chapter 6, the approach with type-II QWs is studied by means of the (GaIn)As/Ga(AsSb)/GaAs system. The design is discussed in detail and preliminary photoluminescence studies are carried out to evaluate the potential for the use as gain medium. Afterwards, the first type-II VECSEL is demonstrated and studied by the methods from chapter 3.

Overall, this thesis presents novel design concepts to increase the already stunning wavelength range of VECSELs even further.

2. Physics of VECSELs

Since the first demonstration of a VECSEL, many different reviews and text books have been published which address the underlying laser physics. A basic understanding of the VECSEL functionality can be obtained from the review by Tropper and Hoogland [11] as well as the text book by O. G. Okhotnikov [8]. This literature also contains excerpts of the fundamental semiconductor laser physics from more general text books by L. A. Coldren et al. [24] as well as P. S. Zory [25]. This chapter provides an overview based on this literature about the physics of VECSELs with focus on the topic of the present thesis. In the first section 2.1, the basic elements of a VECSEL are introduced. The exact composition and functionality of a VECSEL chip is treated in the second section 2.2. More emphasis is given to the concept of a barrier-pumped resonant periodic gain medium (section 2.3) and the thermal resistance of flip-chip bonded VECSELs (section 2.4). The last section 2.5 serves as an overview about the different operation modes of a VECSEL, which are mainly obtained by a manipulation of the external cavity or therein placed optical elements.

2.1 Operation principle

The operation principle of a VECSEL can be understood by means of Fig. 2.1. The illustrated arrangement is very similar to what is often used in the existing literature and what is also applied in most of the experiments throughout this thesis. As every laser, the VECSEL is composed of three fundamental elements, namely a pump source, a gain medium and a resonator. Most VECSELs are driven by an optical pump source. In the present work, fiber-coupled 808 nm diode lasers are used which deliver high optical powers at relatively low expenses. The pump laser's fiber is attached to a pump optics which essentially consists of a collimation and a focusing lens. In this way, the pump beam is focused onto the VECSEL chip. The pump spot size can be well approximated by the relation $d = d_f f_1/f_2$, where f_1 and f_2 are the focal lengths of the focusing and collimation lens and d_f is the fiber diameter, respectively. Typical fiber diameters of commercially available devices range from 100 µm to 600 µm, depending on the power capabilities of the module. With typical focal lengths of < 10 cm, the usual pump spot sizes range from tens of micrometers to even one millimeter. The VECSEL chip is placed right at the focus of the pump beam. It has a twofold function and serves as gain medium as well as highly reflective resonator mirror at the same time. The resonator is terminated by at least one external mirror, which can be arranged as illustrated in

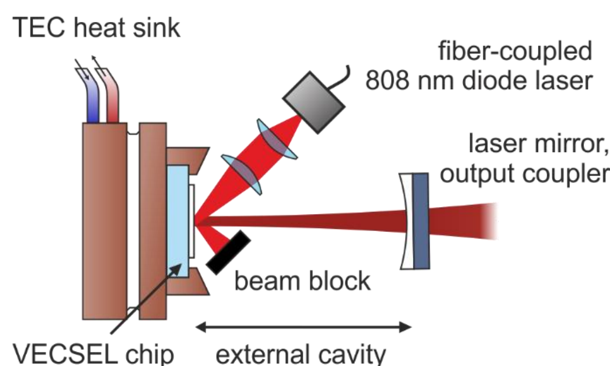

Figure 2.1. Scheme of an optically pumped VECSEL which is arranged in a linear cavity.

Fig. 2.1, to form a linear cavity. However, it is also possible to employ more than one external mirror in different arrangements, such as a V-shaped or Z-shaped cavity. Only a part of the pump light contributes to the VECSEL's power curve. A considerable amount of about one third is only reflected from the chip. Also the absorbed light is not converted one-to-one into laser radiation, but a significant part is dispersed in radiative and non-radiative loss processes. The latter cause significant heat which makes the application of heat removal techniques necessary. In the arrangement of Fig. 2.1, the heat removal is implemented by a diamond heat spreader and a copper heat sink. The diamond heat spreader is part of the VECSEL chip and its function is discussed in more detail in section 2.3. The copper heat sink comprises Peltier elements which enable a temperature control and is connected to a water cycle. Depending on the applied pump powers, temperatures from -20°C to 100°C can be adjusted with this setup. The part of the input power, which is not dispersed by any loss processes, is converted into the output power of the VECSEL.

2.2 VECSEL chip structure

A more detailed view on the functionality of a VECSEL is obtained by Fig. 2.2, which shows a plot of the refractive index versus the growth direction for a typical GaAs-based device with an emission wavelength at about 1010 nm. The interface between air and the VECSEL chip is at the so-called cap layer. This layer is followed by the resonant periodic gain (RPG) and the distributed Bragg reflector (DBR).

Here, a (GaIn)P cap layer is shown which serves as an etch stop for the flip-chip processing, as will be described later. It is also substantial for the confinement of charge carriers in the active laser region. Moreover, its layer thickness has an impact on the standing wave light field within the RPG. The high refractive index contrast between the cap layer and air causes high Fresnel reflections. Due to the high reflectivity of the DBR, a micro-cavity is formed, in which a standing wave light field arises. The light field intensity is illustrated for the 1010 nm design wavelength (black), for 1005 nm (red), and 1000 nm (light red). Its anti-nodes coincide with the QW positions, but a significant wavelength dependence of the intensity is observed, which will be discussed later in more detail. Note that Fig. 2.2 shows only 7 of 22 DBR pairs for a better visibility of the RPG.

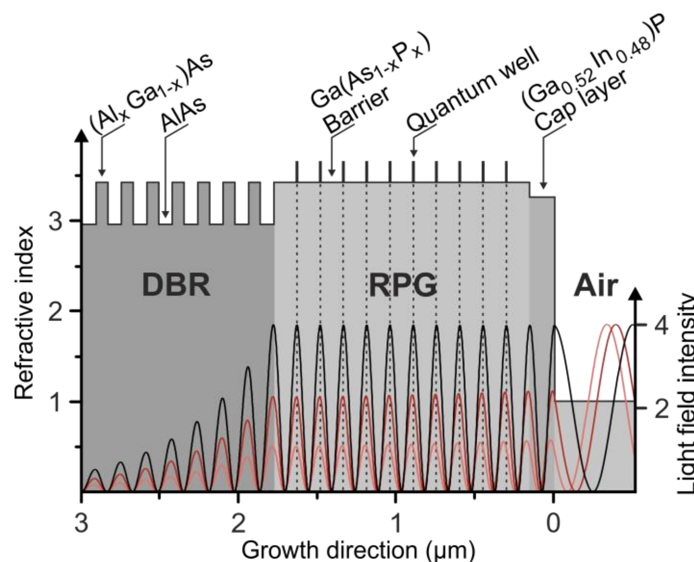

Figure 2.2. Close-up view on the VECSEL structure with the two segments DBR and RPG as well as the cap layer. The black, red and light red lines illustrate the standing wave light field intensity for the wavelengths 1010 nm (black), 1005 nm (red) and 1000 nm (light red).

Distributed Bragg reflector

The DBR consists of multiple layer pairs with alternating refractive index. The preferably high refractive index contrast between these individual layers causes Fresnel reflections at the interfaces. If the optical thickness is $\lambda/4$, which is also referred to as the Bragg-wavelength, the reflected waves interfere constructively. This can be exploited to obtain a high reflectivity. To calculate the resulting reflectivity, a transfer-matrix method can be applied [24]. For this, a forward and a backward propagating electric field $E_1^{+/-}$ is considered. The sign indicates the propagation direction. The transmission of the electric field $E_1^{+/-}$ through an optical element, such as an interface of a dielectric medium, can then be described as

$$\begin{pmatrix} E_2^+ \\ E_2^- \end{pmatrix} = \begin{pmatrix} T_{11} & T_{12} \\ T_{21} & T_{22} \end{pmatrix} \begin{pmatrix} E_1^+ \\ E_1^- \end{pmatrix} = \boldsymbol{M} \begin{pmatrix} E_1^+ \\ E_1^- \end{pmatrix} , \tag{2.1}$$

where $\boldsymbol{M}$ is the transfer-matrix for the respective optical element. For instance, the matrix for the transmission through a dielectric interface contains the respective Fresnel coefficients. The propagation through a dielectric medium, on the other hand, only contains terms for the propagation of the phase. A derivation and summary of the matrices for different optical elements is provided by references [24, 26]. The advantage of the matrix formalism is that matrices of different optical elements can be concatenated to calculate the transmission through a system of N optical systems:

$$\begin{pmatrix} E_N^+ \\ E_N^- \end{pmatrix} = \boldsymbol{M}_N \dots \boldsymbol{M}_1 \begin{pmatrix} E_1^+ \\ E_1^- \end{pmatrix} = \boldsymbol{M}_\mathrm{S} \begin{pmatrix} E_1^+ \\ E_1^- \end{pmatrix} . \tag{2.2}$$

In case of a DBR, consisting of m equal pairs, an analytical expression for the maximum reflectivity, i.e. at the Bragg-wavelength, can be derived. According to [24], the reflectivity at the Bragg-wavelength is

$$R_\mathrm{DBR} = \frac{(1 - b^{2m})}{(1 + b^{2m})} \, , b = \frac{n_1}{n_2} , \tag{2.3}$$

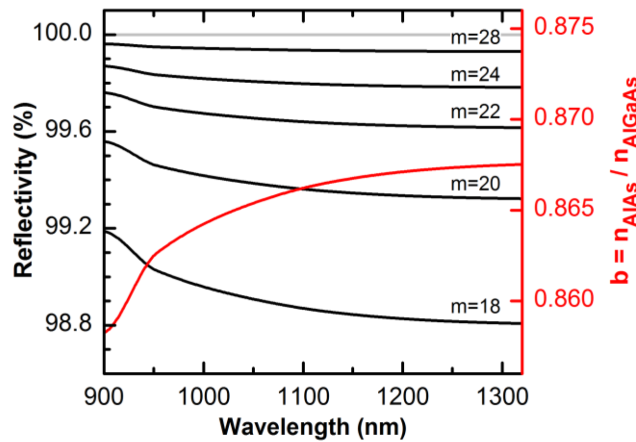

Figure 2.3. Calculation of the DBR reflectivity for different numbers of layer pairs with Eq. 2.3 and in dependence on the wavelength range (left axis). The right axis shows the refractive index ratio b as a function of the wavelength.

where n_1 and n_2 are the refractive indices of the DBR layers. In the present example (cf. Fig. 2.2), the DBR consists of 22 pairs of $AlAs/(Al_{0.2}Ga_{0.8})As$. Bragg-mirrors based on these materials will also be used in chapters 3–6, but for different design wavelengths. However, the refractive indices of AlAs and $(Al_{0.2}Ga_{0.8})As$ exhibit different dispersion, i.e. b is a function of the wavelength. This is illustrated by the plot of their ratio b against the wavelength in Fig. 2.3 (right axis). In the same graph, also the calculated reflectivity for different numbers of mirror pairs m is shown (the left axis). A reflectivity above 98.8 % is obtained for 18 pairs and within the whole range between 900 nm and 1300 nm. Due to the increase of b at longer wavelengths, which means a reduction of the refractive index contrast, the reflectivity is decreasing. Thus, a highly reflective mirror based on this material system and for a long emission wavelength requires somewhat more layers to maintain an excellent reflectivity. Still, if the number of mirror pairs is sufficient, such as 22 pairs, the reflectivity is improved to values above 99.6 % throughout the illustrated wavelength range. Because AlAs and GaAs have similar lattice constants, which are 5.661 Å and 5.653 Å [27], respectively, a high number of mirror layers can be realized with a high material quality. This enables the monolithic growth of highly reflective DBRs in GaAs-based lasers, which is a great advantage of the GaAs-system over other material technologies.

To obtain the reflectivity spectrum of a DBR, the transfer-matrix method can be numerically implemented. Thereby, the incident electric field at a specific wavelength can be "transferred" through the optical elements. Accordingly, the spectrum is obtained by incrementing the wavelength. An example of such a numerical calculation for a DBR with 18, 22, and 26 layer pairs and designed for a center wavelength of 1010 nm, is presented in Fig. 2.4. Here, it is assumed, that the DBR is bonded onto a $AuIn_2$ layer, which is the case for all chips investigated in this thesis. The resulting maximum reflectivity for 18 layer pairs is already 99.5 % and hence improved in comparison to the 98.9 %, obtained from Eq. 2.3. From the calculated spectra, also the spectral width of the stop band can be evaluated. The indicated spectral width in Fig. 2.4 is 115 nm. However, it must be noted, that the width of the high reflective region, e.g. R > 99.0 %, is somewhat smaller. The calculation shows also, that a reflectivity of 99.9 % is obtained for 22 layer pairs and still can be further increased by adding even more layers.

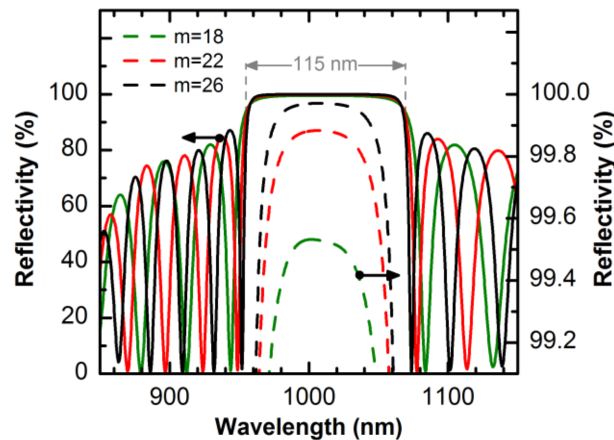

Figure 2.4. Transfer-matrix calculation of the DBR reflectivity for different numbers of layer pairs m and in dependence on the wavelength. The right axis shows only a reflectivity above 99.2 %, but for the same curves.

Longitudinal confinement factor

In the present case, the RPG, which is located on top of the DBR, consists of ten (GaIn)As QWs which are embedded into Ga(AsP) layers. The Ga(AsP) layers are also referred to as barriers since they serve as a potential barrier for the charge carriers in the QWs. However, the barriers also include other important functions. For instance, the phosphorus concentration is adjusted to compensate for lattice strain from the (GaIn)As on GaAs. The required phosphorus content is closely related to the barrier thickness and the indium content of the QWs. Moreover, the thickness of the barrier is used to adjust the optical distance between the QWs, i.e. the barriers can also be understood as separation layers. For stimulated emission, it is required that the standing wave light field anti-nodes are placed at the QWs which constitute the actual gain medium. This principle was already illustrated in Fig. 2.2. The black, red and light red lines show the light field intensity for three different wavelengths in dependence on the growth direction. It is illustrated that, if the barrier layer thickness is uniform and has the correct thickness, a maximum light field intensity of 4 can be obtained (if the incident field has the amplitude 1). Furthermore, the anti-nodes are aligned at the QWs, which are highlighted by the dashed lines. However, the amplitude is only 4 at a resonance wavelength. At other wavelengths, the attainable light field intensity is clearly reduced. To obtain the correct barrier layer thickness for the resonance at a the desired wavelength, it can be considered that the anti-nodes have to be centered at the QWs and need to be separated by an optical layer thickness of $\lambda/2$. Also taking into account that the QWs have a layer thickness d_{QW} different from zero yields slightly different physical thicknesses for the first and last barrier d_{oB} of the RPG in comparison with the center barriers d_{cB}. The correct physical layer thicknesses can obtained from

$$\begin{aligned} n_{\mathrm{QW}}\, d_{\mathrm{QW}} + n_{\mathrm{B}} d_{\mathrm{cB}} &= \frac{\lambda}{2} \quad \text{and} \\ \frac{n_{\mathrm{QW}}\, d_{\mathrm{QW}}}{2} + n_{\mathrm{B}} d_{\mathrm{oB}} &= \frac{\lambda}{2}\,, \end{aligned} \tag{2.4}$$

where n_{QW}, n_{B} are the refractive indices of the QWs and barriers and λ is the design wavelength. The transfer-matrix method can also be applied, to calculate the standing wave light field, as is illustrated in Fig. 2.2. Thus, it can be used to quantify the alignment of the anti-nodes at the QWs in dependence of the wavelength. An important outcome of these calculations is the longitudinal confinement factor (LCF) $\Gamma_z(\lambda)$ [11, 24]. It describes the mean light field intensity at the QWs and can be written as

$$\Gamma_z(\lambda) = \frac{1}{|E_0^+|^2 + |E_0^-|^2} \frac{1}{N_{\mathrm{QW}}} \sum_{j=1}^{N_{\mathrm{QW}}} \left| E_j^+ \exp(ik_j z_j) + E_j^- \exp(-ik_j z_j) \right|^2 \tag{2.5}$$

where $E^{+/-}$ are again the forward and backward travelling electrical fields, $E_0^{+/-}$ the amplitude of the incident and reflected electrical field from the whole structure, N_{QW} is the number of QWs, z_j is the QW position, and k_j is the propagation constant with

$$k_j(\lambda) = \frac{2\pi\, n_j(\lambda)}{\lambda}\,, \tag{2.6}$$

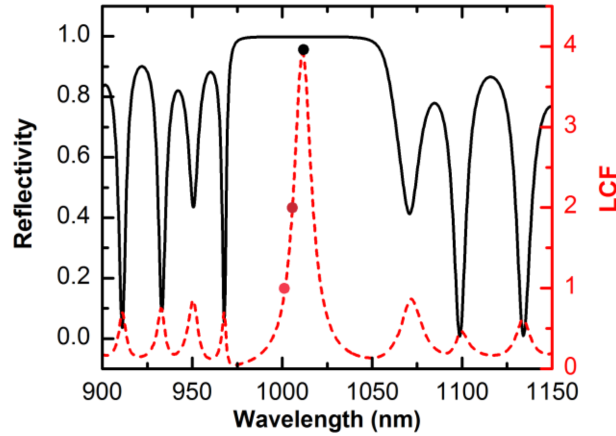

Figure 2.5. Reflectivity (left axis) and LCF (right axis) of a VECSEL which is designed for the emission at 1010 nm. Symbols illustrate the wavelengths of the light fields which were shown in Fig. 2.2.

where n_j is the (dispersive) refractive index of the j-th layer. The LCF and reflectance of the exemplary VECSEL structure from Fig. 2.2 is shown in Fig. 2.5. With Eq. 2.4 the structure is designed to exhibit the LCF peak at 1010 nm, which is also the center wavelength of the stop band. An important finding is that the LCF peak reaches a maximum of 4, in accordance to Fig. 2.2, but, close to the peak, the LCF also drops to values below unity. Additionally, the FWHM of the LCF peak is only 10 nm. Thus, the LCF has great impact on the laser performance, as will be discussed below and later in chapter 4. In chapter 4, it is also discussed, that different designs, such as an anti-reflection coated cap layer, can be applied to reduce the influence of the LCF.

Material gain

Another important function of the barriers is their pump light absorption. In barrier-pumped VECSELs, as exclusively studied in this thesis, it is the barrier which provides the generation of sufficient charge carriers. For example, the absorption of the 808 nm (1.53 eV) pump light is about 9800/cm in Ga(AsP) with low phosphorus content [28]. The thickness of an RPG for emission at 1000 nm is ~1.5 µm (cf. Fig. 2.2). Referring to the Beer-Lambert absorption law, 77 % of the pump light are absorbed in a single pass through the gain region. Due to a double pass of back reflected light from DBR and bond layer, this value can be somewhat higher. However, this depends on the employed materials. In any case, only a small fraction of the pump light is directly absorbed in the thin QWs.

As mentioned, the "original" function of the barriers is to provide a sufficient confinement potential for the charge carriers in the (GaIn)As QW. Depending on the indium content in the QW, the phosphorus content in the barrier can have a significant impact on the QW material gain, as will be discussed in chapter 5. A scheme of an ideal QW with finite confinement potential is represented by Fig. 2.6. The first electron and hole energy states as well as the probability density distributions are illustrated. Also the generation of charge carriers by the pump absorption in the barriers is illustrated. The black lines illustrate their relaxation to the lowest barrier states, their capture by the QW and subsequent relaxation to the QW ground state. Based on Fermi's Golden Rule the material absorption/gain from a QW can be written as

$$g_{\mathrm{mat}} \propto \langle F_{\mathrm{v}} | F_{\mathrm{c}} \rangle^2 \rho^{2D} (f_{\mathrm{c}} - f_{\mathrm{v}}) \tag{2.7}$$

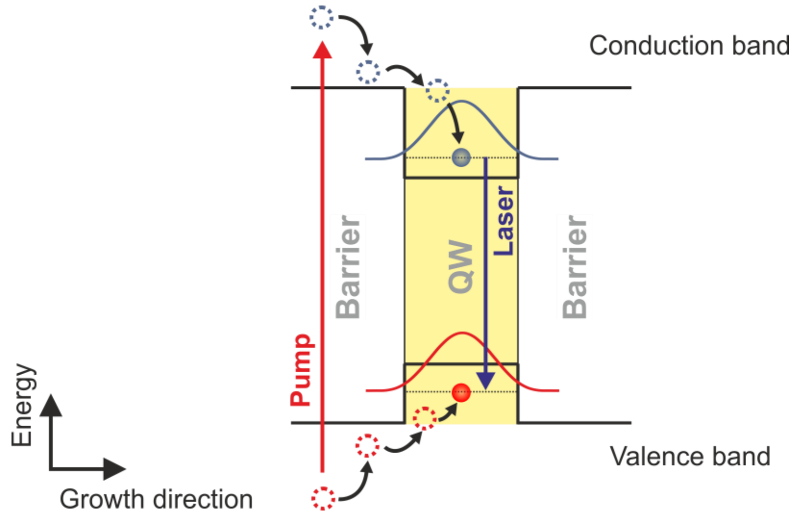

Figure 2.6. Scheme of a QW in a barrier-pumped VECSEL. The red arrow illustrates generation of charge carriers in the barrier. Black arrows indicate the relaxation process of carriers to the QW ground states from which their radiative recombination can take place in a laser process.

with the electron and hole wave functions $F_{v,c}$, the joint density of states ρ^{2D} of the QW electrons and holes, and the respective quasi-Fermi carrier distributions $f_{c,v}$ [24, 25]. Due to the single particle ansatz, Eq. 2.7 does often not satisfy the actual shape of gain/absorption spectra as observed in experiments. Nevertheless, it yields a comprehensible picture of the QW material gain/absorption. The relaxation of charge carriers from the barriers to the QW ground states happens on a time scale of picoseconds, the ground state lifetimes, however, are of a few nanoseconds [29]. Consequently, the population inversion is concentrated at these lowest energy states and the gain peak energy must be close to the band gap energy. Equation 2.4 accounts for this by the difference of the quasi-Fermi distributions which must be $0 < f_c - f_v < 1$ in case of population inversion and which gives the correct sign for the description of gain ($g_{mat} > 0$). At the low energy side, the gain spectrum, where $f_c - f_v$ is at its maximum value, is formed by the two-dimensional joint carrier density of states ρ^{2D} of the QW [24, 25]. At the high-energy side of the spectrum, gain is only maintained until $f_c - f_v = 0$. Thereafter, $f_c - f_v$ converges against -1 at which the unpumped material absorption is obtained. Another implication of Eq. 2.7 is that the optical gain/absorption is dependent on the spatial overlap of electron and hole wave functions $F_{v,c}$. This is particularly important for type-II QWs, where electrons and holes are spatially separated and which reduces the overlap of the involved states (cf. chapter 6).

In the past, a fully microscopic model was developed which demonstrates an outstanding agreement between calculated and measured PL and absorption/gain spectra [30]. Most notably, the model is only based on elementary bulk material parameters which are necessary to determine the single-particle band structure as well as electron and hole wave-functions, e.g. with the multi-band $\vec{k} \cdot \vec{p}$ approach [27]. Otherwise, a fully microscopic treatment of the system is conducted to obtain the many-particle properties, namely the Coulomb-interaction between electrons, the light matter interaction as well as the interaction between electrons and phonons. The many-particle dynamics, i.e. the microscopic polarization and carrier distributions, are obtained by solving the semiconductor Bloch equations. Once the microscopic polarization is known, the macroscopic polarization and, thus, the optical susceptibility can be calculated, which gives access to the measurable carrier induced refractive index change and the material absorption. For a calculation of the PL spectra,

also the light field has to be quantized and the semiconductor luminescence equations are solved. A review of the procedure specifically for VECSELs can be found in [31].

Modal gain and threshold condition

Not only the material gain is important for laser operation, but also the spatial overlap of the standing wave light field anti-nodes with the QW positions. Only then, amplification of the spontaneous emission from the QWs can take place. The wavelength at which the anti-nodes reach their maximum of 4 should ideally coincide with the peak wavelength of the material gain g_{mat}. This condition is described by the modal gain

$$g_{\mathrm{mod}} \propto g_{\mathrm{mat}}\Gamma_{\mathrm{z}}\Gamma_{\mathrm{t}} \tag{2.8}$$

where Γ_z is the LCF as stated above and Γ_t is the transverse confinement factor which describes an intensity distribution within the QW planes [11, 24]. With help of Eq. 2.8, also the threshold condition can be expressed. Therefore, light with the intensity I_0 is considered which is emitted from the VECSEL chip. It is back-reflected from the external mirror with the reflectivity R_{mirror}, passes the RPG region, is reflected at the DBR with the reflectivity R_{DBR} and again passes the RPG region until it reaches the initial point. This yields the round-trip intensity

$$I_{\mathrm{RT}} = I_0 \, R_{\mathrm{mirror}} \exp(g_{\mathrm{mod}}L) \, R_{\mathrm{DBR}} \exp(g_{\mathrm{mod}}L) \, T_{\mathrm{loss}} \tag{2.9}$$

where g_{mod} is the modal gain as defined in Eq. 2.8. The length L relates to the overall layer thickness, at which the light is amplified. A typical value is for instance $L = 80$ nm which is obtained with ten 8 nm thick QWs. Furthermore, a factor T_{loss} is introduced which can describe any kind of intra-cavity losses. Such a loss can be caused by additional intra-cavity elements, such as a nonlinear crystal, but can also involve inherent losses of the complete laser setup. An example for such inherent loss is a possible height fluctuation of the semiconductor interfaces, which involves intra-cavity surface scattering. It is reported that the loss can amount to 0.57 % even for a chip of high quality.

However, for laser operation it is required that the intensity reproduces itself, i.e. the laser gain must compensate the reflection losses as well as the other intra-cavity losses. This results in the threshold condition

$$\frac{I_{\mathrm{RT}}}{I_0} = 1 = \exp(2g_{\mathrm{mod}}L) \, R_{\mathrm{mirror}}R_{\mathrm{DBR}}T_{\mathrm{loss}} \ . \tag{2.10}$$

Detuning

The transverse confinement factor is essentially independent on the wavelength. In contrast, the material gain and the LCF are clearly functions of the wavelength. Moreover, the peak wavelength of both is depending on the temperature, which means that the modal gain is temperature sensitive.

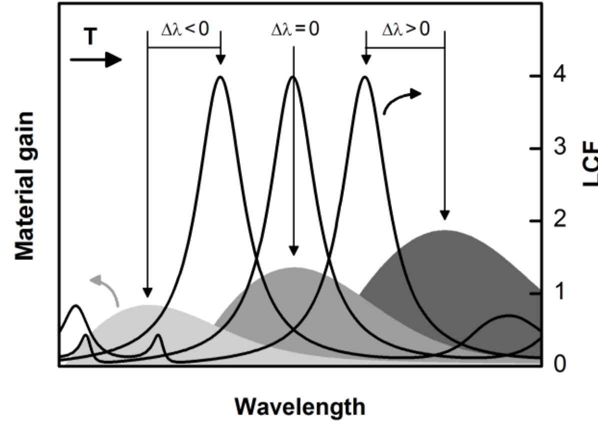

Figure 2.7. Illustration of material gain and LCF for different temperatures.

In a barrier-pumped VECSEL, considerable heat is generated because of the energy difference between the pump and laser photons. The fraction

$$\eta_{\mathrm{QD}} = 1 - \frac{\lambda_{\mathrm{pump}}}{\lambda_{\mathrm{VECSEL}}} \tag{2.11}$$

of the energy is referred to as quantum defect and mostly dissipated in non-radiative losses [32]. Besides, material gain and LCF have different temperature shift rates. As is measured in the next chapter, typical temperature shift rates are 0.34 nm/K for the material gain of (GaIn)As/GaAs QWs and 0.08 nm/K for the LCF. It will also be shown in the next chapter that typical temperatures of the material in the gain region, which is for brevity called gain temperature, come up to more than 120°C. Such significant temperature change in the gain region substantially modifies the spectral overlap between material gain and LCF and must be considered in the design. To account for the different shift rates, it is therefore reasonable to intentionally detune the peak wavelengths of the material gain λ_g and LCF λ_{Γ_z}. The difference in the peak wavelength can be specified by

$$\lambda_{\mathrm{Det}} = \lambda_{\mathrm{g}} - \lambda_{\Gamma_{\mathrm{z}}} \tag{2.12}$$

and is a fundamental property of VECSELs. As will be discussed in more detail in chapters 3 – 5, a negative detuning is required for VECSELs with regular type-I QWs. This is understood by means of the above-mentioned shift-rates and Fig. 2.7, which illustrates three different situations. From left to right the first situation is at low pump intensities. The material gain (light gray) builds up at the short-wavelength side of the LCF peak. Assuming that the VECSEL chip is not heated up significantly at that stage, the peak wavelength difference $\Delta\lambda$ is identical to the sample's detuning λ_{Det}. A significant part of the material gain is located at wavelengths, where the LCF is even smaller than unity. Hence, the material gain is even partially damped and the modal gain is reduced. However, as the VECSEL is pumped more intensively, the overlap of material gain and LCF is improved. This is illustrated by the second situation in the center of Fig. 2.7, where an optimum overlap is obtained, i.e. the material gain peak and modal gain peak coincide. The last situation at the right hand side occurs, if the pump intensity is further increased. Gain temperatures are further raised and material gain as well as LCF diverge.

It is clear that, due to the different shift rates of material gain and LCF, the detuning is a temperature dependent quantity. However, for a comparison of different designs or samples, it is reasonable to specify a detuning for a defined condition. This leads to the concept of the *room temperature detuning*, which is determined at temperatures of 20°C and at low excitation densities, where no pump induced increase of the gain temperature can occur. In the course of this thesis, the room temperature detuning will often be abbreviated by the term detuning. Detunings at other temperatures and excitation densities will consistently be called *effective detuning*.

Furthermore, from an experimental point of view, it is more difficult to measure the material gain peak wavelength which may depend on several experimental parameters, as for instance beam diameters, excitation intensities or pulse durations in a pump and probe experiment. Instead, the PL peak wavelength is used for the determination of the room temperature detuning, which can be accessed with less effort and on an early stage in the manufacturing of VECSELs. The exact procedure of the detuning determination is also discussed in the following chapter in more detail.

It should be noted that many different VECSEL designs have been realized, so far. The above discussed design is only a very specific example, but it is close to the samples investigated in this thesis. Actually, very different numbers and spatial arrangements of the QWs within the RPG have been tested in the past. For instance, there are designs with clearly more than ten equally spaced QWs [33], designs with unevenly distributed QWs [11], or designs with more than just one QW per anti-node [15, 34]. The reasons for these different designs are manifold. In particular, the trade-off between strain (and material quality), material gain and the thermal resistance is one important aspect. Also, VECSELs are not necessarily based on GaAs substrate, but can exploit different material systems, such as InP or GaSb substrates [35, 36]. This greatly increases the range of accessible wavelength with VECSELs. Moreover, not necessarily QWs must be used as gain medium. Also VECSELs with quantum dots (QDs) have been demonstrated with output powers at Watt level [37–39].

2.3 Thermal management

The performance of VECSELs is strongly affected by the generated heat in the device. This is also connected to the above-mentioned concept of detuning. The modal gain is significantly impaired at gain temperatures, where a weak overlap between material gain and LCF is obtained. This results in a reduced slope efficiency and the laser chip heats up more rapidly. Moreover, non-radiative losses, predominantly Auger losses, become more relevant at elevated charge carrier densities and gain temperatures. At a stage where such losses become important, even higher carrier densities are required to maintain the material gain. This in turn requires an increase of the pump intensity which causes an intensified generation of heat. Finally, a situation is achieved, at which gain cannot be maintained and where the laser shuts off. This power limitation is also referred to as the thermal roll-over of the VECSEL. An efficient heat removal, i.e. a low thermal resistance of the VECSEL, is hence desired to delay the separation of material gain and LCF and furthermore reduce inherent laser losses by the avoidance of high gain temperatures. Not surprisingly, a lot of studies have been dedicated to the understanding and optimization of heat dissipation in VECSELs [29, 38, 40–44].

The most efficient method to achieve efficient heat extraction from the pump region is heat spreading. Therefore, a material with preferably low and isotropic thermal resistance is connected to the gain chip. A chemical vapor deposited (CVD) diamond satisfies these preferences best and is certainly one of the most used heat spreaders in the field of VECSELs. Two different approaches to connect the heat spreader with the semiconductor material shall be mentioned. Both turned out

to be successful and have been investigated thoroughly in the past to optimize the heat removal from the gain region. The heat spreader is either bonded to the cap layer (intra-cavity heat spreader) or to the backside of the VECSEL chip (extra-cavity heat spreader) [45].

Intra-cavity heat spreading (ICHS) is promising for regularly grown VECSEL chips, i.e. if the laser structure was grown starting with the DBR and ending with the cap layer [46]. Although an anti-reflection coating is usually applied on intra-cavity heat spreaders to suppress reflection losses, it is not negligible for some applications. For example, undesired and inevitable reflections from the heat spreader might complicate other cavity arrangements than a linear cavity. The ICHS can also cause equidistantly spaced spikes in the emission spectra (Fabry-Pérot resonances). However, this is often avoided by a wedge in the transparent heat spreader. Additionally, the intra-cavity element must be of optical quality with low absorption and scattering losses which drives the costs of such a part.

Extra-cavity heat spreading (ECHS) turned out to be very efficient and enable lowest thermal resistances. If the laser structure is grown bottom-up, i.e. with the cap and gain region grown first and followed by the DBR section, the diamond heat spreader can be directly bonded onto the DBR. In a subsequent step, the substrate must be removed. Thus, this flip-chip technique requires a somewhat more elaborate processing in comparison with the ICHS approach. The benefit is a superior connection between heat spreader and heat sink. While the ICHS can only be mounted at the edges, the whole surface of the ECHS can be connected to a heat sink and heat can be extracted through a larger area. The efficiency of this concept was demonstrated with output powers in excess of 100 W [20, 21].

It is noteworthy, that the ECHS concept is only superior, if the DBR layers exhibit a high refractive index contrast and a good thermal conductivity. Only then, the number of layer pairs in the DBR can be kept small and an excellent reflectivity of the DBR is compatible with a low thermal resistance. This applies in particular to the GaAs/AlAs DBR system as studied in this thesis. However, the access to some wavelength regions requires the use of different material systems with inferior thermal conductivity and refractive index. In such a scenario, the number of Bragg mirror pairs must be increased in order to maintain a sufficient optical reflectivity. This can critically impair the thermal resistance of the Bragg mirror to a certain extent, at which it becomes more efficient to extract the heat with the ICHS concept.

In this thesis, flip-chip bonded VECSELs with ECHS are investigated. In the following, the thermal resistance of such chips is discussed in more detail. The theoretical model by Heinen et al. for the simulation of the thermal resistance in VECSELs with ECHS is summarized and applied to predict the thermal resistances of samples which are investigated in chapters 3 – 6 [44].

The ECHS concept is also popular in the field of other solid-state disk lasers where also efforts were made in order to describe the heat flux quantitatively [47, 48]. These works have later been refined with respect to VECSELs in order to find an optimal design for the heat spreader and heat sink [44]. The results were also an important contribution to the achievement of the output powers in excess of 100 W [20]. Most of the models are based on the finite elements method (FEM). In contrast to analytic approaches heat conduction can be simulated more accurately with the FEM as a minimum of approximations is needed while computational effort still is reasonable. To model the VECSEL chip, Lindberg et al. suggest to take advantage of the rotational symmetry [49]. In this way, the finite size of the VECSEL chip is neglected, but still a symmetric pump shape can be considered and the computational efforts are significantly decreased. The symmetry axis is perpendicular to the semiconductor layer stack and centered in the middle of the heat source which

is modeled by the spatial pump light absorption. Moreover, the semiconductor layer stack is reduced to sections, i.e. the RPG and the DBR each form a single layer with an averaged thermal conductivity and optical absorption. However, also the bond between chip and diamond, the diamond itself, as well as the heat sink contribute significantly to the overall thermal resistance and are added to the simulation structure. The heat removal by the thermoelectric coolers is modeled by a forced heat flow boundary condition at the backside of the whole stack. Also the temperature dependent thermal conductivity of the diamond heat spreader is considered [44].

One of the most important parameters, is the pump beam profile. It can be shown that the generated heat in the VECSEL chip is proportional to the absorbed pump light intensity. The absorbed intensity in a distance r from the symmetry axis and in a depth z along the growth direction can be described as

$$I(r,z) = I_{\mathrm{pump}}(r) \cdot I_{\mathrm{abs}}(z) \tag{2.13}$$

where I_{pump} is the pump distribution and I_{Abs} is essentially the Beer-Lambert law. Here, I_{abs} is a unitless factor, but the unit of the pump distribution is W/m². Furthermore, simulations show that the heat flux is essentially one-dimensional in the gain region, DBR, and bond, if the pump spot is smaller than the cumulated thickness of these layers. However, a three-dimensional heat flux is observed in the heat spreader, if it is sufficiently thick. In other words, a sufficiently thick heat spreader is required to enhance the thermal resistance. Still, larger volumes for heat dissipation are provided at the edge of the pump profile while more heat accumulates at the center. This important effect is also illustrated by the simulations in [44].

A general expression is required, in order to account for different pump distributions. It must enable the description of all variations between the commonly used Gaussian and flat-top beam profiles. This is provided by the super-Gaussian distribution, which is

$$I_{\mathrm{Pump}}(r) = \frac{P_S f(A,m)}{\pi a^2}\left(A^{\left(\frac{r}{a}\right)^{2m}}\right) \tag{2.14}$$

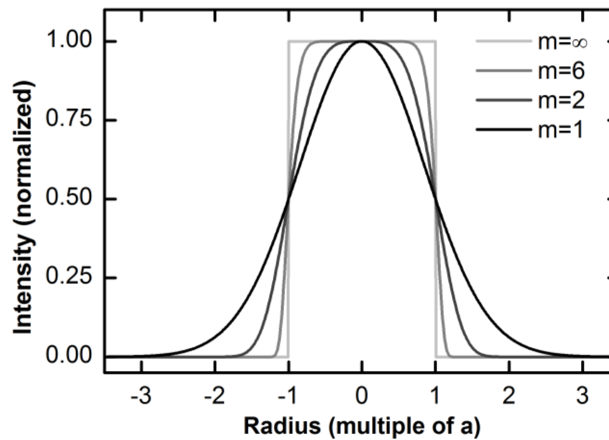

Figure 2.8. Illustration of different Super-Gaussian distributions for $m = 1, 2, 6$ and if m converges against infinity.

with the total power of the heat source P_S, normalization function *f*, order parameter *m* and heat source radius a. The relative amplitude 0 < A < 1 specifies the value at which the radius a is defined. In order to illustrate the influence of the parameter *m*, different super-Gaussian distributions are plotted in Fig. 2.8. For $m = 1$, a Gaussian distribution is obtained. Otherwise, the pump profile turns into a flat-top profile for increased values of m. It can be shown that

$$I_{Pump}(r) = \frac{P_S}{\pi a^2} \text{ for } r < a, m \to \infty, \text{ and} \qquad (2.15)$$
$$I_{Pump}(r) = 0 \text{ for } r \geq a\,, m \to \infty\,,$$

i.e. an ideal flat-top distribution, is obtained if *m* converges against infinity. To quantify the influence of different pump distributions on the thermal resistance, a scaling is required. Therefore, an analytical expression for *f* is obtained, if the ratio of the integrals of the ideal flat-top and the general Super-Gaussian distribution is calculated

$$f(A,m) = \frac{2\pi \lim_{m\to\infty} \int_0^\infty A^{\left(\frac{r}{a}\right)^{2m}} r\,dr}{2\pi \int_0^\infty A^{\left(\frac{r}{a}\right)^{2m}} r\,dr} = \frac{m(-\log(A))^{1/m}}{\boldsymbol{\Gamma}(1/m)}\,. \qquad (2.16)$$

This allows for a normalization of Eq. 2.14 for any $0 < A < 1$ and any order $m \geq 1$. Note that gamma does not represent the LCF, here, but the gamma function [50]. The multiplication of $1/f$ with the circular area $\pi\, a^2$ enables the direct determination of the pump power density from the total power P_S of the heat source.

In principle, the inclusion of the pump profile implies that a comparison between a measured and calculated thermal resistance requires an exact determination of the pump profile. Furthermore, it implies that the simulation must run with the profile obtained from a fit of the measured profile with Eq. 2.14. However, Heinen et al. show that the normalization factor *f* can be utilized for a correction of a thermal resistance calculation with ideal flat-top profile. It is demonstrated that, if $A = 1/2$ is chosen for the fit of the pump profile,

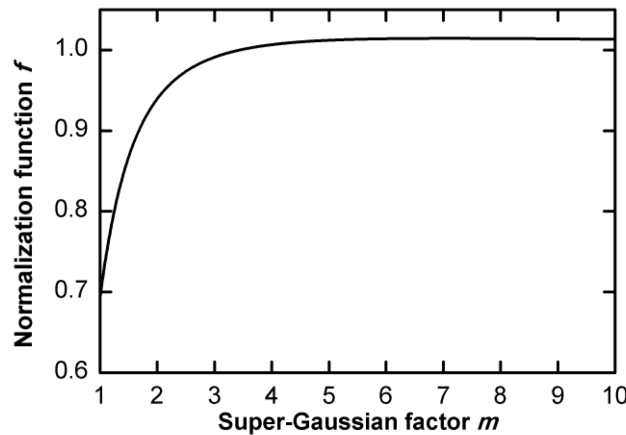

Figure 2.9. Plot of the normalization function $f(A = 1/2, m)$ which enables a comparison between a simulation with ideal flat-top pump profile and an experiment with an arbitrary Super-Gaussian profile.

$$\frac{R_{\text{th}}(m)}{R_{\text{th}}(m\to\infty)} \approx f(A=1/2,m) \ . \tag{2.17}$$

Consequently, it is sufficient to calculate the thermal resistance of a VECSEL structure for an ideal flat-top distribution. Figure 2.6, which shows $f(A = 1/2, m)$, or Eq. 2.17 can be used to calculate the actual thermal resistance for the respective pump distribution. It can also be followed that a thermal resistance, simulated with the ideal flat-top profile, clearly overestimates the thermal resistance of a measurement or simulation with $m < 3$, i.e. the thermal resistance is higher, if a flat-top profile is chosen. This is clearly a result of the three-dimensional heat-flux in the heat spreader. The heat from the center of the flat-top profile cannot be removed as efficiently as in a Gaussian profile which leads to an overall increase of the thermal resistance.

However, it must be noted that a flat-top profile is still preferable for high-power operation. This was experimentally demonstrated by Chernikov et al. [51]. In this study, the output power from a flip-chip bonded VECSEL could be enhanced from 4 W to 22 W by only altering the pump distribution from a Gaussian to a flat-top profile with constant FWHM and pump intensity. According to the above discussion, the thermal resistance was clearly increased by this experiment, while the output power was more than quintupled. This apparent contradiction can be resolved by considering the gain temperatures: Roll-over is achieved early at the center of the Gaussian pump spot. The central transverse laser modes roll-off early and cannot contribute to the output power. In the flat-top profile, the heat is distributed more evenly at cost of the thermal resistance. Still, the power at the center is significantly lower and higher pump intensities can be applied prior to reaching thermal roll-over. These findings demonstrate the importance of the thermal properties of VECSELs.

The thermal resistance calculations for four different flip-chip bonded VECSELs on a 350 µm thick diamond heat spreader and in dependence on the pump spot diameter are shown in Fig. 2.10. The simulations are conducted on the basis of [44]. It can be seen, that for all chips the thermal resistance is clearly reduced for increased pump radii. Concerning the relevant parameters for the thermal resistance simulations, the chip designs are similar, but exhibit different emission wavelengths and, hence, RPG and DBR thicknesses. The exact design of the devices will be discussed in the next chapters. Starting point of the simulations is the sample with the design wavelength of 1010 nm (green line). It is identical to "Design 2" in reference [44] and it was demonstrated that the thermal

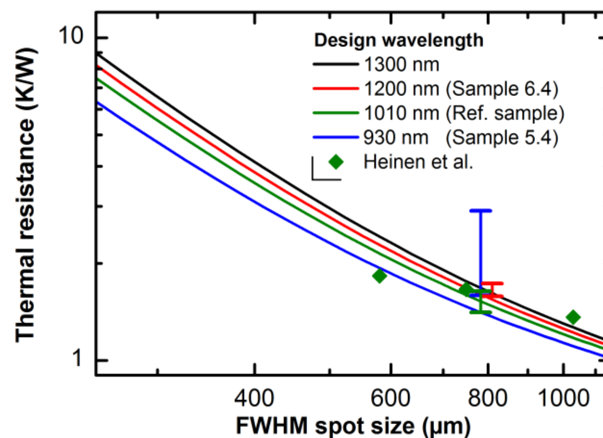

Figure 2.10. Thermal resistance simulation (lines) and measurements (symbols and bars) for different emission wavelengths but with similar chip design.

resistance simulation agrees well with the measured thermal resistance. These measurements by Heinen et al. are indicated as green symbols. Figure 2.10 gives also a preview on the following chapters. The thermal resistance of a chip with 1010 nm emission wavelength and with an identical design as “Design 2” is investigated in chapter 3 (green bar). The measured thermal resistance agrees well with the simulation. The chips at other wavelengths are also subject of this thesis. In chapter 5, samples with emission wavelength between 920 – 950 nm are investigated. A thermal resistance measurement is performed for a 950 nm chip, which can be well compared to the simulation of the 930 nm design (blue line and bar). Furthermore, in chapter 6 the thermal resistance of a type-II VECSEL with emission at 1.2 µm is measured and compared to the simulation (red). Also here, a good agreement with the simulation is obtained. The simulation shows, that the thermal resistances of the samples investigated in this thesis can be well compared. Especially, the thermal resistance should not be of major concern for the development of 920 – 950 nm VECSELs (chapter 5) or type-II VECSELs (chapter 6). In case of the type-II VECSELs it is desired to increase the emission wavelength to 1.3 µm. The simulation (black line) shows that this could be realized with the flip-chip technique, accepting only a small increase of the thermal resistance in comparison to the 1.2 µm samples.

2.4 Resonator geometries and operation modes

The flexibility and variety of parameters in the chip design have significant impact on the laser performance and enable the great wavelength versatility. Other key features of VECSELs are their excellent beam quality and their different operation modes. These features originate from the high degree of freedom in the arrangement of the laser resonator.

In order to achieve a high beam quality, the pump spot has to match the fundamental transverse electromagnetic (TEM) laser mode, i.e. the TEM_{00} mode. In case of the linear cavity, as illustrated in Fig. 2.1, the size of the TEM_{00} mode is dependent on the radius of curvature of the external laser mirror as well as the mirror’s distance to the VECSEL chip. The mode size on the VECSEL chip can also be calculated with a matrix formalism, where each optical element is described by a 2×2 matrix [52]. In chapters 3 and 5, only linear cavities are arranged. The external mirrors have a radius of curvature of -100 mm. An exemplary matrix calculation is presented for this configuration in Fig. 2.11. The full width at half maximum (FWHM) of the TEM_{00} mode is plotted against the

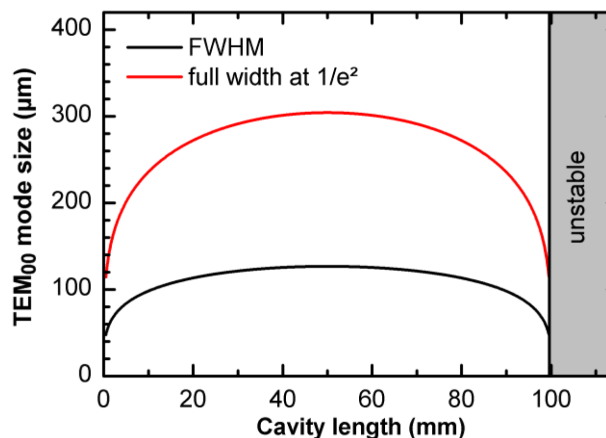

Figure 2.11. TEM_{00} mode size in dependence on the cavity length for an external mirror with a radius of curvature of -100 mm and in a linear cavity.

distance of the mirror from the VECSEL chip. It can be seen that the cavity becomes unstable, if the distance exceeds the mirror's radius of curvature. Depending on the cavity length, the FWHM mode size is between 120 µm and 50 µm, the $1/e^2$ width is between 110 µm and 300 µm, respectively. If the pump spot size becomes significantly larger than the mode size, lasing at higher order TEM_{nm} modes is observed. Most experiments in this thesis are carried out with multiple-transverse mode operation, because a high beam quality is not per se required for a fundamental characterization of a chip. If the pump spot size is large enough, the multiple-transverse modes uniformly fill in the pump spot. This results in a poor beam quality but facilitates the achievement of high output powers. Moreover, the laser is less sensitive against cavity misalignments. For instance, the output power is essentially independent on the cavity length, if the pump spot size is significantly larger than the maximum adjustable TEM_{00} mode size.

There are many other possibilities to arrange the external laser cavity. For example, if two external mirrors are employed, a V-shaped cavity is obtained. In such arrangement, the VECSEL itself or an external mirror can be used as the folding mirror. Moreover, it is possible to combine different mirrors, as for instance a plane and a curved external mirror, or two curved external mirrors. In chapters 4 and 6, also V-cavities with the VECSEL chip as folding mirror are used for studies.

A frequent application of the V-cavity arrangement is found in mode-locked VECSELs, where a regular, plane end mirror is replaced by a saturable absorbing mirror (SAM). The exact cavity arrangement is an important adjustment parameter as it determines the repetition rate and can be used to account for the different saturation fluences of the SAM absorption and VECSEL gain [12]. The first mode-locked VECSEL was presented in the year 2000 with pulse durations in the picosecond regime [53]. Since then, many works have driven the optimization of pulsed VECSELs, forming essentially a new field of research. Today, pulse duration in the sub-picosecond regime are reported by several groups [34, 54, 55]. Furthermore, the VECSEL can be self-mode-locked without an additional SAM [56–58]. Even though the underlying physical mechanism of this mode-locking technique is not clear, the cavity arrangement seems also to be a key parameter here [59–61]. Detailed reviews about mode-locked VECSELs are provided by the references [8, 12, 14].

Beside SAMs, also other optical elements can be placed within the cavity. One example is the use of birefringent filters to force single-frequency operation. Linewidth as narrow as 75 kHz can be achieved with Watt level output powers [62]. Yet, the highest output power in single-frequency operation is 23 W with a sub-MHz linewidth [63]. Additionally, a non-linear crystal for intra-cavity frequency conversion can be placed in the cavity. In combination with a birefringent filter and an adapted cavity configuration, extremely high intensities at a narrow linewidth can be achieved within the crystal. This enables for highly efficient frequency-conversion. In this way, multiple-watt emission in the visible regime and with an excellent beam quality can be generated by second-harmonic generation [23, 64]. In the ultra-violet regime the record power is 260 mW at 330 nm emission wavelength [65]. Even output powers of 20 W are achieved in the visible regime [22, 23]. Via difference frequency generation also remarkable output powers of up to 2 mW could be achieved in the THz regime [66]. Also for this topic of intra-cavity frequency conversion, detailed reviews are available [8, 9, 13].

3. Methods of fundamental VECSEL studies

As indicated in the previous chapter, the VECSEL performance is dependent on many different parameters which all have to be considered in VECSEL development and optimization. With this respect, the inclusion of different fields of physics is a challenge within the VECSEL research field. A "closed-loop" interplay of these fields has the best promise for success [30].

One of these fields is a *predictive theory* of semiconductor gain materials. It enables the study of different material parameters, such as QW thickness and composition, or the choice of the barrier material. The impact of design parameters on the laser threshold, laser efficiency, and output power can be calculated.

The second research field deals with the *epitaxial growth* of the laser structures. Not only crystal strain, but also the availability of high-purity precursors for metalorganic vapor-phase epitaxy (MOVPE) or effusion cells for molecular beam epitaxy (MBE), high-quality substrates, and the capabilities of the respective reactors set stringent limitations to the realization of semiconductor lasers. Yet another demand for the growth of VECSELs is high precision and reproducibility. Only then, the reactors can be calibrated to meet the desired specifications, which is usually done by the growth of test structures. Once the specifications are met, the more expensive complete VECSEL structure is grown with the established settings. Consequently, it is beneficial to iterate a design between the first two research fields prior to the growth of a laser structure. Moreover, the further processing of the wafers is of great importance, as it has a great impact on the chip's quality.

The third field is presented in this chapter. It addresses the *fundamental experimental laser characterization* and allocates the determination of the attributes of realized VECSELs. The most prominent laser attributes certainly include the threshold pump density, slope efficiency, and maximum output power. These values describe the performance of the laser already very well but still represent only a skin-deep characterization. Moreover, it may occur that a laser is not operating at all, which disqualifies such straightforward investigation. However, the concern of a fundamental laser characterization is also to identify properties, which lead to a specific feature or malfunction, i.e. a low or high threshold, slope efficiency, or output power. For example, if a VECSEL with poor performance is present, it might be a matter of a low material gain, an inappropriate detuning, a high thermal resistance, or even an unfavorable interplay of these factors. It is therefore desired to isolate the individual contributions and expose the actual delimiter. The results enable a constructive coordination with epitaxy and theory to improve the laser in an iterative optimization process.

Subject to this chapter is the introduction of the experimental methods which are applied to unravel and analyze the individual parameters. Exemplary measurements are performed and explained by means of a reference VECSEL structure. The obtained analysis for the reference structure will be employed for a detailed comparison and discussion of the other VECSELs throughout this thesis.

Structural details, power curves, and laser spectra of the reference sample are presented in sections 3.1 and 3.2. These properties are closely related to the *modal gain* and the *heat transport capabilities*. As described in chapter 2, the modal gain is a product of the material gain, the longitudinal, and the transverse confinement factor. It was discussed that the spectral detuning between the material gain and the LCF plays an important role in the functionality of the laser. An accurate determination of the detuning is performed in section 3.3. It is based on PL measurements, reflectance measurements, and the calculation of the LCF. These measurements also yield important information about the composition of the laser structure and serve as a thorough investigation of

the chip quality. A comparison of the measured reflectivity with transfer-matrix calculations provides an examination of the chip composition. In section 3.4, a direct measurement of the modal absorption and gain in dependence on the pump power is performed. This measurement will be used for a discussion and comparison with 920 – 950 nm in chapter 5. Section 3.5 summarizes approaches for the thermal resistance determination and provides the indication of the gain temperatures, which is important to understand the laser's capabilities. The last section 3.6 is dedicated to an overview of the results for the reference structure. A table is provided which will simplify the look up of the usual properties of a well-functioning VECSEL device.

3.1 Reference Sample

A MOVPE grown VECSEL with emission around 1 μm is chosen as reference structure. At this wavelength, VECSELs with the best performance, in particular in terms of output power, have been reported. The good performance at this wavelength is explained by the well-balanced laser properties. On one hand, the QW depth enables an excellent confinement for electrons and holes, resulting in a high material gain. On the other hand, the quantum defect of 20 %, employing 808 nm optical pump, which is highly absorbed in the barriers, is reasonable in comparison with devices at longer wavelength. Also, the crystal strain can still be well compensated to achieve a high material quality. The high refractive index contrast of GaAs/AlAs enables the growth of rather short, but high quality and high reflective DBRs (cf. section 2.2). Owing to the short DBR, a flip-chip bonded VECSEL with a very good thermal resistance can be realized.

The resonant periodic gain of the reference sample consists of 10 equally separated $(Ga_{0.76}In_{0.24})As$ QWs. The optical barrier layer thickness is $\lambda/2$ with respect to $\lambda = 1010$ nm, which will be confirmed in section 3.3. The barriers consist of GaAs, strain compensating $Ga(As_{0.97}P_{0.03})$ layers embed the QWs. Both, the GaAs and the Ga(AsP) are highly absorptive at the pump wavelength of 808 nm. The DBR consists of 22 pairs of $AlAs/(Al_{0.1}Ga_{0.9})As$. The structure was grown bottom-up. An ECHS is used and flip-chip bonding is carried out. For this, a chip with a size of 4 mm × 4 mm is cleaved from the wafer. This chip and a 350 μm thick CVD diamond heat spreader are mounted in a vacuum chamber and coated by vapor deposition of gold and indium. The metallic faces are then brought together ("flip-chip") and heated under slight pressure for the actual bonding process. Afterwards, the GaAs substrate is removed by mechanical thinning and selective wet chemical etching onto the $(Ga_{0.52}In_{0.48})P$ cap layer. The success of this last step is a first measure of the chip quality. For instance, a poor bond quality might result in a high thermal resistance. However, it is

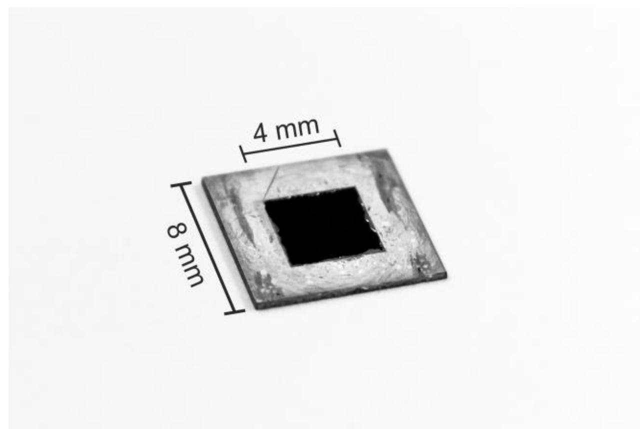

Figure 3.1. Photograph of a flip-chip bonded VECSEL with removed GaAs-substrate.

self-evident that a poor bond will not get through the thinning and wet chemical etching. A photograph of the reference sample is shown in Fig. 3.1. The width and length of the diamond heat spreader are 8 mm.

All VECSEL chips within the scope of this thesis are processed according to the described procedure, i.e. all samples are flip-chip bonded onto 350 μm thick CVD diamond heat spreaders. The VECSEL wafers and compositions measured with HR-XRD are obtained from the Material Sciences Center in Marburg, Germany, as well as the NAsP III/V GmbH, in Marburg, Germany, where the MOVPE is performed.

3.2 Laser power curves

The reference VECSEL is mounted onto a thermo-electrically cooled copper heat sink and arranged in a linear cavity with a length of 75 mm, as illustrated in the previous chapter (cf. Fig. 2.1). The employed mirrors have a radius of curvature of -100 mm. The VECSEL is driven by a fiber-coupled, 808 nm pump laser. A pair of lenses with 50 mm and 55 mm focal length is used to focus the pump beam with a 30° angle of incidence onto the chip. The reflectivity at 808 nm is 35.2 % for this particular sample and angle. This value is not obtained by only accounting for the Fresnel reflection at the (InGa)P cap layer which yields 22.8 %. However, the 1/e optical depth is approximately 1/(9800/cm) ≈ 1 μm and, thus, includes the complete RPG. Therefore, the reflection is still modified by interferences of multilayer reflections.

As described in section 2.3, the pump intensity distribution has a great impact on the device performance. This suggests, that the pump intensity distribution should characterized carefully. Therefore, the VECSEL chip is translated until the pump spot is located at the bond material. The scattered pump light is readily imaged onto a CCD camera which is oriented perpendicular to the chip's surface. Multiple images of the pump spot on the bond material are then recorded while the chip is translated within the area of the pump beam waist. Equation 2.14 is fitted to the averaged pump spot profile choosing $A = 1/2$. FWHM of 740 μm × 825 μm for the x and y axes are obtained, which reflects the elliptical shape of the profile caused by the oblique angle of incidence. Another important parameter is the order of the super-Gaussian distribution $m = 2.73$ which gives rise to the flatness of the applied pump profile. As discussed in section 2.3, this parameter is most significant in concerning the thermal resistance. Referring to Figs. 2.8 and 2.9, a rather flat-top distribution with $f = 0.98$ is observed instead of a Gaussian distribution. In comparison, the FWHM width of the TEM_{00} mode is only 140 μm (cf. Fig. 2.11), so only highly multiple transverse mode operation is observed in this configuration.

In the first investigation, power curves with a set of four different output couplers are measured. The transmissivities are 1.1 %, 3.2 %, 5.0 % and 9.0 %, respectively (cf. Fig. 3.2). Comparable performance is observed for the 3.2 % and the 5.0 % mirrors, a maximum output power of 30.7 W is achieved with the 3.2 % output coupler though. A higher or lower mirror reflectivity results in a reduction of the output powers and slope efficiencies, as is demonstrated with the 1.1 % and the 9.0 % mirrors. The exact knowledge of the pump distribution enables an accurate indication of the pump intensity. As expected, the best threshold is observed with the lowest mirror transmissivity at a pump intensity of 0.9 kW/cm². Yet a low threshold of 1.0 kW/cm² is observed at 3.2 % transmissivity, followed by clearly increased thresholds of 1.4 kW/cm² and 4.9 kW/cm² for the 5.0 % and the 9.0 % mirrors. A summary of the thresholds and maximum output powers is depicted in Fig. 3.2 (right). These trends show that the best performance is offered by the 3.2 % mirror.

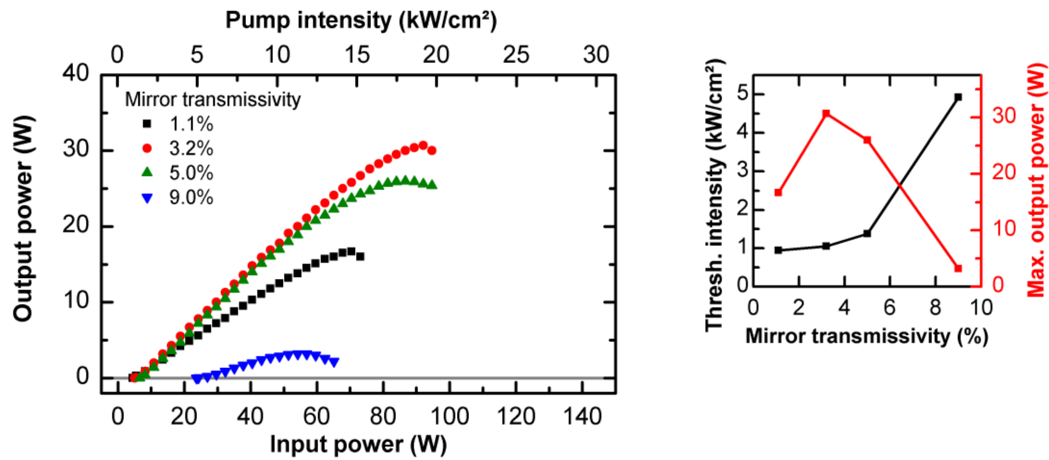

Figure 3.2. Power curves (left) and the threshold intensities as well as maximum output powers (right) dependent on the mirror transmissivities (1.1 % - 9.0 %).

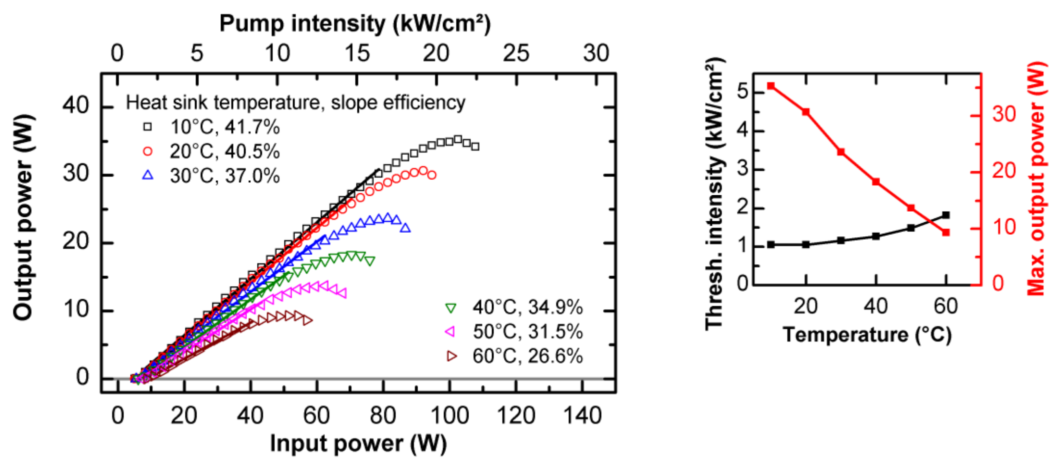

Figure 3.3. Power curves (left) and the threshold intensities as well as maximum output powers (right) dependent on the heat sink temperature (10°C - 60°C).

Another important information is obtained from the demonstration of lasing with 9.0 % mirror transmissivity which enables an approximate determination of the gain of the sample (cf. section 3.4).

The power curves are also recorded with the 3.2 % mirror in a series of heat sink temperatures between 10°C and 60°C in 10°C steps (cf. Fig. 3.3). The best performance is observed at the lowest heat sink temperature of 10°C, with a threshold density of 1.0 kW/cm², a slope efficiency of 44.7 % and a maximum output power of 35.3 W. For raised heat sink temperatures, threshold densities are increased while slope efficiencies and output powers are decreased. Threshold intensities and maximum output powers is summarized in Fig. 3.3 (right).

The temperature characteristics of the sample are closely related to the detuning. An in-depth discussion of the detuning dependent performance follows on chapter 4. Though, a first conclusion is that such a well-functioning laser sample provides a good example in order to discuss and review the performance of other VECSEL devices.

3.3 Determination of the detuning

As discussed in section 2.2, an optimized detuning is required for efficient laser operation. Equation 2.8 states that the intensity of the light field at the QWs is important for laser operation. The highest laser efficiency is achieved, if the standing light wave anti-nodes coincide with the QWs (at the laser operation wavelength). Therefore, efficient laser operation is only obtained if the material gain coincides with the LCF maximum. A complication is that material gain and LCF both are temperature dependent and hence the room temperature detuning was introduced (cf. Eq. 2.12).

If the detuning and the temperature dependences of λ_g and λ_{Γ_z} are known, it is possible to analyze realized laser structures and investigate the performance in correlation with the detuning. The experimental identification of the room temperature detuning is the prominent subject of this section, but the presented experimental procedure is accompanied by a thorough review of the structural composition of a VECSEL and enables a detailed comparison to the original design.

Reflectance measurements

If the reflection of the VECSEL is measured, indirect information about absorption and, thus, the modal gain is obtained. In connection with HR-XRD measurements, it enables the determination of the LCF. Furthermore, in some cases, a temperature dependent reflectance (TDR) measurement may already expose the detuning of the VECSEL [21]. Even if this may not be the case, at least it can be found whether the sample exhibits a large or small detuning. A detailed discussion and explanation is provided in the following section.

For the reflectance measurement, a laser chip is mounted onto a thermo-electrically cooled copper heat sink which enables a variation of the temperature between -20°C and 100°C (cf. Fig. 3.4). White light is focused onto the VECSEL chip using achromatic lenses. The diameter of the focal point is approximately 1 mm. A beam splitter is used to guide the reflected light to a focusing lens which couples the light into the fiber of an optical spectrum analyzer.

A silver mirror is placed in front of the sample and translated to the focus of the white light beam to detect a reference spectrum. The reflectivity is obtained by dividing the sample spectrum, which is obtained in the same manner, and the reference spectrum. Due to the high DBR reflectivity, it

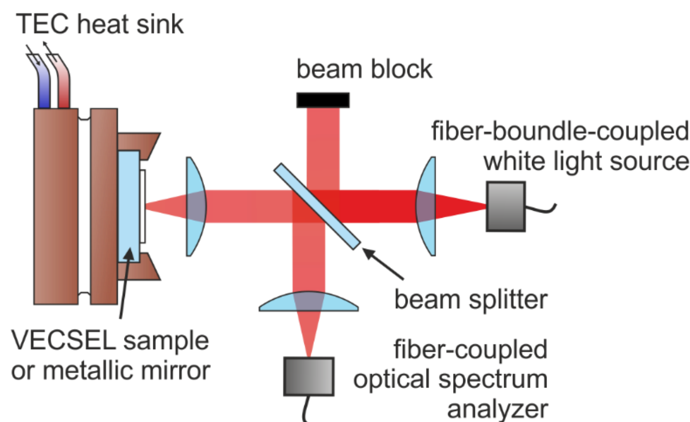

Figure 3.4. Scheme of setup for temperature dependent reflection measurements

can be assumed that the reflectivity maximum within the stop band region is unity. Hence, the result is normalized.

A measurement for the temperature range between -20°C and 100°C with 10°C steps is shown in Fig. 3.5. The expected red shift of the reflectivity curve is observed. In order to determine the temperature shift rate of the reflectivity, the wavelengths of two reflection minima on either sides of the DBR are plotted versus temperature (cf. Fig. 3.6). The shifts of the minima are well described by linear functions. The average slope of the linear regressions is 0.08 nm/K. It is worth to note that the stop band is very broad and flat in comparison to the laser spectrum. Hence, the temperature dependent reflectivity has no impact on laser operation. Still, this shift rate is of importance because the LCF is closely connected to the reflectance and shifts with the same rate. As will be shown in the following chapter, the LCF exhibits a narrow peak with a FWHM of 11 nm which implies that the temperature dependence is of great importance.

This great influence is observed at the absorption dip which arises within the stop band and which gets deeper for increased temperatures. This is explained by a detuning of the material absorption and the LCF in such way that almost no overlap of the material absorption and the LCF peak is present at lower temperatures. For higher temperatures the overlap is steadily increasing. To discuss this temperature dependence, the relative absorption, which depicts the percentage of reflectivity loss in comparison with the stop band maximum, and the corresponding wavelength are plotted versus temperature (cf. Fig. 3.7). It is shown that from -20°C to 0°C the absorption maximum is placed at 1002 nm. For higher temperatures the wavelength of the maximum absorption is linearly increasing with a rate of 0.13 nm/K (cf. Fig. 3.7 (bottom)). This shift rate is different from the shift rate of the reflectivity which implies that it is affected by the QW absorption. The relative absorption exhibits an ‘s’ shaped characteristic. Below 0°C the absorption is less than 10 %. This shallow trend at low temperatures is due to a weak spectral overlap of QW absorption and LCF. The absorption increases linearly until a temperature of 80°C is reached. Afterwards, a saturation is indicated at 100°C with a maximum absorption of about 55 %. Consequently, the overlap of the LCF with the material absorption is steadily increased until 100°C. This indicates that the detuning at room temperature must be of considerable magnitude. To evaluate the detuning from such measurement, it is necessary to determine also the shift rate of the QW emission. This will be carried out later. It will be shown that the shift rate is 0.34 nm/K. Considering that the maximum absorption is reached between 70°C and 100°C and a shift rate difference of (0.34 – 0.08) nm/K between absorption and LCF, the detuning should be in the range between -16 nm and -21 nm.

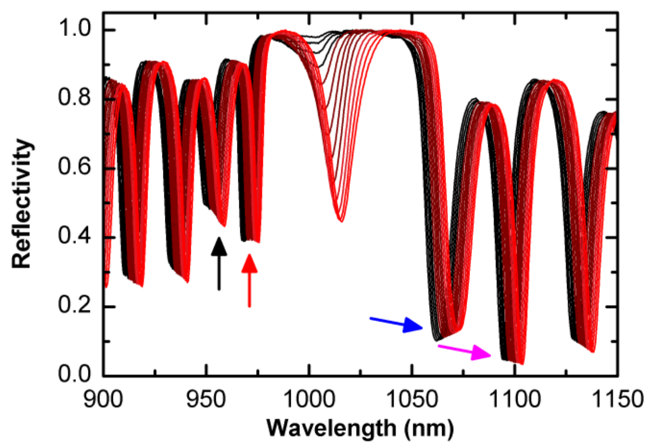

Figure 3.5. Temperature dependent reflectance (TDR) of the reference sample. The curves are recorded from -20°C (black) to 100°C (red) holder temperature with 10°C steps.

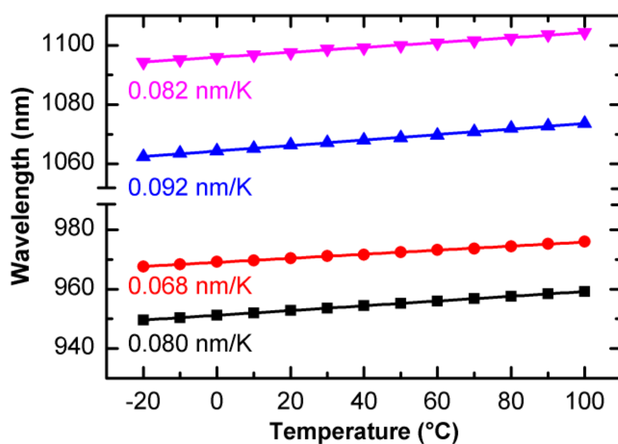

Figure 3.6. Shift of the two reflection minima on each side of the stop band.

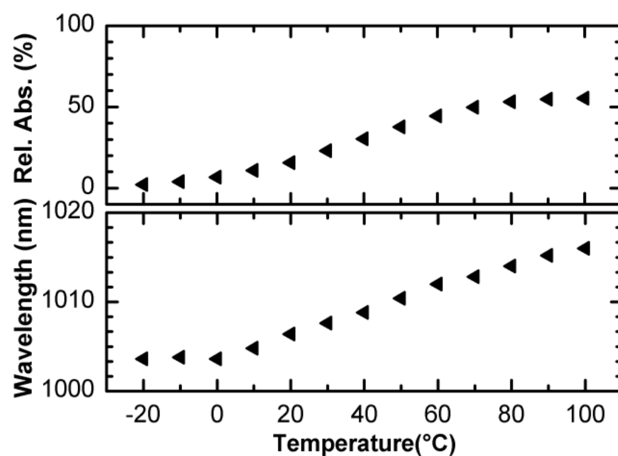

Figure 3.7. Temperature dependence of the relative absorption (top) and the wavelength of the absorption maximum (bottom).

Reflectance and longitudinal confinement factor simulation

In order to obtain more accurate information about the detuning, it is necessary to analyze the coupling between the QWs and the light field. Hence, it is required to reveal the exact LCF. The LCF cannot be measured directly but can be calculated with the transfer-matrix method if the optical layer thicknesses of the whole VECSEL structure are known. A measure of accuracy of this approach is the agreement between a reflectance measurement and its simulation. Although the layer thicknesses are known from the design process of such samples, in practice it is more reliable to revise the realized layer thicknesses and compositions which may deviate from the design. HR-XRD measurements are a powerful tool to provide an insight into these parameters, especially for periodically grown structures as they are present in the RPG of VECSELs. The QW thicknesses as well as barrier thicknesses and compositions of a VECSEL can be determined accurately. Therefore, these values are used as initial parameters in a fitting procedure with the matrix transfer method. However, due to the great DBR thickness, the DBR layer thicknesses cannot be determined precisely. This is also the case for the cap layer thickness, due to its vanishing strain. Fortunately, the DBR consists of the well-established AlAs/GaAs material system and can be grown with high precision. Hence, these layer thicknesses should not deviate critically from the original design values. In contrary, the cap layer thickness can significantly deviate from its design thickness, because it acts as an etch stop layer for the selective wet chemical etching in the flip-chip bonding process. Irregularities during the etching can have an influence on the LCF.

In conclusion, the combination of all results enable a detailed characterization of the VECSEL structure. The RPG composition is known from the XRD measurement, whereas the DBR and cap layer thicknesses can be used as a fitting parameter for the transfer-matrix simulations. It is expected that the obtained optical thicknesses of the DBR will only differ slightly from the design values, whereas significant discrepancies might be observed for the cap layer. A comparison between the measured and calculated reflectivity for the reference VECSEL is illustrated in Fig. 3.8.

The gray area represents the measured reflectivity at 20°C holder temperature, the black line represents the corresponding transfer-matrix analysis. A good agreement between measurement and calculation is observed. Here, the absorption of the QWs is neglected in the calculation which can be observed by means of the absent absorption dip within the stop band. The absorption of the QWs is a matter of a fully microscopic theory which is beyond the scope of this thesis. In order to find a quantitative measure for the reliability of these results, relative errors between the design

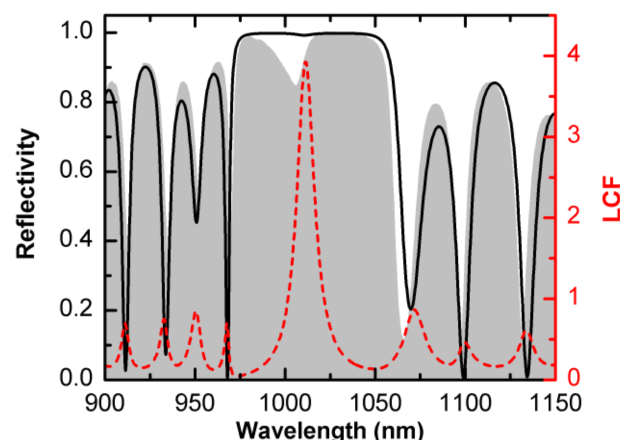

Figure 3.8. Measured (gray area) and simulated (black line) reflectivity of the reference sample as well as the longitudinal confinement factor (red dashed line).

thicknesses and the values obtained from the fit are calculated. For this sample, the relative errors relating to the cap layer and the AlAs/(AlGa)As DBR layers are both below 1 %. These findings show that the layer thicknesses of the realized sample must be very close to the original design values. The red-dashed line in Fig. 3.8 represents the calculated LCF. It is observed that at 20°C the LCF maximum is located at higher wavelengths (1011 nm) in comparison with the absorption dip (1006 nm). This is in agreement with the TDR measurement because the maximum absorption is observed at higher temperature, and, thus, the LCF and the absorption dip should overlap only at elevated temperatures. Another important result is the reaching of the LCF maximum reaches at almost 4, thereby achieving its theoretical maximum.

Edge photoluminescence measurements

Referring to the room temperature detuning definition in Eq. 2.12, the detuning can be determined if the LCF and the peak wavelength of the PL are known. In case of surface emitters, the QW PL cannot be measured readily. The obtained surface PL is a function of the LCF and the actual QW PL. Theoretically, it is therefore possible to obtain the pure PL spectrum, if the surface PL is divided by the LCF. This procedure was presented for instance by J. Hader et al. [32]. But, as exemplarily can be seen from Fig. 3.8, the LCF drops to very low values, which can complicate the determination of the actual peak wavelength. Another approach is to measure the surface PL of test structures without micro-cavity. Such samples are usually grown prior to the growth of the actual laser but with equal parameters. The lack of interferences enable a direct determination of the peak wavelength. However, the accuracy of this approach depends on the discrepancies between the test structure and the actual structure. Depending on the realization of a VECSEL it might be difficult to avoid significant discrepancies. Whereas some well-established QW gain media, such as (GaIn)As QWs, can be reproduced with high accuracy in a careful epitaxy process, it is known that the growth of other gain media is more sophisticated. For instance, this might be the case for quaternary QWs containing dilute nitrides. In chapter 6, it will also be demonstrated that a small deviation of the Sb or In contents in type-II QWs can result in a rather big variation of the PL properties.

Most accurate results for the detuning are hence obtained, if the QW PL of the actual laser structure is observed. An alternative for measuring the surface PL is a measurement of the *edge* PL where the Fabry–Pérot resonances of the micro-cavity are not present.

The procedure of an edge PL measurement depends on the design of the structure. For “regularly” grown VECSELs, i.e. if the structure is grown in the sequence DBR, RPG, and cap layer, the edge PL can be measured straight-forward. For this, the sample is mounted onto the edge of a copper heat sink and excited at the desired wavelength. If the edge of a processed laser sample is covered due to a heat spreader or similar, an unprocessed sample of an adjacent wafer piece should be used. The edge of the sample is brought into focus of a collimation lens which guides the PL to the optical spectrum analyzer.

Here, flip-chip bonded samples are investigated. This complicates the measurements, because the edge of the chip is covered by the indium bond. Furthermore, the chip is placed at the center of the diamond and the PL cone is cut and, thus, only hardly detected from such sample. Therefore, an unprocessed sample of an adjacent wafer piece must be used.

Depending on the DBR composition, the edge PL can either be directly investigated or a further processing of the sample is needed. If a *ternary* $AlAs/(Al_xGa_{1-x})As$ *DBR* with $x > 8$ % is present,

which is transparent at 808 nm, the sample can be excited right through the DBR. Further processing is required in case of a *binary AlAs/GaAs DBR,* where the 808 nm pump light is absorbed at the GaAs layers within the DBR. One possibility is to excite the structure at higher wavelengths, such as 980 nm and excite the RPG through the substrate. This results in a weak absorption within the RPG region and accordingly in a weak PL signal. Alternatively, the sample can be glued (DBR side down) onto the edge of a sapphire plate. Then, the sample is processed like the actual laser structure, i.e. the substrate is thinned and removed by chemical wet etching. This sample is then excited through the cap layer.

The setup where the sample is mounted onto the edge of the thermo-electrically cooled cooper heat sink is illustrated in Fig. 3.9. A fiber coupled 808 nm diode laser is used for excitation. Two anti-reflection coated lenses are employed as collimation and focusing lenses for the laser beam. Also, a collimation lens and a focusing lens are used in order to couple the signal into the optical fiber which is attached to the optical spectrum analyzer and which is used to record the PL spectra. For the correct determination of the room temperature detuning, a power and temperature dependent edge PL measurement is performed. According to the discussion in section 2.2, it is only meaningful to measure the peak wavelength at a low excitation power, where the structure is not heated up. A power dependent measurement shows which excitation power can be regarded as “low density”. Furthermore, a linear regression of the peak wavelengths can be applied to obtain a more accurate result. The power dependent edge PL of the reference sample for excitation powers between 1 mW and 2 W is shown in Fig. 3.10. Regular QW spectra are observed. The peak wavelength is around 1 μm. The short-wavelength tail is generated by hot carriers with a Boltzmann energy distribution, which can be assumed at low excitation densities. However, close to 900 nm a more significant drop of the PL intensity is observed which indicates that an additional loss mechanism takes place. Such a loss mechanism could be a thermal escape of the holes into the Ga(AsP) barriers, which will be discussed in more detail in chapter 5. On the contrary, the long-wavelength tail is formed by the two-dimensional density of states in the QWs, which is broadened by intrinsic statistical alloy fluctuations.

An analysis of the power dependent edge PL measurement is shown in Fig. 3.11. The power dependent peak wavelength is well described by a linear function. From the linear regression, a low excitation density peak wavelength of 997 nm is determined. The integrated intensity increases

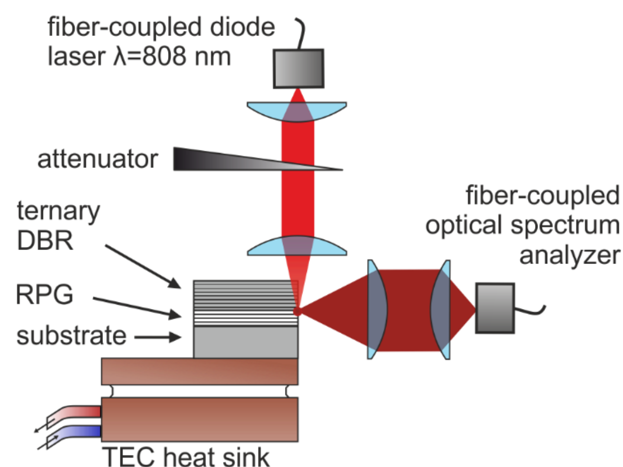

Figure 3.9. Scheme of the setup for the edge PL detection.

linearly with the excitation power until a few hundreds of mW. Due to thermal quenching, the slope of the integrated intensity decreases at high excitation densities which also, due to the heat, results in the red shift of the peak wavelength. Still, resonances of the micro-cavity may distort an edge PL measurement, e.g. because the detection does not take place exactly in the RPG plane. To expose such potential distortion, it can be exploited that QW emission and micro-cavity resonance have different temperature shift rates. Therefore, an impaired PL spectrum should manifest an artificial temperature dependence. The temperature dependent measurement is shown in Fig. 3.12. Here, the shape of the edge PL is not changing in some unexpected behavior. The intensity is decreasing with temperature due to an increase of non-radiative losses. It is observed that the slope at the short-wavelength side of the spectrum is decreased for higher temperatures. This is consistent with a Boltzmann distribution of the electron and hole energies. In contrast, the long-wavelength side does not depend on temperature.

The temperature dependent shift of the band gap energy in bulk III/V semiconductors can be well described by the empirical Varshni formula [67]. For sufficiently high temperatures the shift can usually assumed to be linear. The band gap of the bulk $(Ga_{0.76}In_{0.24})As$ can further be calculated assuming a simple quadratic dependence of the alloy composition. Overall, a calculation based on

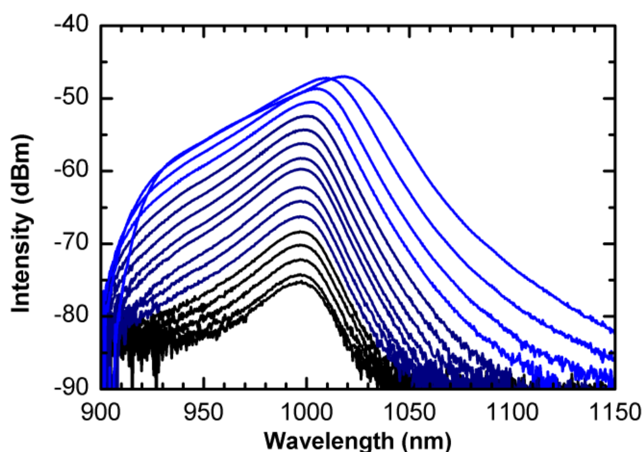

Figure 3.10. Power dependent edge PL measurement of the reference sample. Excitation powers reach from 1 mw to 2 W. The exact excitation densities can be found in Fig. 3.11.

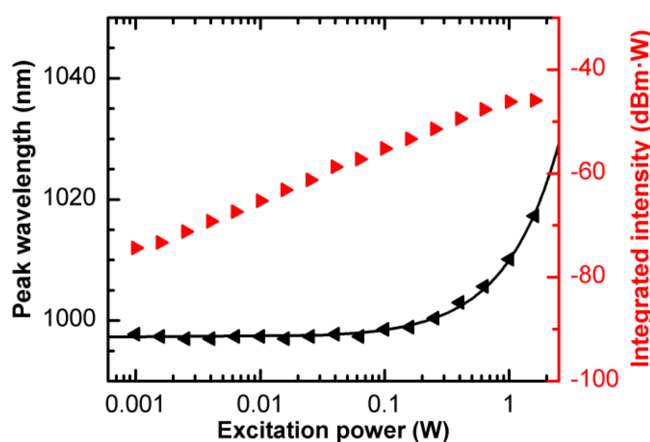

Figure 3.11. Power dependence of the peak wavelength and the integrated intensity of the edge PL of the reference sample. The black line is the linear regression of the peak wavelength. The integrated intensity is shown in red color and at the right axis, respectively.

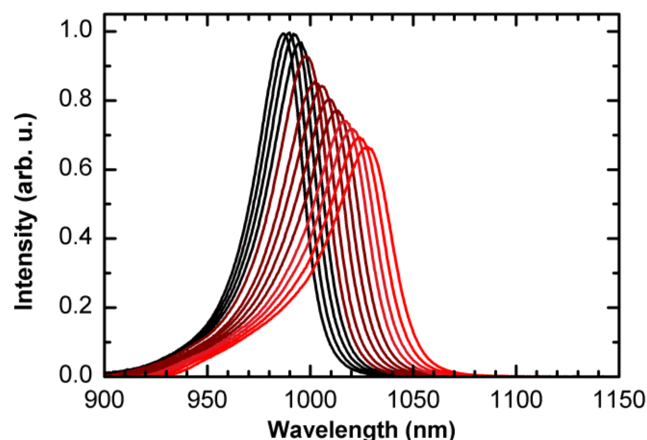

Figure 3.12. Temperature dependent edge PL measurement of the reference sample for a temperature range of - 20°C to 100°C.

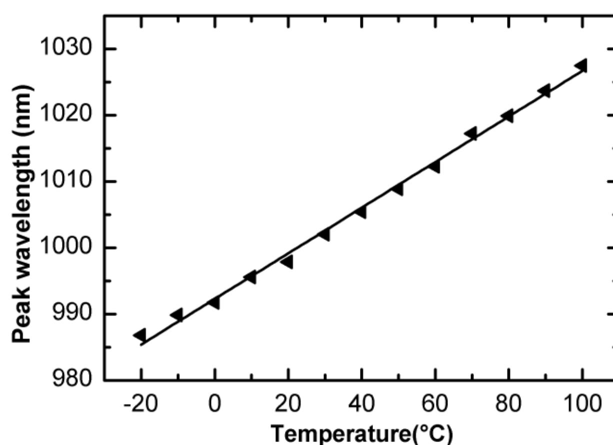

Figure 3.13. Peak wavelengths of the temperature dependent edge PL measurement. The slope of the linear regression is 0.34 nm/K.

the recommended Varshni and bowing parameters yields a band gap energy reduction of -50 meV between -20°C and 100°C [27]. If this energy reduction is applied to the lowest measured peak emission wavelength of 986.8 nm at -20°C heat sink temperature, an emission wavelength of 1028 nm at 100°C heat sink temperature is calculated, which is in good agreement with the measured 1027.5 nm (cf. Fig. 3.13). Hence, the calculated shift rate is 0.34 nm/K which is the slope of the linear regression in Fig. 3.13.

Detuning summary

The temperature dependent reflectivity was recorded to provide insight into the detuning of the sample. It can be related to the depth of the absorption dip within the DBR stop band. An approximate value for the detuning was obtained from the TDR measurement (-16 nm to -21 nm). Furthermore, the reflectance measurement was compared to a transfer-matrix calculation which can reveal potential discrepancies in comparison with the original design. In this way, the resonance wavelength of the LCF is obtained, which is 1011 nm at room temperature in case of the reference sample. An accurate determination of the detuning is obtained by complementary excitation power and temperature dependent edge PL measurements. A low excitation room temperature peak

wavelength of 997 nm is observed and, accordingly, a room temperature detuning of -14 nm is obtained. Obviously the detuning is overestimated with the TDR measurement. This can be explained by the asymmetry of the QW absorption. If the peak wavelengths of the LCF and the QW absorption coincide, still more absorption is present at the short-wavelengths. For higher temperatures, also the spectral overlap between absorption and LCF is improved at the long-wavelength tail, resulting in a somewhat higher absorption. Consequently, it is more accurate to determine the detuning from the exact edge PL and LCF determination.

3.4 Quasi-equilibrium gain measurements

In early years of laser research, the associated theory was not yet highly developed, not to mention the lack of computing capacities. Consequently, gain properties could not be easily predicted and the development of new or optimized lasers was steadily accompanied by the discussion of gain measurements and the related detection techniques. This section will present a gain measurement setup for VECSELs. Also nowadays important conclusions can be derived from gain measurements, as will be demonstrated in chapter 5. Before the mentioned setup is discussed, it is helpful to reconsider gain measurement techniques from literature. Famous gain measurement techniques developed in the 70's are especially the variable stripe length method and the method by Hakki and Paoli.

Reviews of the *variable stripe length* method have been offered by K. L. Shaklee et al. (1971, 1973) [68, 69]. It is based on an optical pump – optical detection scheme. A sample is excited at the edge with a rectangular beam profile, i.e. a stripe with length L (perpendicular to the edge) and width b (parallel to the edge). The PL, which originates from the edge, is detected as a function of the stripe length L. Based on the Beer–Lambert law, the detected intensity can be described by

$$I(L) \propto \exp(gL) - 1 \tag{3.1}$$

where g denotes, absorption ($g < 1$), transparency ($g = 0$), or gain ($g > 1$). In this way, the material gain can be directly detected. Also, the method can be applied to an edge emitter, if anode or cathode material are transparent at the excitation wavelength.

The Hakki–Paoli method was presented in 1973 and 1975 [70, 71]. In contrast, to the variable stripe length method it is based on an electrical pump – optical detection scheme and restricted to electrically driven lasers. It is exploited that there must be a connection between the Fabry–Pérot resonances with the transmissivity (absorption or even amplification) of the gain medium. The spectra of amplified spontaneous emission are detected with a high wavelength resolution while the device is operated closely below the threshold. If a sufficient spectral resolution is at hand, the intensity maxima and minima of the Fabry–Pérot resonances can be determined and evaluated to obtain the modal gain. Furthermore, the electromagnetic field distribution insight the laser structure can be calculated to obtain the material gain spectra from a relation similar to Eq. 2.8.

In the past, both methods have been revised and modified by many other works in the history of laser research [72–74]. However, these techniques focus rather on the characterization of gain in edge-emitting semiconductor lasers.

In contrast to that, fewer literature deals with gain measurements of surface-emitting semiconductor lasers, especially with VECSELs. Nowadays, highly developed theory is available which can be

used to analyze and design gain media. Therefore, gain measurements become dispensable in many cases and it is more efficient to optimize structures based on a comparison with the theory. Hence, the impact of gain measurements has become less significant. However, there are still cases where an experimental determination of the gain is a significant complimentary study. As will be motivated later, this case includes the studies of 920 – 950 nm VECSELs in chapter 5.

The approach for gain measurements on VECSELs is to perform a reflectivity measurement while the gain chip is pumped. An example of such a measurement is described in reference [75]. Haupt et al. use a regular continuous wave 808 nm diode laser as pump source and another VECSEL to probe the device under investigation. A beam splitter is used to guide the probe beam, which is reflected from the sample, to a photodetector. The probe beam is mechanically chopped and a regular lock-in-detection scheme is used to obtain a sufficient signal-to-noise ratio. Furthermore, a Faraday isolator is employed to prevent a distortion of the “probe VECSEL” from back-reflections.

The measured quantities are the intensity of the probe prior to reflection $I_0(\lambda)$ and after reflection at the gain chip $I_\mathrm{P}(\lambda)$. Similar to the derivation of the threshold condition (cf. Eq. 2.9 and 2.10) it is obtained that

$$\frac{I_P(\lambda)}{I_0(\lambda)} = \exp(2g_\mathrm{mod}L)\, R_\mathrm{VECSEL} \tag{3.2}$$

where g_mod is the modal gain as defined in Eq. 2.8. The length L can be adapted to different definitions of the gain. Haupt et al. relate L to the cavity length, but if it is desired to calculate the material gain, L must account for the cumulative QW thickness in the RPG, as was also suggested in chapter 2.2. In such a measurement, it is not possible to separate the reflection losses R_VECSEL from the VECSEL chip and the absorption. However, if the gain region is centered within the DBR stop band, a reflectivity of 1 can be assumed. Furthermore, no out-coupling mirror with reflectivity R_mirror is present in a gain measurement, which justifies

$$\frac{I_P(\lambda)}{I_0(\lambda)} \approx \exp(2g_\mathrm{mod}L). \tag{3.3}$$

For VECSELs, it is meaningful to express gain as a reflectivity greater than unity, or the difference

$$G = \frac{I_P(\lambda)}{I_0(\lambda)} - 1, \tag{3.4}$$

because this value can be directly related to the maximum applicable loss, e.g. by the output coupling mirror. As demonstrated in section 3.2, the reference sample still lases with a mirror loss of 9.0 %. Hence, G must be larger than 9 %. High-resolution X-ray diffraction measurements yield an accumulated QW width of $L = 74$ nm. A LCF close to 4 was simulated in the preceding section. Consequently, it can be concluded that the material gain is at least 1455/cm.

In the described gain measurement setup, the “probe VECSEL” has to meet the emission wavelength of the sample under investigation. The probe wavelength and line-width can be controlled by an intra-cavity etalon and for each adjusted wavelength a measurement with a series of different pump densities can be performed. The wavelength resolution is limited by the linewidth of the “probe VECSEL”. However, the spectral bandwidth of the measurement is limited by the modal gain width of the “probe VECSEL”. Depending on the variety of gain samples and their

emission wavelengths it may also be required to employ different optical isolators. Therefore, the setup by Haupt et al. is strictly limited by the wavelength capabilities of the available probe laser and the Faraday isolator. For the investigation of samples at different wavelengths, it is desired to change the probe source and eventually also the optical isolator. To achieve a greater versatility, it is required to replace the probe laser by an adequate device. For instance, titanium sapphire lasers cover a great spectral range and can be employed as shown by Borgentun et al. [76]. Also, transient gain dynamics can be investigated if the arrangement is combined with time-domain spectroscopy, i.e. a pump – probe scheme. Such measurements have been performed on well-established type-I VECSELs by Head et al. [77] as well as Mangold et al. [78] and on a type-II VECSEL by Lammers et al. [79].

Concerning continuous wave gain measurements, an even more desirable alternative is to replace the probe laser by a broadband white light source. An incandescent lamp inherently covers the necessary spectral range and is not sensitive to back-reflections which supersedes the use of an optical isolator. In this section a setup is presented which employs an incandescent lamp. A thorough study of the measurement setup can be found in the master thesis by A. Kalinger [80]. Basic considerations are described in the following.

The setup is illustrated in Fig. 3.14. The white light is focused onto a facet of a fiber-bundle. At cost of intensity, the fiber-bundle enables a more careful alignment. The white light is collimated, reflected by the beam splitter, and focused again onto the sample. The focusing lens also serves as collimation lens for the reflected light which then passes the beamsplitter and is focused onto the monochromator. In order to collect the divergent light from the output of the monochromator, two lenses are used for collimation and focusing onto the (GaIn)As photodetector. Only achromatic lenses are used to minimize the aberrations.

As indicated, the spectral capabilities of the individual components are the advantages of this setup. To demonstrate its superior spectral range, the reflectance of a silver mirror is measured from 820 nm to 1340 nm. The resulting spectrum is a product of the white light spectrum, the monochromator transmission function, a transmission function of any other optical element within the path (including the silver mirror), and the responsivity of the (GaIn)As photodetector. The averaged spectrum of a long-time measurement consisting of 11 spectra is shown in Fig. 3.15. The red line indicates the average intensity I_{avg} plus and minus the standard deviation s of the signal in dependence on the wavelength. The signal to noise ratio (SNR) can be determined by

$$\text{SNR} = \frac{I_{\text{avg}}}{s} \tag{3.5}$$

The SNR is indicated at the right axis of Fig. 3.15. It is about 200 throughout the whole wavelength range, which implies the capabilities for gain measurements in this range. Furthermore, the spectral range was limited by the maximum rotation angle of the stepper motor which is used to drive the monochromator. Hence, it is possible to gain access to even lower or higher wavelength by only centering the stepper motor to another wavelength.

However, one challenge in such an arrangement is to maintain the SNR if the gain chip is pumped. The light intensity on the photodetector can be written as the sum of the reflected white light $I_{\text{W}}(\lambda)$ and the PL signal $I_{\text{PL}}(\lambda)$

$$I_{\text{PD}} = I_{\text{W}}(\lambda) + I_{\text{PL}}(\lambda). \tag{3.6}$$

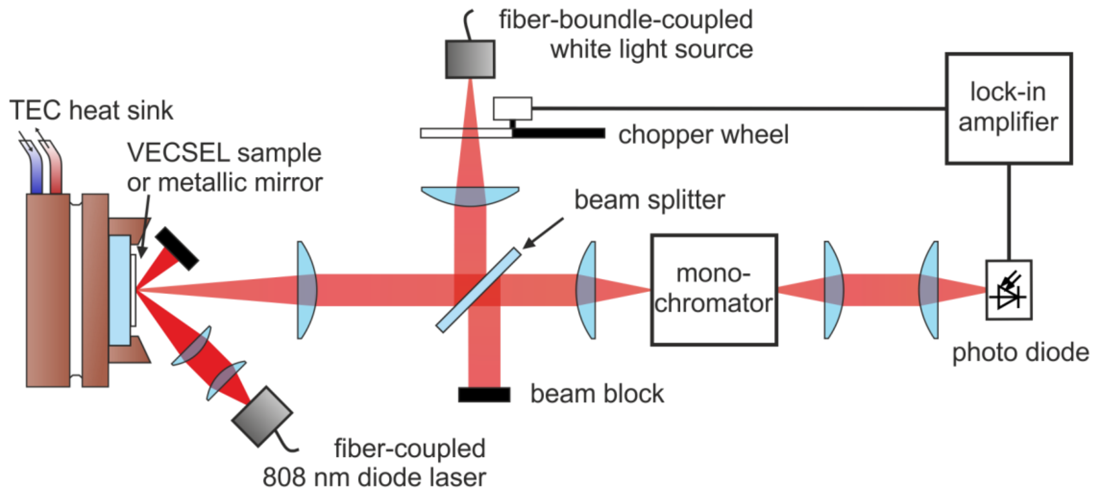

Figure 3.14. Scheme of the continuous wave gain measurement setup.

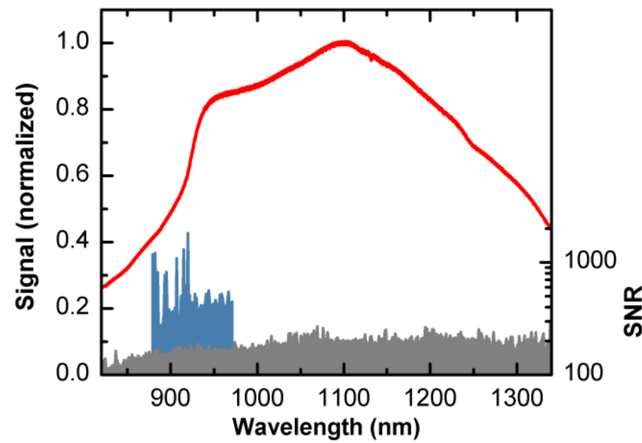

Figure 3.15. Normalized reflectance (red line), and SNR (gray area) of a silver mirror. The thickness of the red line indicates the standard deviation. Also shown is the SNR for a pumped gain structure (blue area) at an excitation intensity of 1.8 kW/cm².

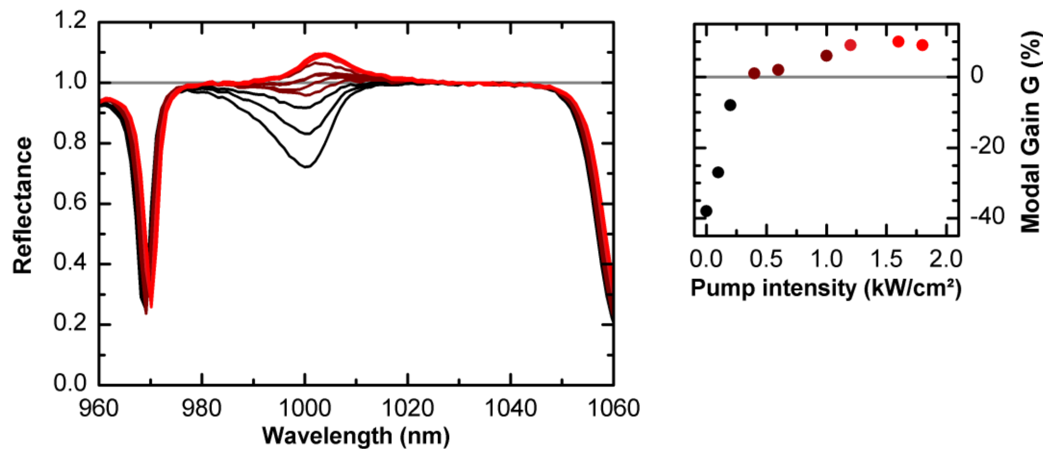

Figure 3.16. Result of the gain measurement of the reference sample. The reflectivity in dependence on the pump density is shown left. The maximum absorption and gain, i.e. the modal gain G, is plotted versus the excitation intensity (right).

In the present setup, both intensities pass the monochromator. Still, the PL signal is much more intense than the white light signal. Although only the white light is chopped and detected, the PL signal causes a continuous load at the detector and may have a significant impact on the SNR. This also implies, why the monochromator should be placed in front of the photodetector. An alternative position would be between the white light source and the gain sample. In such an arrangement, the total integrated PL intensity encounters the photodetector and may impair the SNR, or even saturate the photodetector. In other words, in the introduced setup the monochromator also serves as a variable bandpass filter which should maintain the SNR while the gain structure is pumped. This is demonstrated by means of a gain sample around 930 nm. The SNR is determined at pump intensity of 4 kW/cm². The result is shown as blue area in Fig. 3.15. The improved SNR in comparison with the silver mirror measurement can be explained by an improved alignment.

Finally, an exemplary gain measurement is carried out with the reference sample. The result is shown in Fig. 3.16. The black curve corresponds to the unexcited reflectivity (cf. Fig. 3.16 (left)). While the sample is excited, its absorption dip within the stop band is bleached until transparency and even gain is observed. The percental gain G is plotted versus the excitation intensity (cf. Fig. 3.16 (right)). A maximum gain of about 10 % is observed which is in agreement with the observation of lasing with the 9.0 % output coupler. The measured threshold intensity of about 0.5 kW/cm² is lower as in the laser experiment (1.0 kW/cm²), however, this discrepancy might be due to intra-cavity losses which cannot be revealed in the gain measurement.

Overall, the measurement is neat demonstration of the applicability of the setup for a gain characterization. Although similar information is obtained from the power curves in the previous chapter, it is demonstrated that the setup provides a powerful characterization tool. Such gain characterization can be helpful, if not such a set of output couplers is available for a specific wavelength. Furthermore, it might appear that lasing is not observed for specific samples. In such a case, the absence of modal gain can only be proven by a gain measurement, which excludes uncharted cavity losses.

3.5 Thermal resistance measurement techniques

As explained in chapter 2, the temperature of the gain medium has a great impact on the laser performance. If a poor thermal resistance is present, the pumped structure will heat up rapidly, laser threshold will be reached only at elevated temperatures and thermal roll-over will occur already at low dissipated powers which also implies low output powers. In this regard, the thermal resistance is an important quantity for the power capabilities of a VECSEL structure. Besides, a thermal resistance determination can reveal other important quantities, such as the temperature and excitation power dependent laser wavelength shift rates and, most importantly, the gain temperature can be determined for an arbitrary heat sink temperature and pump power. This enables the identification of the gain temperatures at threshold and at the maximum emission wavelength, i.e. at the point of thermal roll-over. These findings play an important role in laser development, because low gain temperatures are wanted to achieve low laser thresholds and on the other hand a maximization of the gain temperatures at roll-over is required for high output powers. Furthermore, the thermal resistance, threshold densities and gain temperatures can serve as input parameters for a thorough experiment-theory comparison.

Yet, different approaches for thermal resistance measurements have been proposed. A résumé of three practical techniques is presented by means of the reference sample in the following.

Shift-rate method

In section 3.3 the excitation density and temperature dependent properties of the reference sample have been investigated. Linear wavelength shift rates for the spontaneous emission and the reflectivity have been observed. Heinen et al. show that the laser wavelength exhibits linear dependences as well, i.e. a linear red shift is observed in dependence on the heat sink temperature and dissipated power [43]. This implies that both, the heat sink temperature and the dissipated power, have a linear influence on the gain temperature. A linear change of the gain temperature results in a linear wavelength shift. Based on these findings, it can be shown that

$$\lambda = \frac{\partial \lambda}{\partial T}(T_{\mathrm{Hs}} - T_0) + \frac{\partial \lambda}{\partial T} R_{\mathrm{th}} P_{\mathrm{D}} + \lambda_0 \tag{3.7}$$

with the laser wavelength λ, the heat sink temperature T_{Hs}, the thermal resistance R_{th}, the dissipated power P_{D}, the offset wavelength λ_0, and offset temperature T_0, respectively. The dissipated power is defined by the difference of net input power and output power. In the experiment, the heat sink temperature and pump power can be varied while the emission wavelength and output power are recorded. This resulting measurement data for λ, T_{Hs}, and P_{D} can each be written as a column vector. Then, Eq. 3.7 can be written as a system of linear equations. Its solution yields the shift rates $\partial\lambda/\partial T$ and $\partial\lambda/\partial P_{\mathrm{D}}$ as well as the offset wavelength λ_0 at T_0. The thermal resistance is then calculated by

$$R_{th} = \frac{\partial \lambda}{\partial P_D} \Big/ \frac{\partial \lambda}{\partial T}. \tag{3.8}$$

Whereas the recorded temperatures and optical powers are experimentally acquired as discrete values, the laser spectra usually have a width of several nanometers. Furthermore, the spectral width is usually also a function of the gain temperature. It bears the question which discrete values must be extracted from the spectra to calculate the thermal resistance correctly. This matter can be resolved by connecting Eq. 3.7 with a laser spectrum and the three-dimensional heat transfer and the pump distribution. While heat can primarily dissipate in one dimension at the center of the spot, a three-dimensional heat flow can take place at the outer regions. Furthermore, the pump profile usually exhibits the highest intensity at the center. Since the long wavelength tail of the spectrum corresponds to the hottest region in the gain medium, it must correlate with the center of the pump spot. Vice versa, the short-wavelength tail correlates with the outer region of the pump spot. The temperature dependence of the latter depends also on the temperature dependent threshold, which can result in a non-linear behavior. Following these relations, a fixed point of the gain region, namely the center, can be investigated by measuring the maximum wavelength of the laser spectrum. The maximum wavelength can be defined by an adequate intensity drop with respect to the intensity maximum of the spectrum.

The result of an exemplary thermal resistance measurement for the reference sample is shown in Fig. 3.17. The heat sink temperatures are varied from 10°C to 60°C in 10°C steps. Spectra at various pump powers are recorded at each heat sink temperature. An intensity drop of 10 dB at the long wavelength tail is used to extract the discrete wavelengths. Circles indicate the measured data and lines the linear regression with Eq. 3.7. A thermal resistance of 1.38 K/W is obtained. The corresponding value for a perfect rectangular pump distribution is 1.41 K/W which even undercuts the result from the simulations and the existing experimental data (cf. section 2.3). It is noteworthy

that on the basis of such a measurement, any lasing wavelength can be correlated with a specific gain temperature by

$$T_G = \frac{(\lambda - \lambda_0)}{\partial\lambda/\partial T} + T_0. \tag{3.9}$$

Hence, further important information can be obtained. For instance, the spectra at lowest pump powers have been recorded close to the threshold. Accordingly, it can be observed that the sample does not heat up significantly before lasing starts. At a heat sink temperature of 20°C the threshold gain temperature is 29°C. At a heat sink temperature of 60°C, a spectrum was recorded also close to the roll-over which indicates a roll-over temperature of about 119°C. Also, the spectral width can be correlated with the temperature gradient between the center and the edge of the gain region.

The validation of the above demonstrated shift-rate method has not only been carried out experimentally, but also from a theoretical point of view. The complementary work by Hader et al. enables a detailed discussion of potential error sources [40]. While the influence of the heat sink temperature is understood readily, it is more difficult to confirm the relation between the gain temperature and the pump intensity. The reason is that such investigation must quantify the individual contributions to the dissipated power, which can be written as a sum of non-radiative power P_{heat} and radiative powers P_{rad}

$$P_{\text{D}} = P_{\text{heat}} + P_{\text{rad}}. \tag{3.10}$$

Obviously, only P_{D} can be determined in the experiment and clearly a major part of the dissipated power is converted to heat. The generated heat itself is an accumulation of electron-electron and

Table 3.1. Summary of the quantities obtained from the thermal resistance measurement based on the shift-rate method.

	$\partial\lambda/\partial P_{\text{D}}$	$\partial\lambda/\partial T$	λ_0	R_{th}	R_{th}/f	$T_{\text{thr}}^{20°\text{C}}$	T_{ro}
Measured	0.1417 nm/W	0.1025 nm/K	1007.0 nm	1.38 K/W	1.41 K/W	29°C	119°C
P_{D} corr.	0.1551 nm/W	0.0964 nm/K	1007.2 nm	1.61 K/W	1.64 K/W	29°C	122°C

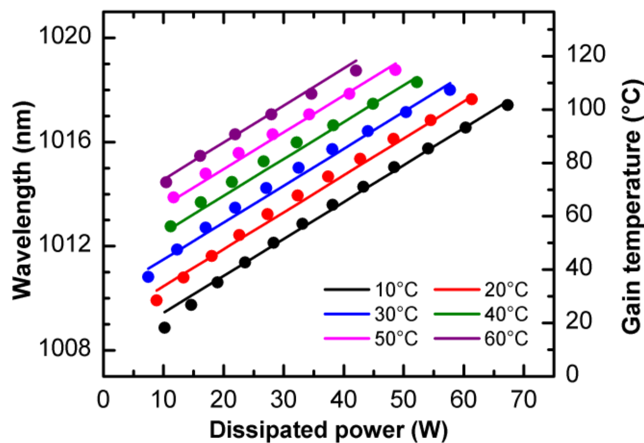

Figure 3.17. Result of the shift-rate measurement. Circles denote the measurement data, lines the plot of Eq. (3.7) with the solutions for the shift rates and the offset wavelength.

electron-phonon scattering. It is mainly depending on the quantum defect, Auger losses, and reabsorbed spontaneous emission. However, there are also significant radiative losses due to non-reabsorbed spontaneous emission and intra-cavity scattering of the laser radiation. These losses do not contribute to heat. In other words, the use of P_{D} in Eq. 3.7 causes an underestimation of $\partial\lambda/\partial P_{\mathrm{D}}$ which in turn, according to Eq. 3.8, causes an underestimation of the thermal resistance. It is further discussed that the error is dominated by the intra-cavity scattering losses, e.g. due to scattering at the chip interfaces. These losses are pronounced, if low mirror transmissivities are employed. From this point of view the 3.2 % transmissivity, which are used here, are still reasonable. Still, this can explain the underestimation of the measured resistance in comparison with the simulation (cf. Fig. 2.10).

In order to account for the dominant intra-cavity losses, Hader et al. suggest to perform a series of thermal resistance measurement but with different mirror transmissivities. The dissipated power is written as

$$P_{\mathrm{D}} = P_{\mathrm{pump}} - P_{\mathrm{out}}\left(1 + \frac{\alpha_{\mathrm{SS}}}{\alpha_{\mathrm{out}}}\right). \tag{3.11}$$

with the intra-cavity scattering loss α_{SS} and the mirror transmissivity α_{out}. In this way, the power which is lost due to spontaneous emission is still neglected, but it is taken account for the dominant intra-cavity scattering loss. Nakdali et al. used this approach to measure the scattering losses with a low quality chip, i.e. the chip's surface quality was visibly impaired. A scattering loss of 1.5 % to 3.5 % was measured, depending on the used region on the chip [37], while Hader et al. report a scattering loss of 0.57 % for a clean chip [40]. It is expected that the present reference sample exhibits a very clean surface, because it was freshly processed for these investigations. However, the scattering loss of 0.57 % can be considered to obtain an approximation of the maximum error from the thermal resistance determination. Applying Eq. 3.11 and a scattering loss of 0.57 % to Eq. 3.7 yields shift rates of 0.096 nm/K, 0.155 nm/W, an offset wavelength of 1007.2 nm, and a thermal resistance of 1.61 K/W, respectively. The relative error between the original and the corrected thermal resistance is about 15 %. It is noteworthy that due to such error the gain temperatures are only slightly underestimated. An overview of these results is also shown in Tab. 3.1, in the row labelled with row labeled with "P_{D} corr.", respectively.

Roll-over method

In a high-power experiment with multiple transverse mode operation, it was recognized that the thermal roll-over occurs first at the center of the pumped gain region while the outer regions still lase [20]. This is in accordance with the above considerations; laser operation ends first at a specific maximum temperature at the hot center of the pump profile while lasing is still observed at the colder outer regions. Furthermore, it was discovered that the maximum gain temperature does not depend on the heat sink temperature [40, 43]. This relation can be used in order to drastically simplify a thermal resistance measurement. It can be shown that

$$T_{Hs} = T_{Roll} - R_{th}P_{D} \tag{3.12}$$

where T_{Roll} is the gain temperature at the point of roll-over. Such measurement can be performed quickly as no optical spectrum analyzer is necessary to acquire and analyze laser spectra. Only

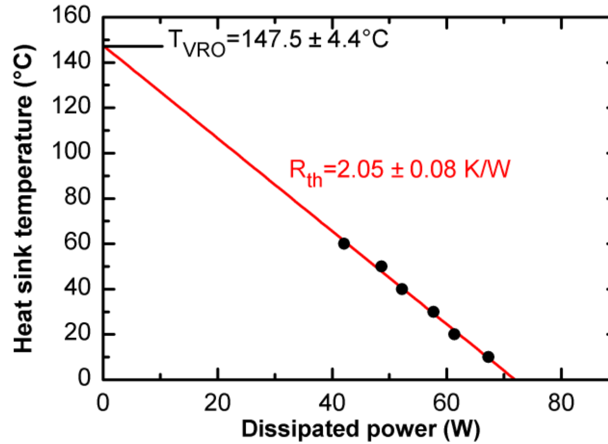

Figure 3.18. Result of the thermal resistance measurement based on the roll-over approach.

output powers, pump powers, and heat sink temperatures need to be recorded. As an example, such data is extracted from the power curves in Fig. 3.3. The obtained data is illustrated in Fig. 3.18. A thermal resistance of 2.1 K/W is obtained and a roll-over temperature of 148°C. Considering potential scattering losses of 0.57 % even lifts the result to 2.5 K/W and 165°C, respectively. The quite significant discrepancy in comparison with the shift-rate approach is not surprising. The reason is that the pump profile is almost a flat-top profile. In this case it may occur that enough output power is still generated from the outer regions of the pump spot while the center is rolling-off. This results in a rather flat power curve at the maximum output power. Furthermore, the power curves do not contain many points at this flat region, which results in a vague identification of the roll-over point. In summary, the approach can be used especially for Gaussian pump profiles to quickly determine the thermal resistance and if the temperature and power dependent shift rates are not of interest. The approach can only be applied if the roll-over temperature is independent of the heat sink temperature. In case of new designs, such behavior has to be verified, accordingly.

Virtual roll-over method

A compromise between the extensive shift-rate method and the fast yet occasional error-prone roll-over method is the virtual-roll over method which has been presented in [44]. It reflects exactly the roll-over approach, but an optical spectrum analyzer is used to overlap the emission spectra at a defined signal drop for different heat sink temperatures and pump powers. Then, Eq. 3.12 can be written as

$$T_{\mathrm{Hs}} = T_{\mathrm{G}} - R_{\mathrm{th}} P_{\mathrm{D}}, \tag{3.13}$$

i.e. T_{Roll} is replaced by the gain temperature T_{G} which corresponds to the chosen overlapped wavelength. Here, eight spectra were recorded for heat sink temperatures between 10°C and 80°C. The power was adapted to overlap the spectra at an intensity drop of 10 dB (cf. Fig. 3.19). Afterwards, the dissipated powers are plotted versus the heat sink temperatures. The linear regression yields a thermal resistance of 1.35 K/W and a gain temperature of 106.7°C (cf. Fig. 3.20). Considering intra-cavity scattering losses of 0.57 % yields 1.51 K/W and 109.6°C, respectively. In

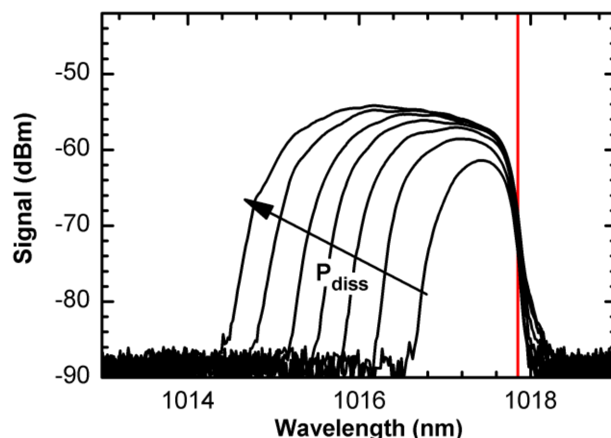

Figure 3.19. Illustration of the virtual roll-over method. The spectra are recorded at heat sink temperatures between 10°C to 80°C (10°C steps), pump powers are adjusted to overlap the spectra at a 10 dB drop.

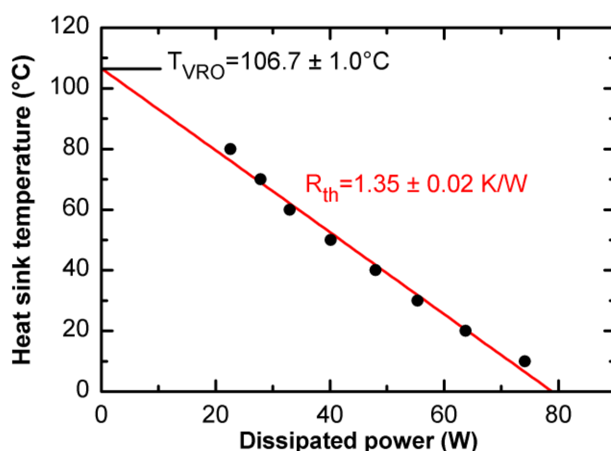

Figure 3.20. Dissipated powers and heat sink temperatures corresponding to the spectra in Fig. 3.19.

comparison with the shift rate method, it can be seen that the measurement was performed close to the thermal roll-over. The relative error of the thermal resistance with respect to the shift rate method is 6.2 % which indicates a good agreement.

3.6 Summary

In this chapter, the fundamental characterization methods for flip-chip bonded VECSELs have been presented by means of a reference structure. Power characteristics of the sample dependent on different output couplers and heat sink temperatures were investigated, followed by a detailed characterization of the reflectivity, longitudinal confinement factor, and edge PL. In this way, a room temperature detuning of -14 nm was determined. Furthermore, the detuning analysis enables a detailed comparison with chip design which has been realized precisely in case of the reference sample. A gain measurement setup was presented, which confirmed gain values of about 10 % and threshold densities in the low kW/cm² regime. Also, a detailed analysis of the thermal resistance has been performed by means of three different measurement techniques. In conclusion, this chapter has not only presented experimental methods which will be used to characterize VECSELs throughout this thesis, but also yields a full set of data for the reference structure. This data will be

used for detailed comparisons with other VECSEL structures and will help to understand and reveal potential issues. In order to simplify the comparisons, all results are summarized in Tab. 3.2.

Table 3.2. Summary of the fundamental laser analysis of the reference sample.

Reference structure

Cap	$\lambda/2$ $Ga_{0.52}In_{0.48}P$
Barriers	11 x $\lambda/2$ $Ga(As_{0.97}P_{0.03})/GaAs$
Quantum wells	10 x 7.4 nm $(In_{0.24}Ga_{0.76})As$
DBR	22.5 pairs of $\lambda/4$ $AlAs/(Al_{0.1}Ga_{0.9})As$

Pump spot

FWHM	740 µm × 825 µm
Super-Gaussian factor *m*	2.73
R_{th} correction *f*	0.98

Power curves (3.2% trans., 10°C heat sink temp.)

Threshold intensity	1.0 kW/cm²
Max. output power	35.3 W
Slope efficiency	44.7 %
Max. mirror trans.	9.0 %
Emission wavelengths	1007 nm – 1019 nm

Room temperature detuning

LCF λ_{LCF}	1011 nm
Edge PL λ_{PL}	997 nm
Detuning $\Delta\lambda$	-14 nm

Gain measurements (20°C)

Maximum gain G	10 %
Threshold intensity	~ 0.5 kW/cm²

Thermal resistance measurements

Method	**Shift-rate**	**Roll-over**	**Virtual roll-over**
R_{th}/f	1.41 K/W	(2.1 K/W)	1.38 K/W
Corr. R_{th}/f	1.64 K/W	(2.5 K/W)	1.54 K/W
T_{Ro}	119°C-122°C	(148°C-165°C)	>107°C
T_{thresh} (T_{Hs}=20°C)	29°C	-	-

4. Detuning dependent performance of quantum well VECSELs

Besides the well-studied effect of thermal management or the development of efficient gain media, only little attention has yet been paid to one other key design parameter, namely the spectral detuning between micro-cavity resonance and material gain as it was introduced in chapter 2.

Indeed, the detuning is not a critical parameter for every VECSEL design. For some applications, it is reasonable to apply an *anti-reflection coating* to the cap layer. A common coating is for instance a bilayer of Si_3N_4 and SiO_2 [81]. The thickness of such coatings is designed to obtain a node of the light field at the chip's surface and at the respective laser wavelength. In analogy to a poor mirror reflectivity in a Fabry–Pérot etalon, the coating reduces the finesse of the micro-cavity which results in a reduction of the LCF. A demonstration of this effect is illustrated in Fig. 4.1. A transfer-matrix calculation of the coated reference structure is carried out and compared with the regular, resonant design. The modified LCF reaches its maximum at about 1.3 which implies a reduction of the modal gain by a factor of three. In exchange for that, the FWHM of the broadened peak is about 40 nm. Therefore, the resulting modal gain of the chip is flattened which makes the laser less sensitive to a change in gain temperature and the VECSEL can operate at the material gain maximum. For such VECSLEs, it is not necessary to indicate a detuning. Furthermore, it is observed that, in comparison with the regular chip, the LCF is increased at the short and long wavelength tails which results in an improved tunability. Additionally, the thickness of the anti-reflection coating can be designed to minimize the chip's group delay and third order dispersions, which is necessary particularly for mode-locking applications. Not by chance, the anti-reflection coating was discussed as key parameter to achieve pulse durations as low as 100 fs [34].

An alternative to a coating is obtained by the choice of an *anti-resonant design*, where the cap layer thickness is $\lambda/4$ instead of $\lambda/2$ as for instance in the discussed reference sample [11]. The resulting transfer-matrix calculation for the reference structure is also shown in Fig. 4.1. In comparison with the coated chip, the LCF maximum is completely removed, but two small resonances occur at the lower and longer wavelengths. Remarkable results concerning mode-locking have been achieved also with this design, e.g. sub-picosecond VECSELs with peak output powers up to 4.35 kW [54].

Analog considerations are also applicable for VECSELs with silicon carbide or diamond *intra-cavity heat spreaders* which are attached to the cap layer, usually by liquid capillary bonding [82]. These designs are favorable in the presence of many-layered DBRs, which are often inevitable at wavelengths in the visible regime or at longer wavelength in the mid-infrared regime [83, 84]. The heat spreader reduces the refractive index contrast at the chip's surface which reduces the finesse of the micro-cavity, and further on, the heat spreader is usually anti-reflection coated in order to avoid Fabry–Pérot resonances.

The bottom line is that the modal gain can only be maximized by the application of resonant designs. The alternative designs provide other features like an improved modal gain width and a minimized group delay dispersion, but impair the magnitude of amplification. This understandable assertion has also been verified in a theoretical comparison of an anti-reflection coated and resonant structure [81]. However, it is noteworthy that at some specific conditions an anti-reflection coating can also surpass the resonant design. Anyhow, a reduction of the modal gain is not acceptable for every application. For instance, resonant designs were employed to demonstrate the above-mentioned record output powers of 100 W in multiple transverse mode operation [20], and 23 W in single-

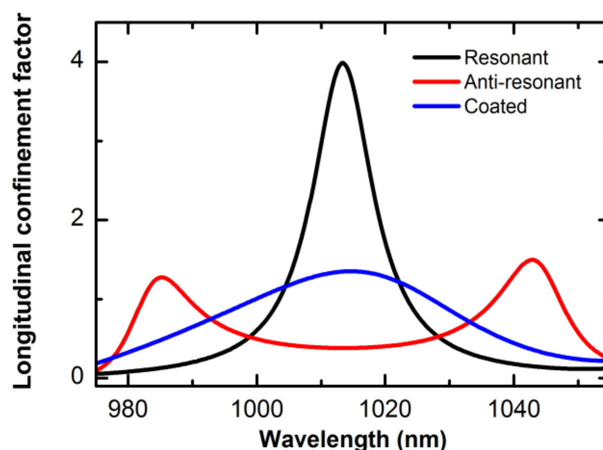

Figure 4.1. Comparison of the longitudinal confinement factor in resonant, anti-resonant and anti-reflection coated designs.

frequency operation [63]. Latter case implies that a resonant design should also be favored for intra-cavity frequency-conversion, where high intra-cavity fields and a mode with narrow line-width are required and substantial optical losses are introduced to the laser cavity [13]. Nevertheless, the choice of the "correct" detuning is not readily specified. The reason is that material gain is a product of many entangled influences, as for instance the carrier density, gain temperature and their connection with the radiative as well as non-radiative losses. A notable consequence is that the pump densities and gain temperatures at threshold or thermal roll-over, which play an important role in the detuning choice, are hardly foreseen.

A detailed theoretical analysis of the detuning dependent performance of structures emitting at 1 µm is theoretically studied by Hader et al. [32]. A fully microscopic many-body theory is used to calculate the microscopic gain properties. Rate-equation models are used to also account for the macroscopic heat-, carrier- and light dynamics. Input parameters are experimentally identified for an 808 nm pumped high-power VECSEL with emission wavelengths around 1040 nm. Such parameters are for instance the pump spot profile, the thermal resistance, but indeed also include the complete structural data of the VECSEL. The analyzed chip exhibits 10 (GaIn)As QWs, which are separated by Ga(AsP) barriers, and a 20 × AlAs/GaAs DBR. Moreover, the structure is soldered onto a diamond heat spreader. The thermal resistance was measured to be 4.3 K/W with a pump spot size of 550 µm (FWHM). With the experimental data fed to the theoretical model, reflectivity, PL measurements, and power curves could be well reproduced. On this basis, individual design properties are modified in the model in order to investigate the influences on the chip's performance. These modifications include the number of QWs, the reflectivity of the solder for the 808 nm pump light and most important in this context also the detuning. The results represent very well what can be observed in the experiment. While VECSELs with a small detuning exhibit low thresholds, devices with a large detuning delay the thermal roll-over and deliver significantly higher output powers. Consequently, an "optimized detuning" is a matter of the intended application. However, the study does not only indicate tendencies but enables a quantitative specification of a "small" or "large" detuning for low thresholds or high output powers, respectively. For instance, if the detuning is in a range between 10 nm to -5 nm, no significant impact on the threshold pump intensity is observed. In contrast, the output power is 30 % higher at a detuning of -5 nm and in comparison with the 10 nm detuning. Due to the low threshold, such detuning can be referred to as a small detuning. If the negative detuning is further increased, even up to -40 nm, there is also a significant impact on the threshold density. In comparison with the -5 nm detuning the threshold is

quadrupled and the output power is increased by approximately 35 %. Hence, such detuning can be referred to as large.

An existing experimental study of the detuning is based on the non-uniformity of the MOVPE growth in a planetary reactor [41]. Due to a slightly different growth ambient among different wafers, most importantly a temperature gradient within the reactor, different layer compositions and thicknesses are obtained. Although such variations are not dramatic, both the emission wavelength and the LCF resonance wavelength are sufficiently altered to result in an inherent variation of the detuning. This was demonstrated by TDR measurements of three VECSELs from three different wafers. The samples reveal clearly different absorption characteristics within the stop band which can be assigned to their different detuning (-12 nm, -18 nm, and -34 nm). Maximum output powers of 23 W, 57 W and 73 W are achieved with these structures, respectively. This is a remarkable demonstration of the impact of the detuning as the output power is more than tripled by only adjusting the detuning.

However, not for every structure such convenient set of chips is available. Many structures are grown at a smaller scale in exploratory MOVPE reactors or by MBE which do not cast off a set of different wafers. Furthermore, it is desired to perform a study which can clearly exclude any other parameter. One critical parameter is for example the chip quality. The presented experimental study was based on bottom-emitters [41]. Although bottom-emitters involve the discussed advantages they pass a lot of steps during the processing. This might end up in a variation of the bond quality, the surface quality, or the thermal connection between the chip and the heat sink, which can be well summarized in the term “chip-to-chip fluctuations”.

And yet, no complementary experimental study has been performed, where the influence of the detuning can be taken into account as the sole parameter for the change in the performance. This chapter presents an approach which exploits that the VECSEL can be arranged as a folding mirror of the resonator in a V-cavity. The connection between the opening angle of the cavity, i.e. the angle of incidence on the chip’s surface, and the micro-cavity resonance is calculated and exploited to manipulate the detuning. The investigation shows that by altering the cavity-angle dependent detuning, the device's performance can be modified significantly which is only due to a change of the detuning. The goal of this study is to quantify the implication of the detuning and demonstrate a meaningful experimental technique for VECSEL characterization and optimization.

It is noteworthy that the considerations in this chapter, including the above discussed references, only deal with flip-chip bonded structures with an emission wavelength of about 1 µm. Clearly, a great variety of different designs has been realized since the invention of the VECSEL in the late 90’s. Different gain materials, quantum defects, or heat spreading techniques are just a few examples of design parameters with great impact on the temperature and pump intensity dependent shift rates. Therefore, an optimized detuning is very much depending on the device. The below described technique gives access to a detuning study for any chip design. Hence, it will be also applied in the context of the type-II VECSEL as presented in chapter 6.

4.1 Basic theoretical considerations

In order to find an approximation for the connection between angle of incidence and LCF resonance shift, a simple model is presented in the following. It is assumed that the VECSEL can be considered as a regular Fabry–Pérot etalon with the thickness d and the refractive index n. Furthermore, it is sufficient to restrict the considerations to the phase of two plane waves. The phase difference of a reflected plane wave for normal incidence ϕ_p and a reflected plane wave with oblique incidence ϕ_o is

$$\Delta\phi = \overrightarrow{k_p}\,\overrightarrow{r_p} - \overrightarrow{k_o}\,\overrightarrow{r_o}\,. \tag{4.1}$$

with the respective wave vectors $\vec{k}_{p,o}$ and position vectors $\vec{r}_{p,o}$. It is of interest how one specific point in a reflectivity spectrum shifts in dependence on the angle of incidence φ_1. The observed point in the spectrum may be $(\lambda_p,\ R)$ for normal incidence which shifts to (λ_o, R) for oblique incidence. In other words, the wavelength has to change in such a way that the same phase in comparison with normal incidence is found. This yields the condition

$$\Delta\phi = 0\,. \tag{4.2}$$

The path length $|\overrightarrow{r_o}|$ is well known from the discussion of Fabry–Pérot etalons in textbooks [85]. With help of trigonometric relations, it can be shown that

$$|\overrightarrow{r_o}| = 2dn\cos(\varphi_2). \tag{4.3}$$

with the angle of refraction φ_2. Using Snell's law, φ_2 can be substituted by

$$\varphi_2 = \arcsin\left(\frac{\sin\varphi_1}{n}\right). \tag{4.4}$$

A more handy expression is obtained using the identity [50]

$$\cos(\arcsin x) = \sqrt{1 - x^2} \tag{4.5}$$

which results in

$$\phi_o = \overrightarrow{k_o}\,\overrightarrow{r_o} = \frac{4\pi dn}{\lambda_o}\sqrt{1 - \left(\frac{\sin\varphi_1}{n}\right)^2}\,. \tag{4.6}$$

It is worth to note that Eq. 4.6 equals the phase of a plane wave with normal incidence times a factor γ. Hence, the phase difference depends only on this factor

$$\gamma(\varphi_1, n) = \sqrt{1 - \left(\frac{\sin\varphi_1}{n}\right)^2} \leq 1. \tag{4.7}$$

Using Eq. 4.1 and Eq. 4.2 results in

$$\lambda_o = \lambda_p\, \gamma(\varphi_1, n). \tag{4.8}$$

This relation describes at which wavelength λ_0 the same phase as for the normal incidence with λ_p is obtained. Because $\gamma(\varphi_1, n) \leq 1$, a blue shift is observed for any angle $0 < \varphi_1 < 90°$. A simple expression for the difference wavelength in comparison with normal incidence is

$$\Delta\lambda = \lambda_p(1-\gamma) \tag{4.9}$$

The γ parameters is illustrated as a series of refractive indices in Fig. 4.2. Because a VECSEL chip's reflectivity, longitudinal confinement factor, and group delay dispersion are interference phenomena, basically depending on the wave's phases, it is expected that these quantities will experience the wavelength shift described by Eqs. 4.7-4.9.

A comparison between the measured reflectivity and the reflectivity calculated with the transfer-matrix of the reference sample for normal incidence (top) and 30° angle of incidence (bottom) is represented by Fig. 4.3. In the transfer-matrix calculation, the angle dependence can be readily considered by the angle dependent propagation constant as described by [11]

$$k_j = \frac{2\pi}{\lambda} n_j \cos\left[\arcsin\left(\frac{n_{j-1}}{n_j}\sin\varphi_j\right)\right] \tag{4.10}$$

where j indicates the layer number. This relation can be obtained similar to the previous procedure. The observed blue shift of the reflectivity spectrum amounts to -10 nm. Another important observation is that the measured absorption dip within the stop band is more pronounced for the 30° angle. This is explained by the blue shift of the longitudinal confinement factor resulting in a stronger overlap with the gain spectrum, which is also illustrated in Fig. 4.3. It is shifted by -10 nm which therefore modifies the room temperature detuning to -4 nm. The relative absorption of ~ 40 % is comparable to a measurement at normal incidence and a heat sink temperature of 60°C at which also an effective detuning of -4 nm is observed, considering the measured QW and LCF shift rates of 0.34 nm/K and 0.08 nm/K, respectively. The result can also be compared to the

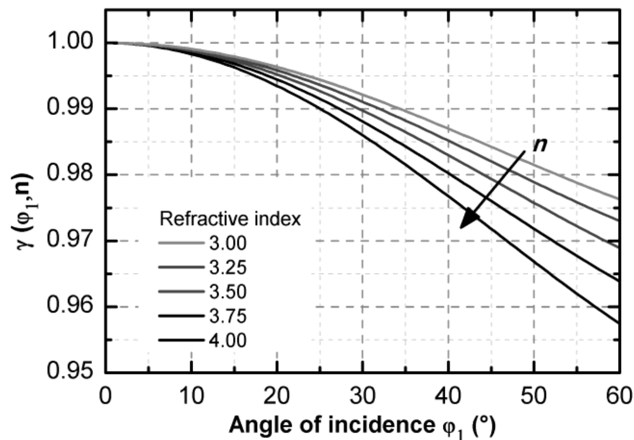

Figure 4.2. Illustration of the function γ which describes the change of the phase of a plane wave which is reflected by an etalon.

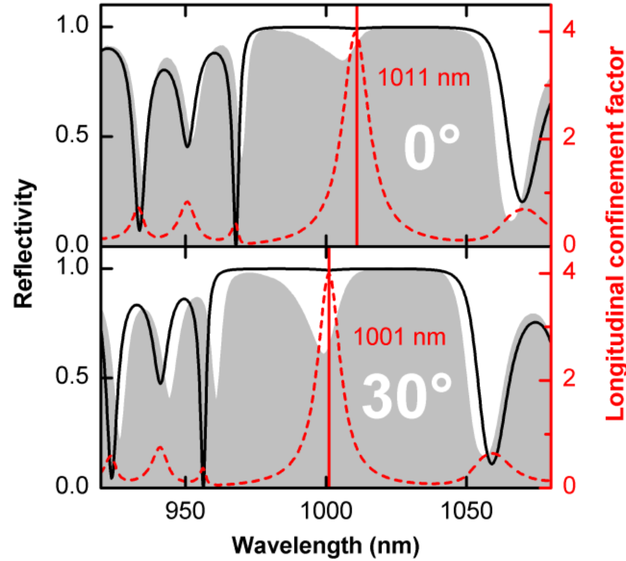

Figure 4.3. Measurement (gray) and ray transfer-matrix calculation of the reflectivity for normal incidence and 30° angle of incidence (left axis). Also shown are the calculated longitudinal confinement factors for the corresponding angles (red, right axis).

determination of a wavelength shift according to Eq. 4.8 with the refractive index 3.5, which is close to the average refractive index within the RPG. The result for λ_0 is 1000.6 nm, which is in agreement with the ray transfer-matrix calculation.

4.2 Experimental study of the detuning dependent performance

In the following, the angle dependence of the longitudinal confinement factor is exploited to investigate the impact of the detuning. A VECSEL chip is arranged as folding mirror in a V-shaped cavity as shown in Fig. 4.4. The application of different angles results in different room temperature detunings. Referring to the above discussed study by Hader et al. [32], a change of the detuning should be most significant between -40 nm and -15 nm where a great influence on threshold intensities and maximum output powers is observed. However, the preliminary considerations show that a change of the angle only results in a blue shift of the LCF. This implies that the effective negative detuning can only be decreased in such an experiment. Therefore, it is favorable to choose a sample with a large negative detuning which then can be reduced by increasing the cavity's angle.

The sample which is chosen for the investigations here was recently used for the demonstration of 23 W singe-frequency operation [63] and, in particular, it is from the same wafer as the structure used for the demonstration of 106 W from a single gain chip [20]. These remarkable results indicate that such sample could exhibit a large negative detuning. In addition, the structure is very similar to the chips of the previously discussed studies [32, 41]. Overall, the structure is very similar to the reference sample as can be seen in Tabs. 3.2 and 4.1. It exhibits a similar cap layer, RPG and heat spreader. Furthermore, the structure is also flip-chip bonded onto a 350 µm thick diamond heat spreader. Still, there are differences between the reference sample and sample 4.1 which should be considered.

One difference is the binary AlAs/GaAs DBR instead of the ternary AlAs/(AlGa)As DBR. The major difference between the binary and the ternary DBR is not the reflectivity but their distinct

Table 4.1. Summary of the composition of the chosen sample for the detuning investigation.

Sample 4.1	
Cap	$\lambda/2$ $Ga_{0.52}In_{0.48}P$
Barriers	11 x $\lambda/2$ $Ga(As_{0.97}P_{0.03})/GaAs$
Quantum wells	10 x 8 nm $(In_{0.18}Ga_{0.82})As$
DBR	22.5 pairs of $\lambda/4$ AlAs/GaAs

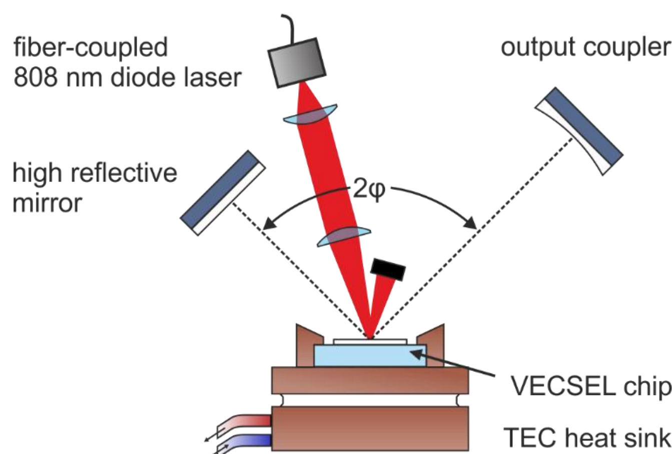

Figure 4.4. Scheme of the V-cavity arrangement for the detuning investigation.

contribution to the chip's thermal resistance. The binary DBR involves absorption of the 808 nm pump light but exhibits a lower thermal resistance. In contrast, the ternary DBR is transparent at 808 nm but the ternary material induces a poor thermal conductance [86]. A detailed comparison of these different designs was carried out in [44, 87], where the thermal resistances were measured and compared with finite element simulations. It could be demonstrated that the binary DBR outperforms the ternary DBR. Still, the thermal resistances of the structures are very similar. At a FWHM pump spot size of 300 µm the simulated thermal resistances are 2.1 K/W and 1.7 K/W for the reference structure, and sample 4.1, respectively. Furthermore, in chapter 2 it is demonstrated that the thermal resistances for different chips at different emission wavelengths are also very comparable (cf. Fig. 2.10). Concluding, the results obtained in this chapter can be well transferred to similar chip's but with ternary DBRs and at different emission wavelengths between 900 nm and 1300 nm.

Indeed, *another difference* is the slightly different barrier width which results in a different detuning. The experimental methods presented in section 3.3 are applied to determine the detuning precisely. Only the edge PL measurement is somewhat complicated due to the absorption of the 808 nm in the binary DBR. Thus, a wafer piece is glued onto the edge of a sapphire plate and the substrate is removed by mechanical thinning and wet chemical etching. This procedure is very similar to the flip-chip bonding process described in section 3.2.

It is not surprising that similar PL spectra are observed in comparison with the reference structure. For brevity, only the evaluation of the peak wavelength for the temperature and power dependent measurements are shown in Fig. 4.5. It is demonstrated that the low excitation density peak wavelength is 995 nm (cf. Fig. 4.5 a)). The temperature shift rate is 0.33 nm/K which differs only by 0.01 nm/K from the previously measured value for the reference structure (cf. Fig. 4.5 b)).

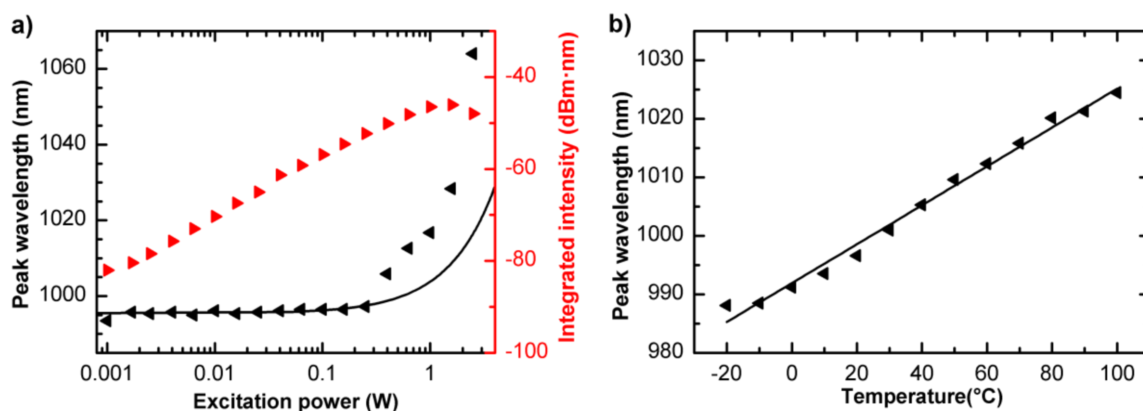

Figure 4.5. a) Evaluated peak wavelength of the power dependent and b) temperature dependent edge PL measurements of sample 4.1.

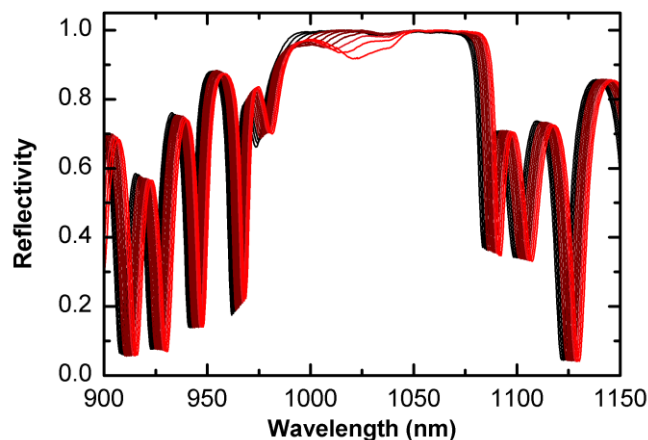

Figure 4.6. Temperature dependent reflection of sample 4.1 for temperatures between -20°C and 100°C and in 10°C steps.

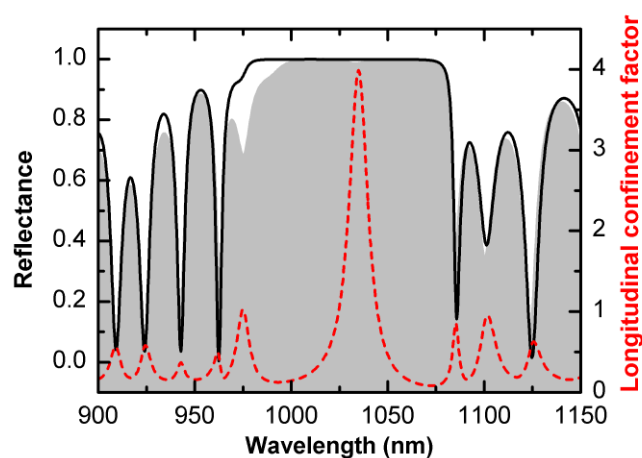

Figure 4.7. Comparison between the measured (gray area) and calculated reflectance (black solid line) of sample 4.1. Also shown is the resulting longitudinal confinement factor (red dashed line) with a peak wavelength of 1035 nm.

Considering the almost identical QW design with indium contents of 18 % as well as the thicknesses of 8 nm, the difference of 2 nm between the peak wavelengths is reasonable.

An impression of the sample's large negative detuning is sustained from the temperature dependent reflection measurements. Throughout the holder temperatures from -20°C to 100°C only a weak absorption dip is observed within the stop band (< 10 %). Consequently, QW absorption and longitudinal confinement factor are not even close at 100°C. This interpretation is readily evidenced by the transfer-matrix calculations (cf. Fig. 4.7). The relative errors between the design and simulated cap and DBR layer thicknesses are less than 1 %. A remarkable agreement between the measured and simulated reflectivity is observed. It is revealed that there is a pronounced absorption dip at the low wavelength edge of the stop band at 997 nm, where a side peak of the LCF is present. However, at the main peak position of 1035 nm, there is no significant modal absorption, obviously due to the lack of material absorption. Accordingly, the detuning is -40 nm which is exactly the suggested detuning for high-power operation [32].

As last step prior to the actual experiment, the longitudinal confinement factor is calculated in dependence on the cavity angle (cf. Fig. 4.8). The result is also compared with Eq. 4.8 ($n = 3.5$, $\lambda_n = 1035$ nm). A good agreement is found which suggests that the approximation can be used for a precise determination of the angle dependent detuning also for other resonant structures. The integrated table also summarizes the resulting room temperature detunings at angles of incidence of 15°, 30° and 45°, respectively. These angles are chosen because they are practical in an experiment.

Next, the sample is arranged in a V-cavity as illustrated above. A plane 3 % output coupler and a highly reflective mirror with a radius of curvature of -250 mm are used to build the V-cavity. To align the cavity with different angles φ, the plane mirror remains fixed, while the VECSEL chip is rotated and the high reflective mirror is rearranged. As in any other setup in this thesis, the VECSEL is optically pumped by a fiber coupled 808 nm semiconductor diode laser. In contrast to the studies in chapter 3, a 120 W pump laser is employed instead of a 400 W laser. Due to the smaller fiber diameter of 200 µm, 1/2" lenses can be used for the pump optics in comparison with the 600 µm fiber and 1" lenses. Only in this way collisions with the laser mirrors can be avoided. For the

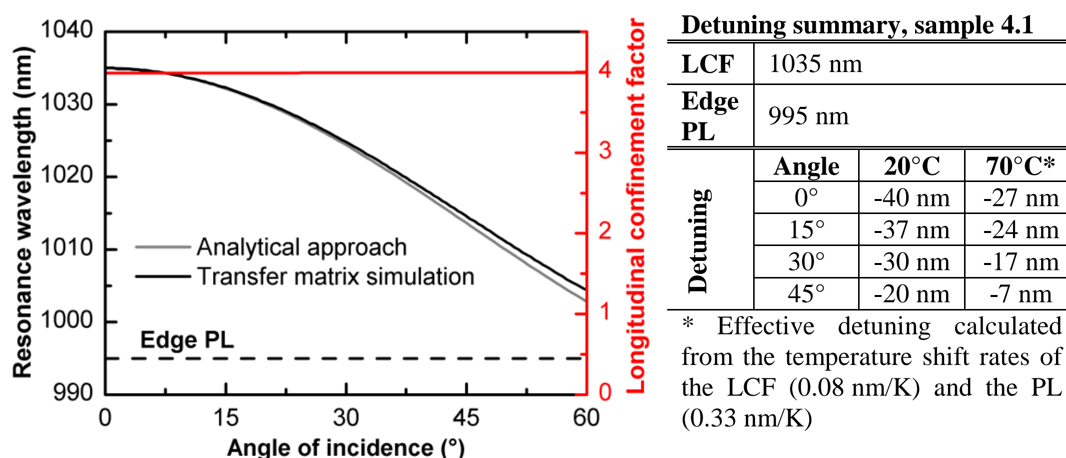

Detuning summary, sample 4.1

LCF	1035 nm		
Edge PL	995 nm		
Detuning	**Angle**	**20°C**	**70°C***
	0°	-40 nm	-27 nm
	15°	-37 nm	-24 nm
	30°	-30 nm	-17 nm
	45°	-20 nm	-7 nm

* Effective detuning calculated from the temperature shift rates of the LCF (0.08 nm/K) and the PL (0.33 nm/K)

Figure 4.8. Peak wavelength of the longitudinal confinement factor calculated with the transfer-matrix method (black, left axis) and the trigonometric approach from section 4.1 (gray, left axis). The red line demonstrates constancy of the LCF's magnitude, also calculated with the transfer-matrix approach (right axis). The integrated table summarizes the room temperature detuning as well as the effective detuning at a temperature of 70°C for different angles.

different cavity angles, the pump optics are realigned to maintain the relatively large pump spot with a diameter of 670 µm. In principle, it is desired to investigate the laser's performance from the lasing threshold to the thermal roll-over. Yet, due to the large detuning of the present sample, the thermal roll-over cannot be reached at a heat sink temperature of 20°C even with the maximum pump power of 120 W. One approach to overcome this limitation is to reduce the pump spot size, which increases the pump density. However, the laser will purely operate on fundamental transverse mode, if the pump spot size matches the TEM_{00} mode or is smaller than the mode on the VECSEL chip, which will be altered significantly with the change of the cavity angle. For instance, in a cavity with $\varphi = 15°$, the major axis of the TEM_{00} mode measures 420 µm and the minor axis 400 µm. When the cavity angle φ is increased to 45° and the cavity length remains unchanged, the major axis of the mode is increased to 570 µm while the minor axis remains 400 µm. From this perspective, in TEM_{00} operation it can be hardly observed whether a change in the performance is due to a different overlap with the pump spot or due to the detuning. In contrast, this can be handled well with a relatively large pump spot for which high-order TEM_{nm} mode operation is obtained. Thereby, the higher-order transverse modes fill in the complete pump spot even if the indices of the involved TEM_{nm} modes are changing with the cavity angle. In order to reach the thermal roll-over with this large pump spot the heat sink temperature is increased to 70°C. At this heat sink temperature, the effective detuning is changed to -27 nm but it has been demonstrated that the roll-over temperature is independent from the heat sink temperature [40, 44]. This implies that measurements at elevated heat sink temperatures can be correlated to the roll-over behavior of the same chip at any lower heat sink temperature.

As a first detuning investigation, the power curves are recorded at angles of 15°, 30° and 45°. It is noteworthy that a linear cavity with $\alpha = 0°$ is excluded from the investigations, because the number of optical passes through the gain region in the resonator would be halved. Therefore, it must be expected that inherent optical scattering losses α_{loss} at the chip's interfaces play a pronounced role. Consequently, this would result in a different effective roundtrip gain and an inclusion of linear cavity with 0° angle of incidence could only be accomplished if the $\alpha_{loss}/\alpha_{mirror}$ ratio is determined precisely. However, due to the small difference of the detuning (3 nm) between the 0° and the 15° angle, no significance of such comparison is expected anyway.

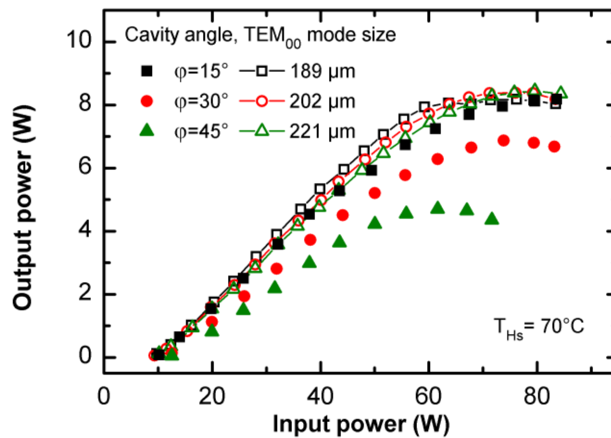

Figure 4.9. Plots of the power curves recorded at different angles (filled symblos). Open symbols represent the control experiment with a fixed cavity angle but different cavity length, which result in different pump spot to TEM_{00} mode size ratios, respectively.

For the selected cavity angles, the measured output powers are plotted as a function of input power in Fig. 4.9. In the case of 45°, the output power reaches its maximum of 5.2 W at an input power of 61.6 W. As the cavity angle is decreased to 30°, the detuning is increased and therefore the thermal roll-over is delayed to an input power of 73.8 W. Accordingly, the maximum output power amounts to 7.6 W. In the case of 15°, as a result of the further enlarged detuning, the maximum output power is just achieved at the maximum available input power of 83.6 W. With the output power of 8.2 W this configuration clearly marks the best performance. By comparing the maximum output power of 45° and 15°, an increment over 70 % is noticed, which proves the importance of the detuning concerning high-power operation of resonant VECSELs. Surprisingly, the thresholds in the three cases do not differ notably. However, the main reason for that is, at such low pump powers that the heat sink temperature of 70°C elevates the modal gain in all the three cases to a comparable level. A fair comparison of the thresholds is rather obtained at the heat sink temperature of 20°C. Here, the thresholds show significant differences, which are 25. W, 13.9 W, and 7.4 W, for 15°, 30° and 45°, respectively. The influence of the detuning is clearly pronounced. As the detuning decreases, less pump power is required to achieve enough overlap between the material gain and LCF to overcome the losses, which is to say, the lasing threshold is lower.

An important part of the experiment is to review the influence of the overlap between the pump spot with the transverse laser modes. As discussed above, a change of the angle deforms the elliptical transverse modes at the gain chip. On the other hand, the pump laser is carried along when the holder is rotated and the pump spot size is maintained. A legitimate question is hence, whether the different overlap causes a variation of the performance which is as significant as the influence of the detuning. In order to exclude such influence, the V-cavity with 15° is arranged and the cavity length is varied in order to obtain different ratios between pump spot size and TEM_{00} mode size. In this way, power curves for three ratios (272 %, 229 % and 196 %) are recorded which simulate the pump spot to mode size ratios for the 15°, 30° and 45° configurations at the constant cavity length of 230 mm. The obtained power curves are also shown in Fig. 4.9. The result is that the previously recorded power curve at 15° is essentially reproduced for all ratios. The small discrepancies between all four curves recorded at 15° are negligible in comparison with the great change of the performance at cavity angles of 30°, or 45°, respectively. This result proves that, when the pump spot is significantly larger than the TEM_{00} mode, their overlap has minor influence with respect to

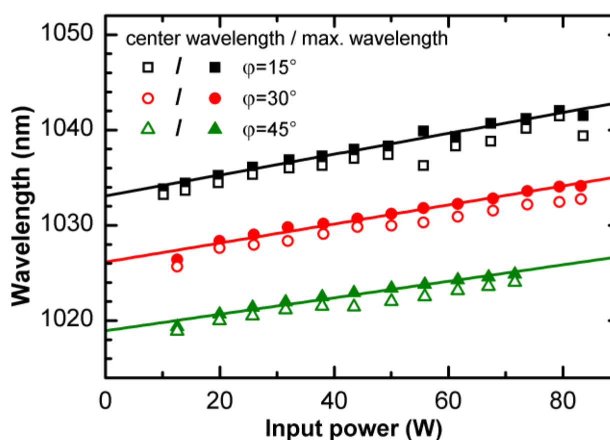

Figure 4.10. Power dependence of the maximum and center emission wavelength. The linear regressions exhibit slopes between 0.09 nm/K (45°) and 0.11 nm/K (15°).

the output power. The conclusion is that the detuning is the sole quantity to explain the observed angle dependent power dependences.

At each point, where the output power is recorded, the spectrum is recorded simultaneously by an optical spectrum analyzer. The maximum wavelength of each spectrum is defined as the wavelength where the amplitude of the peak drops by 10 dB on the long-wavelength side. This procedure is very similar to the principles discussed in line with the thermal resistance measurements in chapter 3. The maximum wavelength as a function of the input power is shown in Fig. 4.10. In the arrangement with φ = 45°, the maximum wavelength during operation ranges from 1019.4 nm to 1024.9 nm, while for 30° and 15° it ranges from 1026.4 nm to 1034.1 nm and from 1033.8 nm to 1041.5 nm, respectively. These different wavelength ranges are attributed to the altered sub-cavity resonance wavelength, which shifts to longer wavelength as φ is decreased. The slopes of the dotted lines in the figure indicate the shift rates of the maximum wavelength as a function of the dissipated power. For all three cases, the shift rates amount to approximately 0.11 nm/W, since the thermal characteristics of the setup remain unchanged throughout the experiment. The offset of the linear regressions are 1033.1 nm, 1026.2 nm, and 1018.9 nm which results in differences in the emission wavelength of about 7 nm and which is almost identical to the shifts of the LCF of 7 nm (15° to 30°) and 10 nm (30° to 45°).

Noticing the broad wavelength coverage resulting from a different detuning, it is of interest to investigate the wavelength tuning range. Therefore, a 1 mm thick birefringent filter (BRF) is placed in the respective cavities at its Brewster's angle and employed to tune the emission wavelength while the output power is recorded. Due to the introduced optical losses at the BRF, a mirror with 2 % transmissivity is chosen instead of the previously used 3 % in order to maintain a good output power level. For a fair comparison between the different angles, the tuning ranges are measured at a fixed input power of 49.1 W. The resulting plots with emission wavelength versus output power, as shown in Fig. 4.11, are an image of the chip's modal gain at the chosen conditions. For the cavity with φ = 45°, the center wavelength can be tuned from 1016.3 nm to 1033.3 nm, while for 30° and 15°, the tuning range covers 1022.6 nm to 1045.9 nm and 1029.6 nm to 1050.9 nm, respectively.

In fact, the different shapes of the tuning curves and the modifications in average output powers should also be attributed to the different detuning situations. Keeping in mind that the modal gain is a product of material gain and LCF it is concluded that their spectral overlap is improved at an

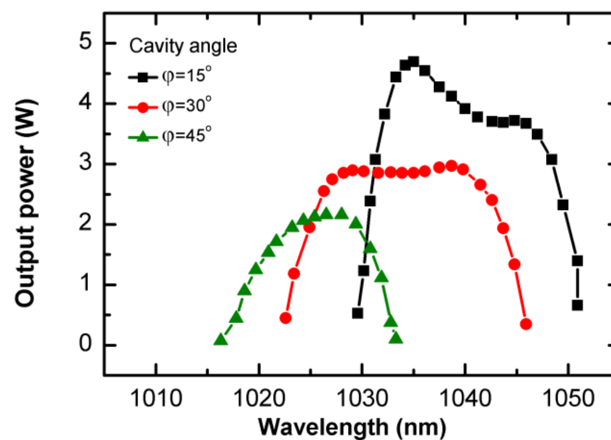

Figure 4.11. Tunability of the VECSEL at an input power of 49.1 W, a heat sink temperature of 70°C and at the different cavity angles. The curves are obtained by rotating a birefringent filter which is placed in the V-cavity at Brewster's angle.

angle of 15°, resulting in the highest average output power among the three cavities and a broad tuning range of 21.3 nm. In case of a 30° angle of incidence, the material gain peak is located at the same wavelength as for 15°, while the sub-cavity resonance is blue-shifted. Therefore, the overlap between material gain and LCF is reduced in comparison with the 15° arrangement. Correspondingly, the average output power is lower. However, due to the blue-shift of the sub-cavity resonance, the amplification of the material gain is improved at shorter wavelengths and overall the modal gain is slightly broadened (23.3 nm). Finally, since the detuning is small for the case of $\varphi = 45°$, the sub-cavity resonance is further moved to the short-wavelength side of the material gain peak. The overlap between the two key factors is the smallest, when compared to the other two cases. As a consequence, the output power is lower and the tuning range is the narrowest.

4.3 Summary

The general angle dependence of the reflectivity and the longitudinal confinement factor of VECSELs was discussed. On this basis, a method for the experimental investigation of implications due to the detuning was presented. A sample with a large negative detuning (sample 4.1) was characterized according to section 3.3 and its detuning was quantified. The sample was arranged as folding mirror in a V-shaped cavity of which the cavity angle was varied to obtain different detunings. A strong influence on the laser properties was observed by decreasing the amount of negative detuning from -37 nm to -20 nm. In this way, almost a factor of 2 is observed in the output powers, the threshold densities even change with a factor of almost 4. These results are in line with the above discussed studies [32, 41]. Furthermore, it can be expected that the threshold densities would be further decreased in case of an even smaller detuning. Following the trend of decreasing threshold with decreasing detuning, there is also a good agreement with the threshold of 1.0 kW/cm² in case of the reference sample with the detuning of -14 nm using extrapolation (cf. Tab. 3.2).

The results illustrate the necessity of detuning studies: A detuning of -40 nm seems quite large but still generates an improved output power in comparison to smaller negative detunings. Moreover, it is demonstrated that the reference sample can be considered as a “low threshold” sample, at least in comparison with sample 4.1. However, the range of accessible detuning was limited by the applicable maximum angle and the detuning of the sample at perpendicular incidence.

The presented V-cavity approach is conveniently applicable to many different samples. An outlook towards complimentary experiments is, thus, to employ very similar VECSELs with other detuning. To maintain a coverage of the possible reasonable detunings, the reference sample could be employed to further explore the threshold behavior. On the other side, a sample with an extreme amount of negative detuning, such as -60 nm could be used to experimentally identify the optimum detuning for high-power operation.

Other possible experiments include the investigation of VECSELs based on different material gain systems. In this chapter, it was demonstrated that the (GaIn)As QWs provide a high, broad material

Table 4.2. Summary of the detuning investigations on sample 4.1.

Angle	Detuning	Thresh. power / intensity	Output power	Tuning range
15°	-37 nm	25.6 W / 7.3 kW/cm²	8.4 W	1030 - 1051 nm, 21 nm
30°	-30 nm	13.9 W / 3.9 kW/cm²	6.9 W	1023 - 1046 nm, 23 nm
45°	-20 nm	7.4 W / 2.1 kW/cm²	4.7 W	1016 - 1033 nm, 17 nm

gain. Indeed, the performance can be modified to a great extent by only varying the detuning, but laser operation is still observed in any examined case. This might be very different for other gain media, as for example with (GaIn)As QWs at lower wavelength, i.e. with shallow QWs (cf. chapter 5). Then, it might be necessary to find the correct detuning just for reaching laser operation. Another detuning study is carried out in the course of this thesis with a type-II VECSEL structure (cf. chapter 6).

5. The development and characterization of VECSELs with novel emission wavelengths

Chapter 3 and 4 show examples of efficient VECSELs with emission wavelengths at about 1 µm. Lasing is observed at various operation conditions. In case of the reference sample, a high mirror transmissivity of up to 9 % could be employed (section 3.2), demonstrating a high material gain which was also confirmed by the gain measurements in section 3.4. Sample 4.1 was used to demonstrate the VECSEL's power dependence on the detuning. Although a significant impact was revealed, the sample was still operating at a wide range of detuning and at heat sink temperatures of 70°C (section 4.2).

Nevertheless, it is the VECSEL's great wavelength versatility which is one of the advantages over other lasers and which makes it a promising tool for many different applications. The realization of different emission wavelengths is accompanied by various challenges though. This chapter is dedicated to the investigation of barrier-pumped VECSELs for novel emission wavelengths by means of a wavelength range between 920 nm and 950 nm. The interest in such devices is not primarily driven by their fundamental emission, but by the possibility of highly efficient intra-cavity frequency conversion. In particular, there is a lack of blue lasers with decent output powers (> 1 W). Novel laser sources with a small device size and which can exceed 1 W of emission power, are GaN based diode lasers [88] or, as indicated, VECSELs utilizing a non-linear crystal for intra-cavity frequency doubling [13]. The remarkable potential of frequency-doubling into the visible regime has already been demonstrated by Kantola et al., who achieved output powers as high as 20 W at 588 nm [23]. Powers of up to 2 W could be achieved at a wavelength of 460 nm [89].

An important field of application for blue lasers is their use as compact light source in projectors [13]. Besides, the availability of efficient, high-power level blue lasers could boost the research on submarine near- to mid-range communication systems [90]. In laboratory environments, it is furthermore desired to replace bulky and inefficient devices, such as the argon ion laser, in fluorescence microscopy, or the widely spread photoluminescence spectroscopy.

The key issue in the supply of blue VECSELs is the development of gain media with fundamental emission wavelengths between 920 nm and 950 nm. It is of primary interest whether it is possible to transfer the above employed design strategies for devices at 1 µm (cf. chapter 3 and 4) to this wavelength range.

A bottleneck of 808 nm pumped devices is certainly the reduced quantum confinement of the charge carriers within the "shallow" QWs. Section 5.1 illustrates this concern and discusses suitable QW designs, including the corresponding band alignments and the potential non-radiative carrier loss. Section 5.2 then presents four laser samples based on the designs which will be investigated throughout the remaining parts of this chapter. Three samples are designed for the emission between 920 nm and 930 nm, another one is designed for the emission at 950 nm. The following studies are close to the procedure in chapter 3. As a first characterization the samples are investigated in a laser setup. However, it is anticipated that decent laser performance is only obtained with the 950 nm device (section 5.3). This finding calls for a more detailed comparison of the laser samples by means of reflectance and edge PL studies (section 5.4). At the same time the detuning is investigated which, referring to chapter 3 and 4, is also expected to be a key parameter here. Moreover, the modal gain of two exemplary samples is investigated in section 5.5. Based on that, the poor lasing

performance of a 920 nm VECSEL is discussed. Overall, the results of this chapter will yield a clear picture of the investigated samples, which enables an isolation of disadvantageous design properties. The results are summarized and an outlook is given, which will include suggestions for an optimization and realization of future VECSELs between 920 – 950 nm (section 5.6).

5.1 Quantum well design

Before QW designs for shorter emission wavelengths are discussed, it is reasonable to reconsider a typical design for emission at 1 µm. The 8 nm thick $(Ga_{1-x}In_x)As$ QW exhibits an indium concentration of $x = 20\ \%$ (cf. Fig. 5.1). For strain compensation the QW is embedded into $Ga(As_{1-y}P_y)$ barriers with a phosphorus concentration of $y = 3\ \%$. An important function of the barriers is also their high absorption at the desired pump wavelength of 808 nm. To a sufficient extent, this ensures the generation of charge carriers which can diffuse to the QWs and can recombine in an efficient radiative process. It is also illustrated that there is a heavy and light hole splitting in the band-structure, due to the compressive strain and the quantum confinement in the QW.

A PL measurement of a multiple-quantum well, containing ten of these heterostructures (10 × MQW), is shown in Fig. 5.2 (red). For comparison, the graph also comprises spectra of two other designs, which will be discussed later. All spectra were measured in a sequence and hence under comparable experimental conditions. A standard PL setup was used, employing a grating monochromator and a germanium detector in a lock-in scheme. All samples were excited continuous wave with an argon ion laser at 514 nm and at an intensity of 0.25 kW/cm². The PL was collimated and focused onto the monochromator by a pair of achromatic lenses. Only slight adjustments were carried out to ensure that the maximum signal is captured. In this way, a clear trend concerning the PL intensities can be extracted which confirms the following discussion: The intensity can be related to the QW depth.

In case of the typical design (cf. Fig. 5.1, left), the peak energy of 1.237 eV (1015 nm) can be related to the transition between the electrons and heavy hole states (cf. Fig. 5.2, red). The low energy side of the spectrum is formed by the QW density of states, the high-energy tail comprises the thermal distribution of electrons and holes as well as the recombination between electrons and light holes. Also the luminescence of the barrier layers is observed at 1.457 eV, which enables a more detailed

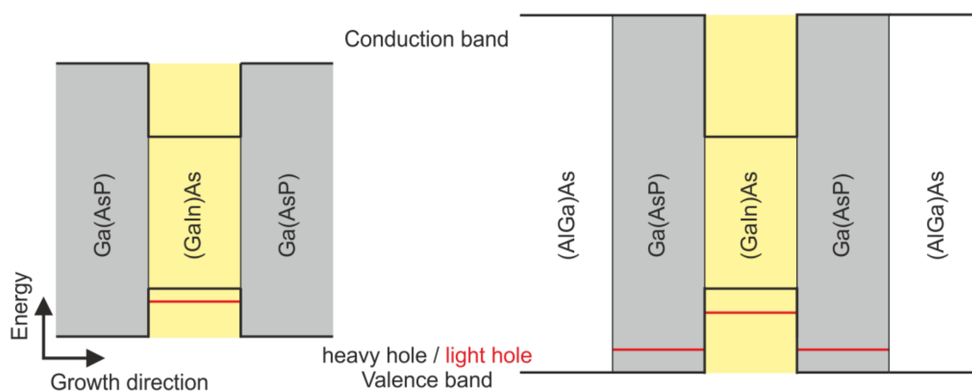

Figure 5.1. Illustration of a (GaIn)As QW with thick Ga(AsP) barriers (left) and with thin Ga(AsP) barriers as well as thick (AlGa)As separation layers (right).

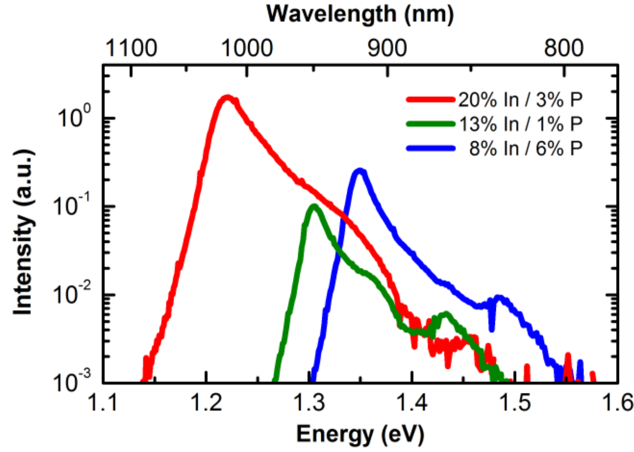

Figure 5.2. Photoluminescence measurements of 10 × MQWs with different QW depths. The excitation is at 514 nm and with an intensity of 0.25 kW/cm² for all three samples.

discussion of the design, since the energy difference of 236 meV between the QW and barrier luminescence can be related to the depth of the QW.

It is of importance that this energy difference is not evenly distributed to the valence and conduction band offsets (VBO, CBO). For the well-studied (GaIn)As/GaAs QWs, various different band offsets have been reported. A summary of experimental and theoretical results is given in [91]. The reported VBO ratios for the heavy hole in QWs range from 0.17 [92] to 0.60 [93]. However, there is a clear agglomeration of results suggesting VBO ratios between 0.3 and 0.4 [94–98]. Less studies are present in case of the (GaIn)As/Ga(AsP) system. A theoretical investigation of the band alignment for phosphorus concentrations of y = 5 % is provided by Zhang et al. [99]. Their results suggest VBO ratios of about 0.4. Overall, there is a clear tendency towards a smaller VBO ratio than 0.5 and it seems reasonable to consider ratios between 0.3 and 0.4 for a best- and worst-case scenario, respectively. Consequently, a VBO between 71 – 94 meV and a CBO between 118 – 138 meV is likely in terms of the 1015 nm MQW sample with x = 20 % and y = 3 %. The QWs can be referred to as “deep”, as it is neither likely for electrons nor for holes to escape into the barriers. Considering the Boltzmann distribution, a 1/e drop of the carrier density is at an energy of k_BT, which is ~25.4 meV at room temperature. However, for laser operation high carrier densities are required to obtain population inversion. Then, a quasi-Fermi distribution of the charge carriers is present and a potential loss due to a low barrier is even worse. Still, k_BT is fairly low in comparison with the VBO of > 71 meV and thus a good confinement of both, electrons and holes, is expected. A summary of the discussed band alignment is provided by Tab. 5.1 (bold font), which also yields a comparison with the band alignment in a hypothetical (GaIn)As/GaAs design (regular font).

A different situation is present if the band gap energy is further decreased by a reduction of the indium content within the QW. A PL spectrum of a 10 × MQW with x = 13 % and y = 1 % is also shown in Fig. 5.2 (green). The peak wavelength is 950 nm, the barrier luminescence is observed at 865 nm. The resulting energy difference is only 128 meV which is significantly smaller in comparison with the design for 1015 nm. Accordingly, the VBO is between 38 – 51 meV and the CBO is between 77 – 90 meV. The worst-case scenario for the VBO is hence only 38 meV which comes close to k_BT at room temperature (cf. Tab. 5.1). Such a QW can be referred to as “shallow”. It should be noted that, if such QW design is employed in a laser operating at room temperature, much higher temperatures have to be considered for the gain region. A typical gain temperature at

Table 5.1. Summary of possible band alignments in $(Ga_{1-x}In_x)As/Ga(As_{1-y}P_y)$ (bold) and the hypothetical $(Ga_{1-x}In_x)As/GaAs$ and QW heterostrucutres.

In x (%)	P y (%)	λ_{Peak} (nm)	E_{Gap} (eV)	E_{Barr} (eV)	ΔE (meV)	VBO 0.3 / 0.7 (meV)	CBO	VBO 0.4 / 0.6 (meV)	CBO
-	-	1010	1.226	1.424	198	59	138	79	118
20	**3**	**1015**	**1.221**	**1.457**	**236**	**71**	**165**	**94**	**142**
-	-	950	1.303	1.424	121	36	83	71	48
13	**1**	**950**	**1.305**	**1.433**	**128**	**38**	**90**	**51**	**77**
-	-	920	1.346	1.424	78	23	54	46	31
8	**6**	**919**	**1.349**	**1.485**	**136**	**41**	**95**	**54**	**82**

a decent power level is for instance 100°C, as measured in case of the reference sample (cf. section 3.5 and Tab. 3.2). According to a quasi-Fermi distribution of the charge carriers, it must be expected that carriers are thermally activated to escape from the QW into the barriers. The result is a drastically decreased probability for radiative recombination of the charge carriers within the QW.

The excessive thermal escape of carriers from shallow (GaIn)As/GaAs QWs was demonstrated in a combination of different experiments [100–102]. An established method is to measure the temperature dependent PL. The spectrally integrated intensity is plotted versus the inverse temperature on a half-logarithmic scale (also referred to as Arrhenius plot). A linear regression of the intensity drop yields the activation energy which is required for excitons to escape from the QW into the barrier. It was confirmed that the intensity of shallow QWs exhibits an early, pronounced drop-off which can be understood as a “spill-over” of charge carriers [100–103]. Furthermore, such studies were complemented by time-resolved PL measurements which indicate a clear reduction of the carrier lifetime of the QW states in shallow QWs. An additional part of the experiments was carried out by placing QWs with equal indium content but different width close to each other. Due to the different well depths, also different quantum confinements are provided. In the temperature dependent PL measurement, it was observed that carriers can be emitted from a shallow well and are recaptured by a deeper QW. Consequently, it was observed that while the intensity of the shallow well is decreased with increasing temperature, the intensity of the deeper well is enhanced.

It is to mention that such thermal emission of carriers from the QW impairs the material gain as the escaped carriers can neither contribute to spontaneous nor to stimulated emission. However, there is no explicit rule which specifies a minimum QW depth for either the VBO or the CBO. In literature, 4 – 5 k_BT is suggested [8], which is ~100 meV at room temperature, or “at least a few k_BT” [25]. Nevertheless, there is no theoretical or experimental gain versus QW depth study which could yield a more specific idea of what is required for the (GaIn)As/Ga(AsP) system and which is investigated here. In any case, the closer the emission wavelength is to the band gap of GaAs (~870 nm), the more the well depths is of concern.

Interestingly, a satisfying laser performance is observed with the discussed QW design at 950 nm. A VECSEL, containing ten QWs arranged as resonant periodic gain, yields Watt level output powers as will be demonstrated in the next section. In regard to an emission wavelength of about 920 nm it is assumed that a comparable material gain can be established, if the QW depth, which is essentially limited by the VBO, can be kept at a comparable magnitude. Indeed, the QW depth is reduced if the indium content is further reduced and while the QW width is kept at 8 nm, but this can be compensated if the barriers are modified appropriately.

An approach to enhance the VBO is, thus, to embed the QW in thinner Ga(AsP) barriers but with an increased phosphorus content. In this way, strain compensation and barrier height can be addressed simultaneously. To not impede the capture of charge carriers from the barriers, (AlGa)As separation layers between the individual QWs are used. Based on the bowing parameters from reference [27] and with aluminum and phosphorus contents of $y, z = 5$ % band gaps of 1.504 eV and 1.481 eV are obtained for the $Ga(As_{1-y}P_y)$ and $(Al_zGa_{1-z})As$, respectively. The approach is illustrated on the right-hand side of Fig. 5.1. The amount of compressive strain is increased in the (GaIn)As QW which results in a more pronounced heavy and light hole splitting. On the other hand, there is some significant tensile strain in the Ga(AsP) barriers which effects in a flip of the heavy and light hole splitting. However, the quantum confinement of electrons and heavy holes should be significantly improved in comparison with a design of thick Ga(AsP) barriers and a lower phosphorus concentration, respectively. The difference energy between the emission maxima of QW and barrier states is 136 meV and the VBO is between 41 – 54 meV (cf. Fig. 5.2 (blue) and Tab. 5.1).

Overall, the PL intensity is highest for the first structure, emitting at 1015 nm and with the VBO of larger than 71 meV (cf. Fig. 5.2). A significant drop of the intensity by a factor of greater than ten is obtained for the 950 nm sample with a VBO of >38 meV, respectively. Although the emission wavelength is even lower, the intensity of the 920 nm sample is rather improved in comparison with the 950 nm. This can be attributed to an improved QW depth with a VBO of >41 meV. Regarding the VBO ratio for the (GaIn)As/Ga(AsP) system [99], the VBO should rather amount to 54 meV.

Consequently, the latter design should be well suited for the realization of barrier pumped VECSELs with emission at 920 nm. In particular, a similar approach was already pursued by Kim et al. [32], who have demonstrated a 920 nm emitting VECSEL with output powers in excess of 10 W. Referring to their report, the applied (GaIn)As/Ga(AsP) QW design employs thin barriers with phosphorus concentrations of 10 %.

5.2 VECSEL samples

The discussed QW designs for the emission at 920 nm are now implemented in VECSELs. Three different samples from three different wafers are studied thoroughly (Samples 5.1 – 5.3). Furthermore, one VECSEL sample is available with the above discussed design for 950 nm (Sample 5.4).

All VECSELs 5.1 – 5.4 are based on a RPG with ten QWs of the respective design. In case of samples 5.1 – 5.3, with the QWs embedded into the thin Ga(AsP) layers, $(Al_zGa_{1-z})As$ separation

Table 5.2. Summary of VECSEL samples designed for the emission between 920 – 950 nm. The composition of the gain region is obtained from HR-XRD. The Bragg-mirror and cap layer compositions are design values.

		Sample 5.1	Sample 5.2	Sample 5.3	Sample 5.4
Cap		$(Ga_{0.52}In_{0.48})P$ + $(Al_{0.50}Ga_{0.50})As$	$(Ga_{0.52}In_{0.48})P$	$(Ga_{0.52}In_{0.48})P$ + $(Al_{0.50}Ga_{0.50})As$	$(Ga_{0.52}In_{0.48})P$
RPG	In conc. x	9.0 %	9.1 %	9.0 %	12.3 %
	P conc. y	7.2 %	6.6 %	6.0 %	0.9 %
	Al conc. z	5 %	5 %	5 %	-
	QW width	7.0 nm	8.0 nm	8.0 nm	6.2 nm
DBR		$AlAs/(Al_{0.20}Ga_{0.80})As$			

layers are grown to obtain the λ/2 optical thickness between the individual QWs as indicated in the previous section. A low aluminium content of $z = 5\ \%$ is chosen to adapt the band gap to the Ga(AsP) barriers. At the same time a high pump absorption at 808 nm is maintained while the introduced strain is fairly low and can be neglected. In sample 5.4 the optical layer thickness is directly adjusted by the Ga(AsP) barriers with the low phosphorus concentration of $y = 1\%$. For more clarity, the compositions of the resonant periodic gain regions, obtained from HR-XRD diffraction measurements, are summarized in Tab. 5.2. The overview illustrates that the realized gain regions effectively match the aforementioned designs. Only slight variations in the indium and phosphorus concentrations are observed. Table 5.2 also indicates the design cap layer and distributed Bragg reflector compositions. Please note that the cap layers mark a difference between the samples 5.1 and 5.3 in comparison with samples 5.2 and 5.4. Whereas latter samples exhibit the regular λ/2 (GaIn)P cap layer, the other two samples employ a bilayer of λ\4 $(Ga_{0.52}In_{0.48})P$ and λ\4 $(Al_{0.50}Ga_{0.50})As$. The effect of the different designs will be discussed later in section 5.5. A similarity of all four samples is the ternary DBR which consists of 22 ½ pairs of $(Al_{0.20}Ga_{0.80})As$/AlAs and which is transparent for the pump wavelength, respectively. The layer thicknesses are adjusted to center the stop band at the respective emission wavelength.

A key design parameter should also be the detuning. Its importance was demonstrated in chapters 3 and 4 by means of the reference sample and sample 4.1, both with emission wavelengths above 1 µm. A result from these investigations is that the detuning is not a critical parameter to achieve laser operation in some way, but has a great impact on the laser performance, i.e. on the threshold pump density, slope efficiency and maximum output power. For instance, the reference sample with a detuning of -14 nm exhibits a low threshold intensity (1.0 kW/cm²). In contrast, sample 4.1 still operates at a detuning of -40 nm but with drastically increased threshold intensities (7.3 kW/cm²) and an improved maximum output power. The studies have confirmed the theoretical predictions by Hader et al. [32]. Interestingly, these calculations show, too, that the detuning does not have an impact on the threshold pump intensity, if it is in a range between 10 nm to -5 nm. These findings are also understood in terms of the thermal resistance measurements in section 3.5, which have exposed the gain temperatures in dependence of pump power and heat sink temperature. It was revealed that gain and heat sink temperatures are essentially equal when the laser is operated close to the threshold, i.e. there is no significant heating and, thus, no thermal shift of neither the material gain nor the micro-cavity resonance. Assuming a linewidth (FWHM) of the material gain of ~30 nm [104], there is sufficient overlap of material gain and micro-cavity resonance for the above-mentioned range of detuning at room temperature. However, it is a challenge to transfer these findings to the VECSELs with emission wavelengths between 920 – 950 nm. As discussed, it is expected that the reduced quantum confinement results in a weaker and narrower material gain. In principle, this should in turn make these lasers more sensitive to the detuning. Also, it has not been studied how the thermal roll over might be affected by the shallow QWs. Therefore, it is reasonable to design the samples with a small negative detuning, between 0 nm to -15 nm. Such detuning allows for a slight, pump-absorption induced heating before material gain can built up and while a sufficient overlap between micro-cavity resonance and material gain is maintained. However, it must also be considered that the heating of the structure should be less significant as the quantum defect is significantly reduced for the 920 nm (12 %) and 950 nm (15 %) lasers. Following this strategy, the optical cap, barrier, and Bragg reflector layer thicknesses are designed to place the longitudinal confinement factor maximum at a wavelength of up to 15 nm longer than the PL maximum.

For the following studies, actually multiple samples of each design have been processed by the flip-chip bonding technique as described in section 3.1. The result was that there is basically no

significant variation in the chip quality or the chip reflectance. The chip quality was examined by microscopy of the chips' surfaces. Furthermore, the chips could withstand pump powers of more than 10 kW/cm² which confirms a proper bond between the Bragg reflector and the diamond heat spreader. Moreover, the reflectance can be understood as a fingerprint of a VECSEL, as it contains information about absorption properties and layer thicknesses. It was found that the processed chips of each design had a very similar reflectivity which indicates a good wafer homogeneity and a good reproducibility of the selective wet chemical etching for the removal of the substrate. As a conclusion, the investigated samples in this chapter can be seen as representative and the obtained results can be generalized for each design.

Having introduced the different samples and design strategies, a detailed analysis of the samples will be carried out as the next step. The procedure of the following studies is very similar to what has been presented in chapter 3. In the next section, it is tried to accomplish lasing and study the laser performance.

5.3 Laser studies

Samples 5.1 – 5.4 are mounted one-by-one onto the heat spreader and a regular linear cavity is arranged with a mirror's radius of curvature of -100 mm. A high reflective mirror with a transmissivity of less than 0.1 % is available as well as out-coupling mirrors with 1.5 % and 3 % transmissivity. However, the 1.5 % mirror does only cover wavelengths above 940 nm. The 808 nm pump laser is focused under an angle of 30° onto the sample. For this, a pump optics consisting of two lenses with the focal lengths of 50 mm and 55 mm are used, resulting in a pump spot size of 740 µm × 825 µm (cf. section 3.2). Indeed, this will not enable TEM_{00} operation, but will drastically simplify the alignment of the external cavity and, thus, also facilitate the first observation of laser operation. A proper alignment of the cavity is furthermore ensured with the help of a red laser diode. Laser cavity and laser diode are adjusted to be collinear. The multiple reflections of the laser diode between chip and laser mirror are superimposed with the pump spot. With this procedure, no further adjustments were necessary in case of the VECSELs in chapter 3 and 4, i.e. lasing is observed as soon as an adequate pump level is applied. Moreover, the large pump spot features a low thermal resistance which should enhance the lasers performance. Referring to Fig. 2.10 the thermal resistance should be below 2 K/W.

The investigation is unsuccessful in case of samples 5.1 – 5.3. No laser operation can be observed even though different pump intensities (even beyond 10 kW/cm²) are applied. Also heat sink temperatures between 5°C to 50°C are tested which could compensate for a disadvantageous detuning, since a variation of the temperature effectively increases or reduces the samples detuning.

A contrary observation is made in case of sample 5.4. Lasing is readily observed at room temperature and with the high reflective mirror. Laser operation is also achieved with mirror transmissivities of 1.5 % and 3 %. However, in case of the 3 % mirror, the threshold is only achieved at reduced temperatures. For instance, the threshold intensities are 4.3 kW/cm² at 5°C and 6.0 kW/cm² at 10°C. Furthermore, when laser operation is achieved with the 3 % mirror, bright lines across the VECSEL chip become visible with help of a CCD camera. These lines are perpendicular to the chip's facets which is a clear indication of lateral lasing [105, 106]. Lateral lasing occurs due to the high Fresnel reflectivities of the chip's parallel facets which form a

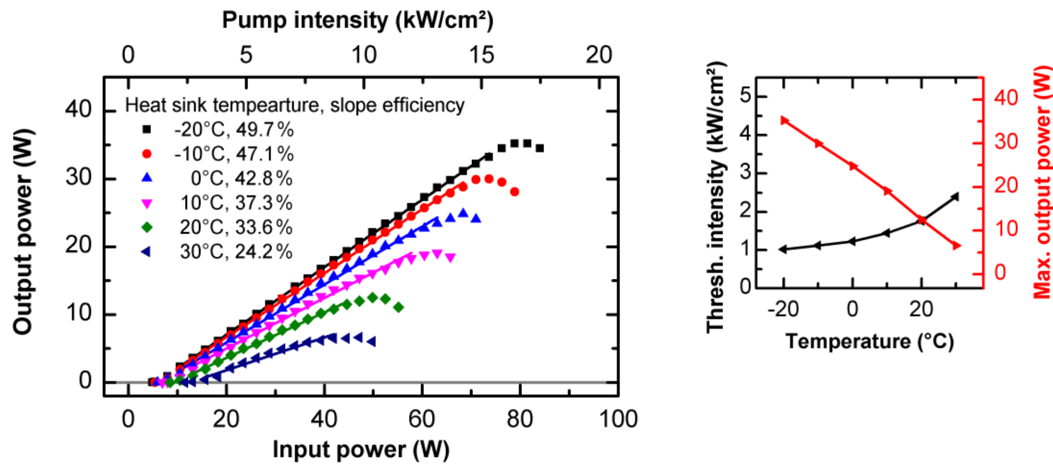

Figure 5.3. Power Curves of sample 5.4 (left) and laser threshold as well as the maximum output power of the device in dependence on the heat sink temperature (right).

resonator. Due to heating at the pumped region, the QW luminescence shifts towards higher wavelengths and the unpumped regions of the chip become transparent which enables the build-up of amplified spontaneous emission and even in-plane lasing. At even higher temperatures, like 15°C, no vertical lasing is accomplished but there is still indication of lateral lasing.

Lateral and vertical lasing are highly competitive processes, and hence, lateral lasing can be suppressed by improving the modal gain and reflectivity in vertical direction. This implies an optimization of the detuning. The above observations indicate that such optimization is effected by a reduction of the heat sink temperature. Moreover, the losses can be reduced by using a mirror with less out-coupling. Accordingly, a decent performance is observed with the 1.5 % mirror. At a heat sink temperature of 20°C an output power of 12.5 W is achieved (cf. Fig. 5.3). The threshold intensity is 1.8 kW/cm² and, thus, comparable to that observed for the reference sample. The power curves are also recorded for other heat sink temperatures (-20°C – 30°C), revealing the temperature dependence of the slope efficiency, threshold and maximum output power. At -20°C a remarkable output power of 35.2 W is achieved. The drastic increase of output power suggests that not only the material gain is improved at lower temperatures, but also the detuning.

To further investigate the sample, the shift rate method is applied to study the emission wavelengths, thermal resistance and gain temperatures (cf. section 3.5). For this, spectra are recorded at intermediate power levels and different heat sink temperatures. The evaluation of the maximum wavelength (defined by an intensity drop of -10 dB) and the corresponding dissipated powers are shown in Fig. 5.4. Moreover, an overview of the results obtained from the regression with Eq. 3.7 is provided in Tab. 5.3. To calculate the gain temperatures at threshold and roll-over, first Eq. 3.7 is taken to calculate the wavelength, then the relation between wavelength and gain temperature (Eq. 3.9) is used. A low threshold temperature of 33°C is found, which is comparable to what has been observed with the reference structure and which is typical for a small detuning. But this time, also the gain temperature of the thermal roll-over is clearly reduced (78°C). However, there was also indication of lateral lasing close to the point of roll-over. Therefore, it is possible that the determined gain temperature of 78°C does not relate to the actual thermal roll-over, but marks the starting of lateral lasing. Indication of lateral lasing was also observed while the power curve at 30°C heat sink temperature was recorded which also was accompanied by temporally varying laser spectra. Thus, these spectra have not been considered for the thermal resistance determination.

Table 5.3. Summary of the quantities obtained for sample 5.4 from the thermal resistance measurement based on the shift-rate method.

	$\partial\lambda/\partial P_D$	$\partial\lambda/\partial T$	λ_0	R_{th}	R_{th}/f	$T_{\text{thr}}^{20°\text{C}}$	T_{ro}
Measured	0.2412 nm/W	0.1548 nm/K	949.1 nm	1.56 K/W	1.59 K/W	33°C	78°C
P_D corr.	0.3489 nm/W	0.1222 nm/K	948.3 nm	2.85 K/W	2.91 K/W	44°C	126°C

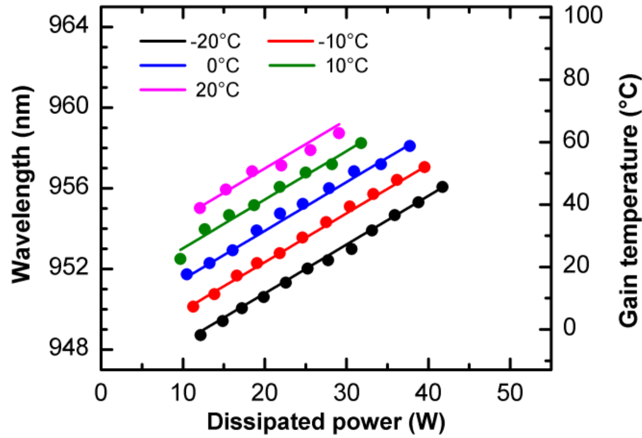

Figure 5.4. Thermal resistance measurement (shift-rate method) of sample 5.4. Symbols depict the measurement data which is obtained by evaluation of the 10 dB drop in the spectra. Lines depict the solution of Eq. 3.7. The right axis shows respective gain temperatures which are calculated on the basis of Eq. 3.9.

The thermal resistance is also determined considering potential intra-cavity losses, i.e. Eq. 3.11 and a scattering loss of 0.57 % are included. A summary of the complete results is also given in Tab. 5.3. In comparison to the reference sample, where a 3 % out-coupling mirror was used, the possible error of the thermal resistance measurement is significantly larger. Consequently, also the threshold and roll-over temperatures are clearly higher (44°C, 126°C). An important result is that the increase of the gain temperature at threshold is still rather low. This is in agreement with the low threshold intensity which is in the same order of magnitude as for the reference sample. According to Fig. 2.10, the corrected resistance (2.91 K/W) seems to overestimate the thermal resistance, whereas the uncorrected value (1.59 K/W) is rather an underestimation. These results enclose the simulation pretty well though.

Concluding, sample 5.4 shows a decent performance. Output powers in excess of 10 W are achieved at room temperature, the laser threshold is fairly low and the thermal resistance measurement documents a proper heat sinking of the sample. The presence of lateral lasing further seems to limit the performance of the device, which may imply that even higher output powers are possible, if it is suppressed. A remarkable result emerges from the comparison of samples 5.1 – 5.4, which all should exhibit a comparable QW depth and also have a similar chip design. From this perspective, it is surprising that only sample 5.4 shows a proper functionality. At this point it is not clear, whether the malfunction of samples 5.1 – 5.3 arises from the QW design or from other issues, such as a disadvantageous detuning.

5.4 Detuning studies

In order to obtain a complete picture of the samples and isolate the issues which cause the unexpected observation, the reflectance and edge PL studies are carried out like in section 3.3. A preview of the following discussion can be obtained by a first glance at Figs. 5.6 and 5.7 (pp. 70, 71), which exhibit a full set of reflectance and PL measurements. These measurements will be summarized and discussed in a step-by-step comparison with the help of Figs. 5.5 and 5.8.

The temperature dependent reflectance measurements are shown in Fig. 5.5 a, a') and Fig. 5.6 a, a'). An absorption dip within the stop band is clearly visible for all samples. Although the measurements look similar, important differences between the samples can be extracted. For the following discussion, a summary of the measurements is provided by Fig. 5.5 where the relative absorption within the stop band is plotted against the heat sink temperature. The graph also contains the respective absorption curve of the reference sample.

In case of *sample 5.1* the absorption is between 60 % and 70 % throughout the hole temperature range. On one hand, this is a clear indication for a positive detuning, because the confinement factor must be placed at the short-wavelength side of the PL peak wavelength. On the other hand, the longitudinal confinement factor should almost achieve the ideal maximum of 4, because of the high absorption, which is, considering the magnitude, also comparable to the reference structure.

The characteristic absorption curve of *sample 5.2* is comparable to that observed for the reference sample. However, the detuning must be significantly smaller than -14 nm (cf. Tab. 3.2), because the absorption maximum is achieved at lower temperatures (~50°C instead of ~100°C). Moreover, it is observed that the slope of the absorption dip is decreased at the long-wavelength side and for elevated temperatures. This also indicates that the QW absorption passes the confinement factor due to its higher shift rate.

Respective observations with *sample 5.3* are very similar to sample 5.2, but the detuning must be even smaller. The absorption maximum is achieved just above room temperature at 30°C and consequently

Last, *sample 5.4* exhibits a feature which is a bit different from the previous samples. Indeed, the characteristic absorption curve is very similar to what is found for samples 5.2 and 5.3, but the

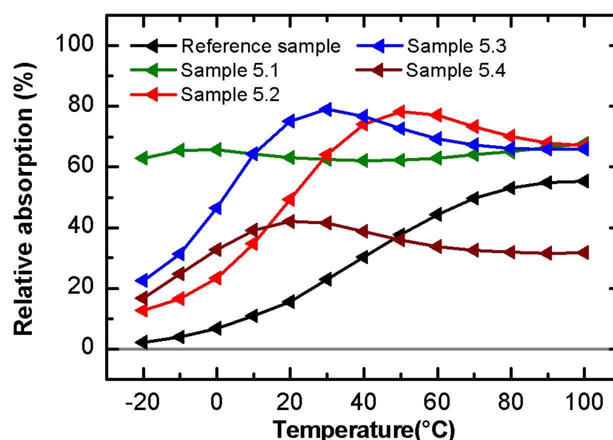

Figure 5.5. Summary of the temperature dependent reflectance measurements. The percentage depth of the absorption is plotted versus the heat sink temperature. Symbols depict the measured data. Lines serve as a guide to the eye.

magnitude of the relative absorption is significantly lower. An obvious explanation may be a reduced confinement factor due to an imperfect alignment of either the micro-cavity thickness, or an uneven distribution of the barrier layer thicknesses. Besides, the sample should exhibit a vanishing detuning, because the absorption maximum is observed just at room temperature. Consequently, even a bend is observed at the long-wavelength side of the absorption dip.

An interim conclusion from the temperature dependent reflectance measurements is that sample 5.1 must clearly exhibit a “wrong” positive detuning. Pump induced heating of the gain region results in a further separation of micro-cavity resonance and gain peak, which is a possible explanation for the malfunction. In contrast, samples 5.2 – 5.4 should have a small, slightly negative detuning. Laser operation of sample 5.4 demonstrates that the detuning should be adequate. Hence, the malfunction of samples 5.2 – 5.3 is still not understood.

Another observation is made by the comparison of the reference sample with samples 5.2 – 5.4. In case of the reference sample, the change of relative absorption is only about 10 % in the temperature range between 60°C and 100°C. Considering comparable temperature range of 40°C close to the maximum absorption, the change is 45 %, 50 %, and 25 % for samples 5.2 – 5.5. In the temperature dependent measurements, the longitudinal confinement factor essentially samples the long-wavelength tail of the material absorption. Hence, the observed shape of the relative absorption is an image of the QW absorption which is closely related to the PL spectra. The power and temperature dependent edge PL spectra are represented in Figs. 5.6 b, b’, c, c’) and Figs. 5.7 b, b’, c, c’). The extraction of the room temperature, low excitation density linewidth (FWHM) yields values of 15 nm and 18 nm for samples 5.2 and 5.3, 20 nm for sample 5.4 as well as 39 nm for the reference sample. These numbers correlate well to the slopes in the characteristic absorption curves (cf. Fig. 5.5). The width of absorption and PL spectra is correlated to the material quality in terms of layer widths, composition fluctuations and defects. Fluctuations of these parameters lead to an inhomogeneous broadening of the PL [107]. Another influence is the carrier and phonon-scattering, which leads to an homogeneous broadening (for instance with an increase of temperature) [107]. The measurements indicate a broadening of the spectra with an increase of the indium content in the QWs. Therefore, the observed tendency rather implies a superior material quality of samples 5.2 – 5.3 and which is also in agreement with HR-XRD measurement, from which the QW compositions have been obtained. Still, these findings also indicate an increased sensitivity of the modal absorption in relation to temperature and the impact of the detuning should therefore be more pronounced for the 920 nm samples.

The power and temperature dependent PL measurements are summarized in Fig. 5.8. Figure 5.8 a) illustrates the evaluation of the peak wavelengths in dependence on the excitation power. The low density room temperature design wavelengths of 920 nm and 950 nm have been matched conceding deviations of less than 10 nm. It is conspicuous that the edge PL of samples 5.1 – 5.3 could only be recorded from 10 mW on, whereas spectra could be resolved already at 1 mW of excitation power in case of the reference sample and the sample at 950 nm. This is an indication of a weaker PL signal for the 920 nm structures. The evaluation of the peak wavelengths from the temperature series reveals similar shift rates (0.33 ± 0.01 nm/K) in comparison with the reference sample. However, a great difference is observed in the drop of the intensity. From -20°C to 100°C the drop is only 33 % for the reference sample, but 63 % for sample 5.4 and even ~95 % for samples 5.1 – 5.3. These findings are very different from the above discussion in section 5.1 relating to the QW depth, since samples 5.1 – 5.4 should not be different. To exclude that the strong intensity drop is an artefact of the edge PL measurements, similar samples but without Bragg-mirror could be compared in a temperature dependent surface PL measurement in a future study.

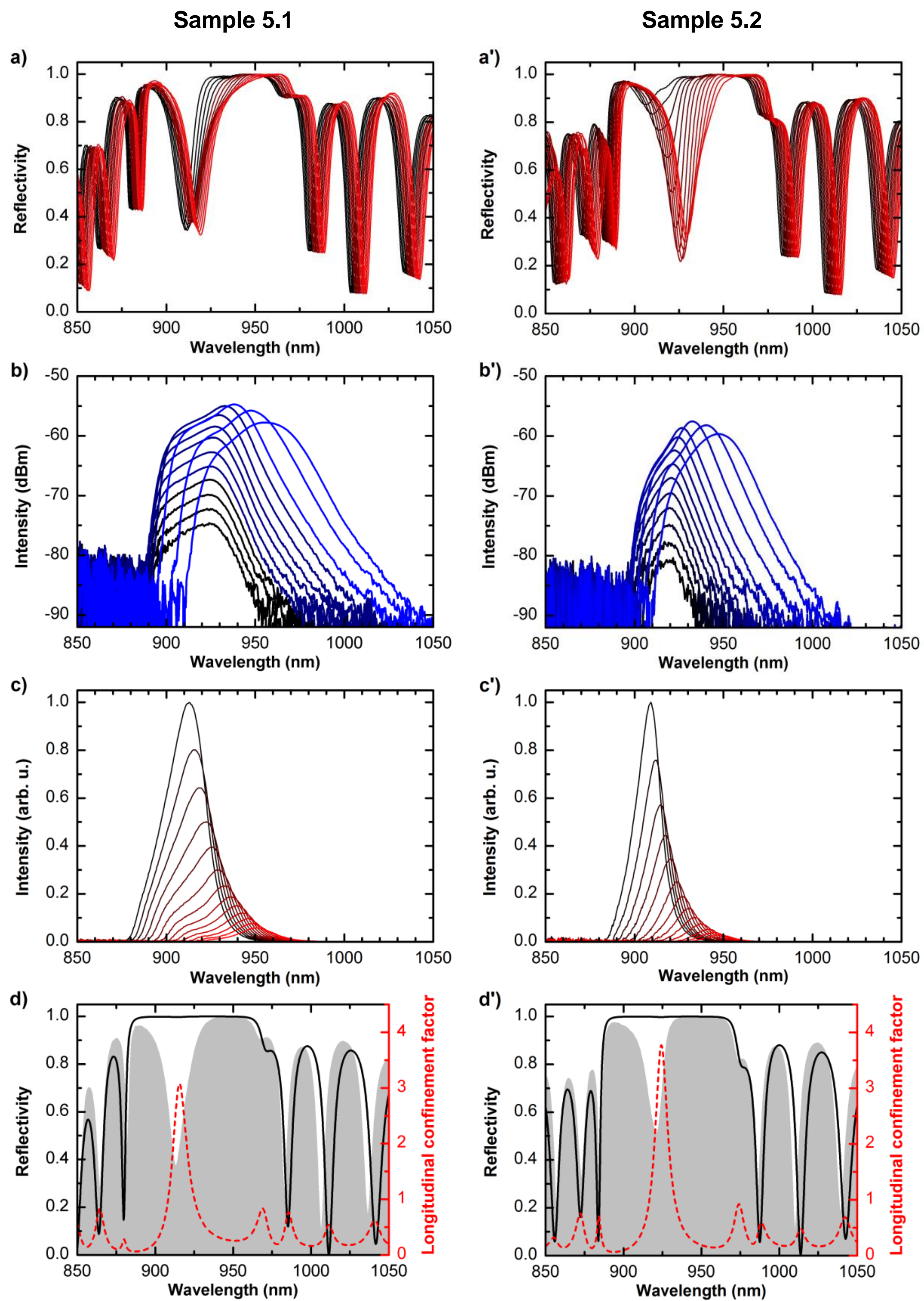

Figure 5.6. Overview on the studies of **samples 5.1 and 5.2**. The TDR measurements are shown in a, a'), the power and temperature dependent edge PL measurements in b, b') as well as c, c') and the transfer-matrix calculations of the reflectivity and confinement factor in d), and d').

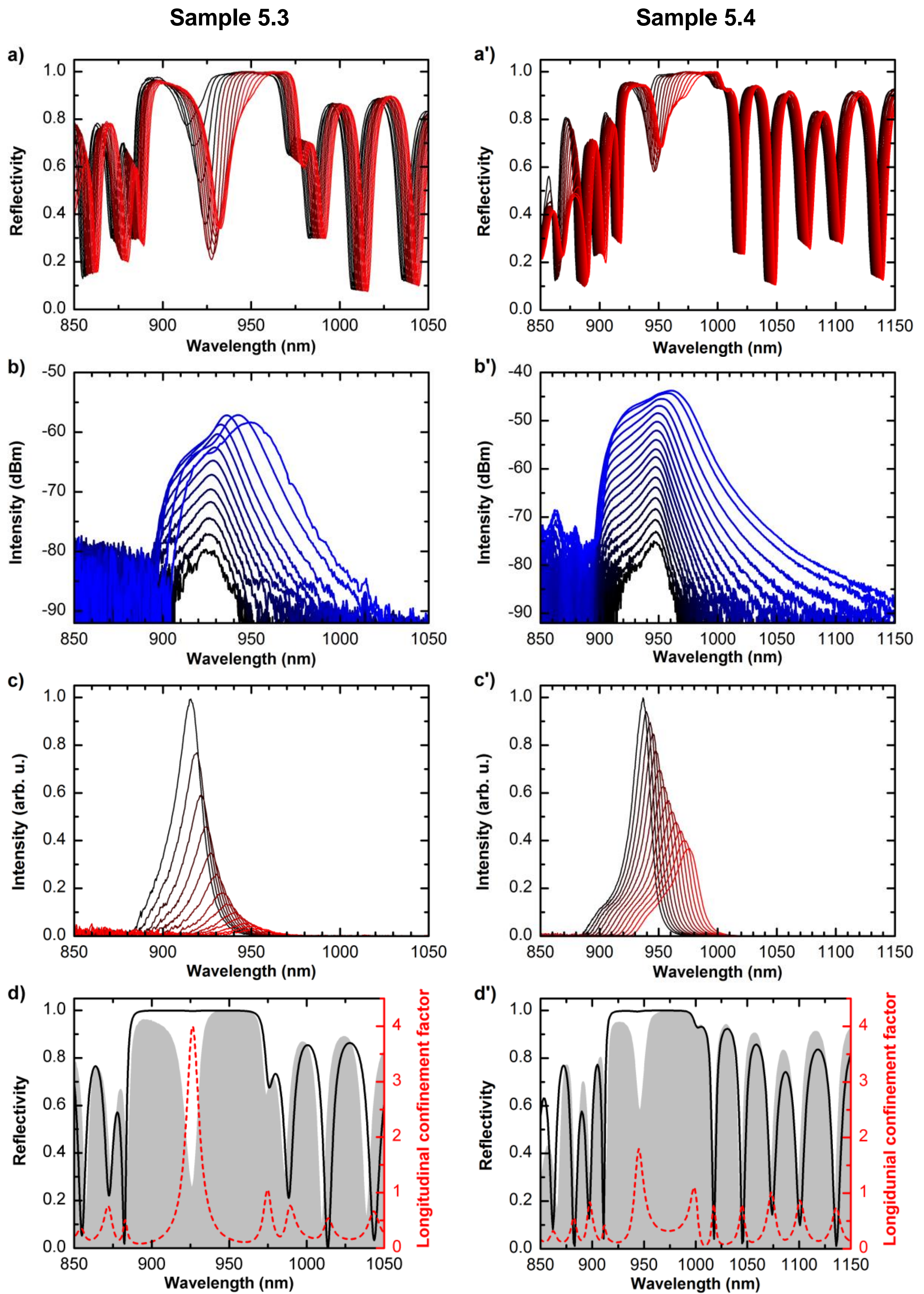

Figure 5.7. Overview on the studies of **samples 5.3 and 5.4**. The TDR measurements are shown in a, a'), the power and temperature dependent edge PL measurements in b, b') as well as c, c') and the transfer-matrix calculations of the reflectivity and confinement factor in d), and d').

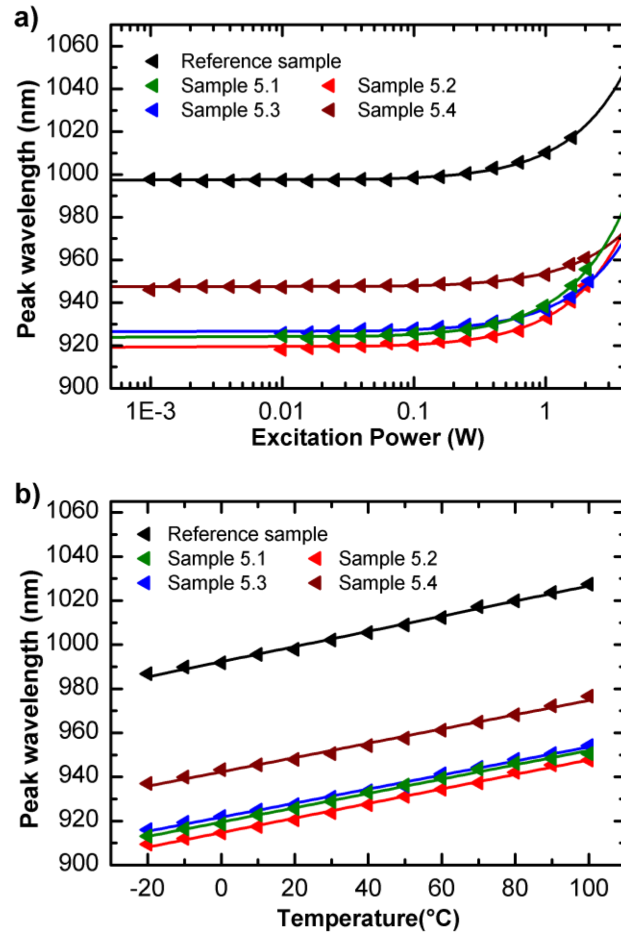

Figure 5.8. Peak wavelength of the edge PL spectra in dependence on excitation power (a), and holder temperature (b). Symbols depict the measured data. Lines show the linear regressions of the measurement data.

As last study of this section, the room temperature reflectivity curves are fitted by transfer-matrix calculations (cf. Figs. 5.6 d, d') and Figs. 5.7 d, d')). A good agreement is found with deviations between the designed and simulated DBR layer thicknesses of less than 1 %. In contrast, there is some discrepancy in the cap layer thicknesses. The relative errors between designed and calculated cap layer thickness are 16.3 %, 10.3 %, 4.1 % and, 1.0 % with increasing sample number. The calculated cap layer thickness was thinner than the design thicknesses. Hence, the error might be an effect of the selective wet chemical etching. However, as indicated in section 5.2, not only one sample per design was processed. The similarity of the room temperature reflectance spectra among different samples (for each design) indicates that the cap layer thickness must be very similar among the different samples of each design. This implies a systematic error either in the growth of the cap layer or the wet chemical etching. Still, due to the good agreement between measured and calculated reflectance, a reliable result can be noted for the longitudinal confinement factor, which is also plotted in Figs. 5.6 d, d') and Figs. 5.7 d, d'). The resulting peak wavelengths of the micro-cavity resonance enable the precise indication of the VECSELs' detunings (cf. Tab. 5.4). The obtained values agree well with the interpretation of the temperature dependent reflection measurements: Sample 5.1 exhibits a "wrong", positive detuning (9 nm), whereas samples 5.2 and 5.3 have a slight negative detuning (-5 nm, -1 nm) and sample 5.4 a slight positive detuning (2 nm). It is also verified that sample 5.4 exhibits a weak micro-cavity resonance with an amplitude of only 2 instead of the ideal value of 4.

Table 5.4. Summary of the detuning determination of samples 5.1 to 5.4 and the reference sample obtained from power and temperature dependent edge photoluminescence measurements as well as the calculation of the longitudinal confinement factor.

	Peak wavelength (nm)	LCF peak (nm)	Detuning (nm)	Absolute error of LCF (nm)	Max. abs. temperature (°C)
Ref. sample	997	1011	-14	1	74
Sample 5.1	924	916	+ 8	9	-12
Sample 5.2	919	924	-5	5	40
Sample 5.3	926	927	-1	3	24
Sample 5.4	947	945	+ 2	1	12

In order to illustrate the influence of the thinner cap layer, transfer-matrix calculations are also carried out assuming the design cap thicknesses. The resulting micro-cavity resonances are compared with the results of the fit. The result is summarized in Tab. 5.4 which contains the absolute error of the peak wavelengths due to the change in the cap layer thickness. Please note that the sign of the error relates to the confinement factor. Referring to the definition of the detuning (cf. Eq. 2.12) the impact on the detuning has the different sign, i.e. detunings of -1 nm, 0 nm, + 2 nm, and + 1 nm had been achieved, if the cap layer thicknesses of the realized samples were identical to the design.

For an approximation of the temperature at which micro-cavity resonance and QW gain have an optimized overlap the measured shift rates of the reflectance and the PL are taken into account. The obtained values are depicted in Tab. 5.4. Referring to the low increase of the gain temperature at threshold in the reference sample, samples 5.2 and 5.3 seem to have very promising detunings for laser operation, whereas sample 5.1 needs to be cooled drastically. Sample 5.4 exhibits a very similar non-ideal detuning. This explains the observed, drastic improvement of the performance for decreased temperatures. However, the detuning does not explain, why sample 5.4 provides decent laser operation, while samples 5.2 and 5.3 do not work at all. It rather indicates that there is a great discrepancy of the material gain between these samples.

5.5 Gain measurements

Strictly speaking, the laser studies in section 5.3 are only *indicating* that the laser threshold cannot be achieved in case of the 920 nm. Although the external cavity was aligned carefully and the operation conditions (heat sink temperature, pump intensity) were varied in a wide range, there is still a possibility that no lasing is observed due to a misalignment or due to corrupt external laser mirrors. However, an incontrovertible *proof* of the malfunction is obtained by a direct measurement of the modal gain. Against this background, samples 5.1 – 5.3 should at most reach transparency, i.e. the absorption dip within the stop band may vanish, but the reflectivity cannot achieve values greater than unity. Thus, in order to further investigate the malfunction of the 920 nm VECSELs, gain measurements are performed.

For these investigations, samples 5.2 and 5.3 are studied with the gain measurement setup presented in section 3.4. As summarized in Tab. 5.2, the difference between samples 5.2 and 5.3 is their cap layer design. Whereas a single layer of λ\2 $(Ga_{0.52}In_{0.48})P$ is employed in sample 5.2, a bilayer of λ\4 $(Ga_{0.52}In_{0.48})P$ and λ\4 $(Al_{0.50}Ga_{0.50})As$ is applied in sample 5.3. Thereby, both samples exhibit the same air-chip interface, but have a different band alignment between cap and resonant periodic gain. For the (AlGa)As/GaAs heterojunction a VBO of 0.35 is reported as the average literature

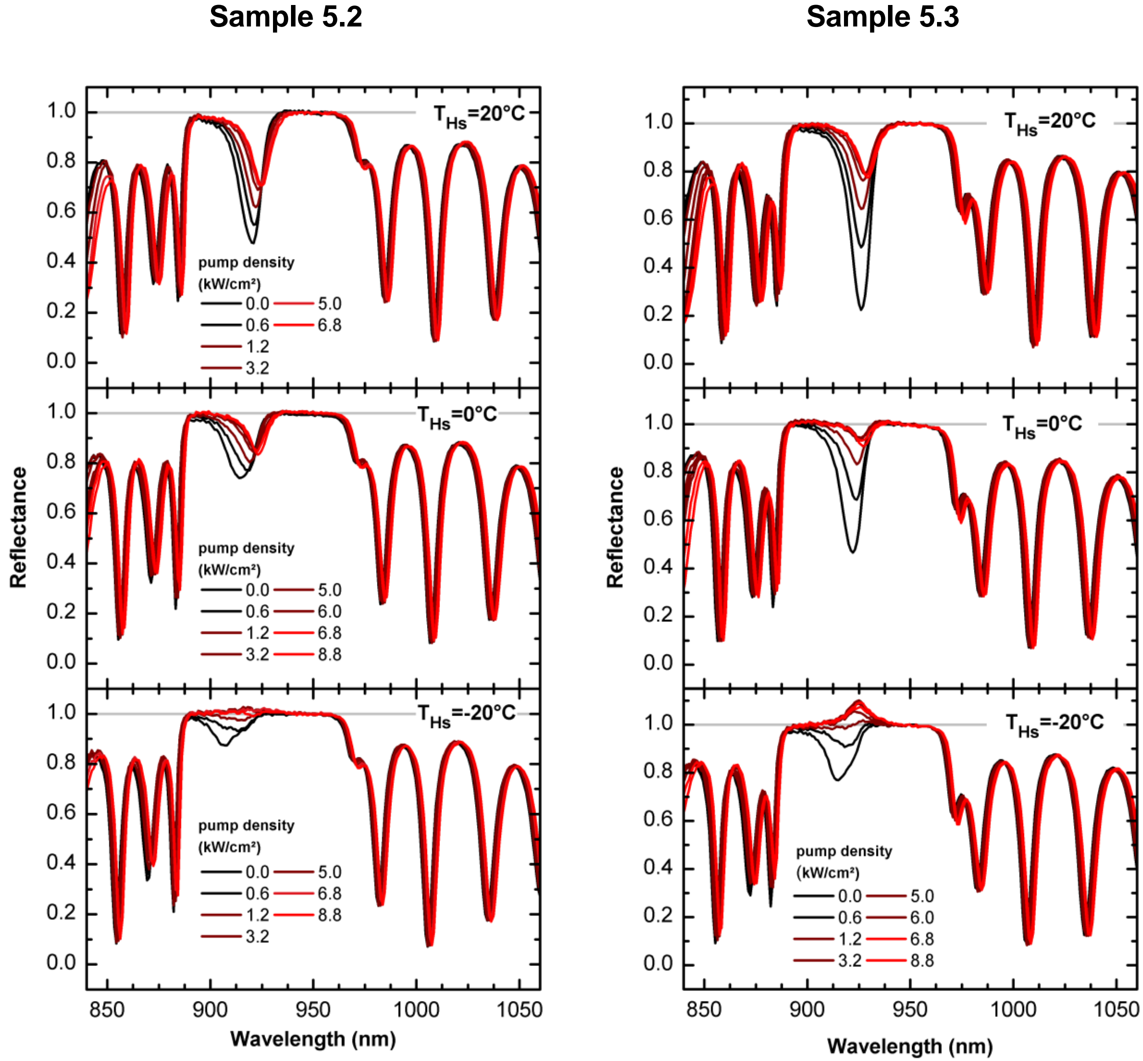

Figure 5.9. Measurements on samples 5.2 and 5.3 of the reflectivity as a function of pump intensity for heat sink temperatures of 20°C, 0°C and -20°C.

value [27]. The room temperature band gaps of the (AlGa)As cap layer and the separation layer, also accounting for an aluminium content of 5 % aluminium in the separation layers, are 1.998 eV and 1.484 eV (calculated with use of the bowing parameters from [27]), which yields a difference of 514 meV. This results in a VBO of 180 meV and a CBO of 334 meV, respectively. Hence, it is not possible for carriers within the gain region to diffuse to the air-cap interface and recombine with surface states. In contrary, a negligible CBO was found to take place in a the $(Ga_{0.50}In_{0.50})P/(Al_zGa_{1-z})As$ heterojunction with low aluminium content. In particular, the CBO is reported to be zero at an aluminium content of z = 11 % [108]. Therefore, it should be possible for electrons to recombine with surface states at the air-cap interface. However, it is noteworthy that such non-radiative carrier loss due to recombination outside the gain region is prohibited concerning the distributed Bragg reflector, which comprises AlAs layers with sufficient valence and conduction band offsets.

It is further to mention that samples 5.1 and 5.3 are essentially equal, but only have a different detuning as demonstrated in the preceding section and summarized in Tab. 5.3. Because the detuning of sample 5.3 is expected to be more appropriate for laser operation, this sample is chosen for the gain investigation, well-knowing that the results will also apply to sample 5.1.

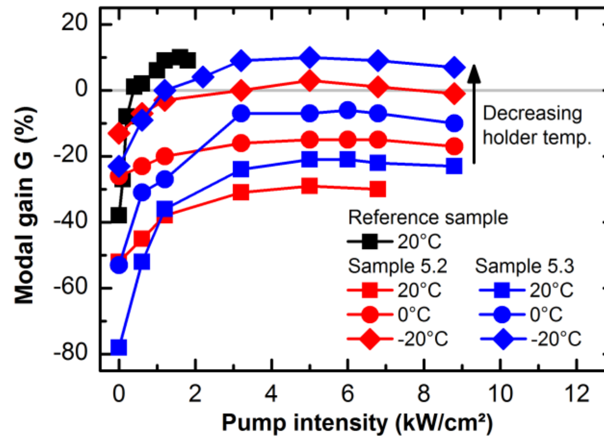

Figure 5.10. Modal gain versus pump intensity for samples 5.2, 5.3 and the reference sample. Symbols depict the measured data. Lines serve as a guide to the eye.

The gain measurements are conducted with heat sink temperatures of 20°C, 0°C, and -20°C, as well as pump intensities of up to ~8.8 kW/cm². The complete set of measurements is shown in Fig. 5.9. The first spectrum of each series is recorded at zero pump intensity and hence is a reproduction of the corresponding reflection measurements in the previous section. At a first glance, it is observed that there is a certain bleaching of the absorption dip within the stop band at 20°C and 0°C holder temperature. However, not even transparency is achieved which is the final proof that no lasing can be achieved at the tested conditions in section 5.2. The measurements show also that lasing must be achieved if the heat sink temperature is further decreased. At a temperature of -20°C a gain peak is observed for sample 5.3. Sample 5.2 exhibits a reflectivity slightly above 1, too. This, however, might not be enough for lasing.

For a more detailed discussion, the extremum within the stop band is evaluated and plotted as modal gain *G* (cf. Eq. 3.4) versus the pump intensity. For comparison, also the gain measurement on the reference sample is added to this graph (cf. Fig. 5.10). This plot shows more clearly that there is a non-saturable absorption of about 30 % and 22 % at 20°C, or 15 % and 7 % at 0°C holder temperature for samples 5.2 and 5.3, respectively. A further increase of the pump intensity does not further reduce the absorption within the stop band. It also illustrates the improvements due to a decrease of the temperature. At -20°C, the saturation finally takes place at positive *G* values. The improvements can be related to both, an effective increase of the negative detuning, and an enhanced material gain due to a reduction of non-radiative losses. Concerning the temperature shift rates of micro-cavity resonance and PL, an effective detuning of -15 nm is obtained for sample 5.2 and -11 nm for sample 5.3, respectively. The comparison furthermore reveals that the absorption is bleached much faster in case of sample 5.3. However, this is still not comparable with the reference sample, which additionally exhibits significant gain at room temperature.

Overall, these measurements show that sample 5.3 is superior in comparison with sample 5.2. Whereas sample 5.2 seems to slightly surpass transparency, sample 5.3 clearly exhibits gain at -20°C. This cannot be explained by the slight difference in detuning, which is even superior in case of sample 5.2. The reason must be rather located at the different cap layer design and an excessive loss of electrons at the $(Ga_{0.52}In_{0.48})P$ cap layer. Consequently, the results demonstrate the importance of the confinement of the charge carriers not just at the QWs, but also at the whole resonant periodic gain region. A first important conclusion is hence that the additional $(Al_{0.50}Ga_{0.50})As$ layer is necessary as a barrier for the electrons.

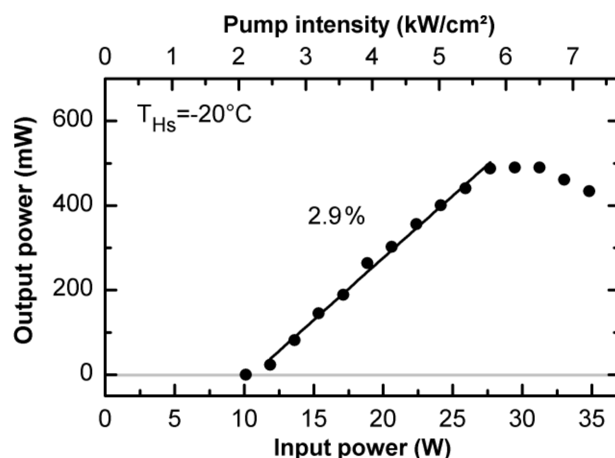

Figure 5.11. Power curve of sample 5.3 at a heat sink temperature of -20°C and with the high reflective mirror (R > 99.9).

The drastic difference between the reference sample and sample 5.3 must be related to the different detuning or the different material absorption of the QWs. A result of the thermal resistance measurements in sections 3.5 and 5.3 was that the VECSEL does not heat up significantly at threshold though. Hence, it must be concluded that the slow saturation of the QW absorption in sample 5.3 must be mainly related to the QW design. Indeed, it might be possible to account for the slow bleaching by employing a larger negative detuning, but it seems more reasonable to understand and rectify the mechanism which leads to the low QW gain. A hint of such optimization is obtained by the comparison between sample 5.2 and 5.3 which demonstrates the importance of the charge carriers from the barriers and separation layers, as they contribute significantly to the bleaching of the QW absorption and at a certain level also to the gain. This suggests that there is another mechanism which prevents charge carriers from being captured by the QWs. A comparison of the different designs further sheds light onto the 10 nm thick Ga(AsP) barrier layers in samples 5.1 – 5.3 which may impede the carrier capture. However, this is not understood in terms of the above discussed literature values for the valence and conduction band offsets which indicate smooth heterojunctions.

As a side note of this chapter, samples 5.2 and 5.3 are again investigated in the laser setup, since the demonstration of gain at a heat sink temperature of -20°C motivates to repeat the investigation from section 5.3 which was only performed above 0°C. Lasing is still not achieved with sample 5.2. In case of sample 5.3, lasing is achieved with the high reflective mirror (R > 99.9 %). The power curve, shown in Fig. 5.11, reveals a slope efficiency of only 2.9 % and a maximum output power of 500 mW. The poor performance can be attributed to the weak out-coupling. However, lasing was not achieved with the 3 % mirror. The emission wavelength is between 935 nm (threshold) and 941 nm (roll-over).

5.6 Summary and outlook

A thorough study of laser samples for the emission between 920 nm and 950 nm was provided. Quantum well depth and detuning were discussed as key parameters for their realization. An important result concerning the 950 nm VECSEL is that the structure yields output powers beyond 10 W and at room temperature, although it is not optimized. The micro-cavity resonance only reaches a factor of 2, rather than the theoretical maximum of 4. Consequently, the modal gain can

be doubled just by correcting the QW separation. An improved resonance should also suppress the observed lateral lasing. Furthermore, the slight positive detuning results in an early separation between micro-cavity resonance and material gain. In order to optimize the sample for higher output powers, it would be interesting to significantly increase the detuning.

The surprising result that only the 950 nm yields proper laser performance, but not the 920 nm devices, was discussed in detail by a step-by-step comparison of reflectance, edge PL as well as gain measurements. In this way, it was revealed that one sample exhibits a significant positive detuning which can explain its malfunction. Another sample, which exhibits a vanishing CBO between cap layer and resonant periodic gain, shows a slow bleaching of the absorption which can be attributed to an excessive carrier loss due to recombination at surface states. However, there was one sample left, designed for the emission at 920 nm, where no such issue was identified. The cap layer is designed to act as a barrier for the charge carriers within the barrier. Also the detuning is rather superior in comparison with the VECSEL at 950 nm. Still, the device showed only lasing at a heat sink temperature of -20°C. Overall, these findings isolate the cause of the malfunction to the initially discussed QW design.

For further investigations, the QW design should be varied. For instance, the Ga(AsP) strain compensating layers can also be placed at the center of the (AlGa)As separation layers. In this way, the respective heterojunction between the (AlGa)As and the Ga(AsP) is removed from the vicinity of the QW while the required VBO and CBO at the QW should be maintained. A more detailed comparison of the designs, also including the designs at 950 nm and 1010 nm, could be performed by means of temperature dependent PL measurements. The corresponding Arrhenius plots could yield more valuable information about potential loss mechanisms and the suitability of the designs as gain media.

To account for a low material gain one could further take advantage of the low strain due to the low indium contents. For the investigated 1 µm emitting devices, the number of ten QWs seems to be a reasonable trade-off between different design parameters. Initially, it was calculated that a number of 16 QWs, equally distributed in a resonant periodic gain as in the discussed designs, is still feasible and results in a superior material gain. The simulated maximum output power is about 50 % higher in comparison to a tenfold QW structure [32]. Still, the highest output powers have been demonstrated with the design presented in chapter 4 and in references [20, 63]. This can be explained by the thinner gain region which also maintains a low thermal resistance and a superior material quality. Referring to the low indium contents of 8 % of the 920 nm QWs in comparison with the 20 % in 1 µm structures, it seems reasonable to increase the number of QWs. To maintain a thin gain region, two QWs could be placed at each anti-node of the standing light field. Such design was already successfully realized in a 920 nm VECSEL [15], even with a triple QW per anti-node, and in different VECSELs with emission around 1 µm [34, 55]. Indeed, this will somewhat decrease the amplitude of the confinement factor, but will significantly increase the material gain.

In order to definitely exclude that the detuning is the mainly impeding laser operation of the 920 nm samples, a larger detuning should be realized in future samples. A favorable detuning is in particular -20 nm. If such amount of negative detuning is too large, it can be systematically reduced by the arrangement of a V-cavity with the desired angle (cf. chapter 4). For instance, the micro-cavity resonance can be tuned from 930 nm to 910 nm at an angle of 45° (cf. Fig. 4.1).

6. Properties of type-II VECSELs

The previous chapter was dedicated to the development of VECSELs with emission wavelengths between 920 – 950 nm. This wavelength regime represents one border of accessible wavelength with (GaIn)As/GaAs based 808 nm pumped VECSELs. It was discussed that while the thermal resistance as well as the low quantum defect are advantageous, the shallow QWs constitute a bottleneck and only provide inferior gain.

This chapter is dedicated to the other side of the accessible wavelength with (GaIn)As/GaAs based VECSELs. In comparison to the previous chapter, the development of VECSELs at an emission wavelength of 1.2 µm and beyond faces contrary challenges. For instance, the QW depth is not of concern, but the quantum defect is already 33 % at 1.2 µm with 808 nm pump wavelength. Thus, a fraction of 33 % of the pump intensity is mainly converted into heat, which intensifies non-radiative losses and impairs the laser efficiency. In comparison, the quantum defect is only 20 % at 1010 nm and 12 % at 920 nm emission wavelength (cf. chapters 3 and 5). The emission at higher wavelengths further requires to adapt the layer thicknesses of the RPG regions as well as the Bragg-reflector which results in a higher thermal resistance (cf. section 2.3). Overall, the slope efficiencies are decreased and the thermal roll-over is achieved at lower pump intensities which reduces the achievable maximum output power. An even more significant challenge is the growth of highly strained QWs for the emission beyond 1.2 µm. The strain sets stringent limitations to the growth of high quality (GaIn)As/GaAs QWs, as it is required to exceed indium contents of 30 %. To a certain degree, the growth of highly strained QWs can be accomplished by a careful investigation of the growth parameters. However, there is a transition from the growth of uniform layers to a dot-like growth mode which rules out the growth of QWs [109].

Still, many applications have a demand for lasers in the infrared regime beyond 1.2 µm. Prominent examples are telecommunication and optical data transfer where the wavelength of light sources has to be adapted to the available propagation media [110, 111]. For instance, a minimum absorption in silica-based optical fibers exists around 1.3 µm, which coincides with the dispersion minimum, another minimum is located at 1.5 µm. Other examples are frequency doubling for red emitters in digital projectors or medical applications [13]. In the latter case, eye-safe emitters with wavelengths beyond 1.3 µm are desired where the corneal absorption can provide a natural protection of the retina [112].

To provide laser sources for these applications, different approaches have been followed in the past. With respect to GaAs-based VECSELs, wavelengths of up to 1180 nm are achieved with the (GaIn)As/Ga(AsP) QW design as discussed in chapters 3 – 5. A remarkable output power of 50 W was achieved by Kantola et al. [19]. Still, no wavelength beyond 1.2 µm was reported with (GaIn)As/GaAs QWs, which illustrates the abrupt limitation due to the growth restrictions. Remarkable results have also been achieved with quantum dot VECSELs. At 1180 nm an output power of 7.2 W was achieved [38]. The use of quantum dots is also a promising strategy to bypass the strain limitation on GaAs substrate and enables wavelengths beyond 1.2 µm. At 1.25 µm an output power in excess of 3 W is achieved [113]. Another approach to bypass the strain limitation is based on quaternary (GaIn)(NAs) QWs. Due to the conduction band anti-crossing in this dilute nitride material system, the band gap can be drastically decreased while strain is maintained at acceptable levels. With this approach even the most popular telecom-wavelength at 1550 nm is reached with an output power of 80 mW [114].

Better results, however, are achieved with wafer-fused structures. Up to 8.5 W at 1.27 µm are achieved by Keller et al., with the use of (AlGaIn)As QWs on InP substrate [115]. The RPG is wafer fused with a GaAs/AlAs DBR. With a similar approach even 1 W of output power is achieved at 1.56 µm in single-frequency operation by Rantamäki et al. [116]. With an RPG on GaSb substrate, which is wafer fused with an GaAs/AlAs DBR 1.1 W was achieved at 2.05 µm, also in single-frequency operation [36].

An approach which has not been realized for GaAs-based VECSELs so far, is provided by a type-II QW design. To decrease the inherent Auger losses in mid-infrared lasers, type-II QW structures are investigated since the 90's [117–120]. In a type-II QW, electrons and holes are spatially separated which enables the combination of materials with large band gaps although their radiative recombination, which can be understood as spatially indirect, exhibits a low transition energy in comparison to the type-I transitions. Since the investigation of type-II QWs as laser gain media, remarkable results have been reported. Lasers have been demonstrated on the GaSb [121, 122], InP [35, 123], and also GaAs [124, 125] material systems. The emission wavelengths of the cited devices range from 1.2 µm [125] to 4.5 µm [122]. Nevertheless, research on type-II QW gain media still forms a niche in comparison with the well-explored fields of type-I QWs or quantum dots.

In this chapter, the feasibility of VECSELs with type-II QW gain media is studied in detail. The functionality and design of type-II "W"-QWs is presented in section 6.1. Prior to the realization of the first type-II VECSEL, test samples are characterized by means of power and temperature dependent PL measurements in section 6.2. The experimental PL spectra are compared with a microscopic quantum theory. On the basis of the good theory–experiment agreement, gain can be predicted for the studied design. Therefore, the presented design is promising for the application in a VECSEL and the design of a prototype is discussed in section 6.3. VECSELs are realized by MOVPE and with the flip-chip bonding process as described in section 3.1. Three samples are manufactured and studied by means of the procedure from section 3.3, i.e. the edge PL and reflectance measurements are carried out and the LCF is calculated to obtain a full characterization including the detuning (section 6.4). In section 6.5, laser operation of all three devices is demonstrated and their performance is compared. One of the samples is used to investigate the power and temperature dependent wavelength shift. It is demonstrated that the thermal resistance can be determined by the shift rate method, which gives access to the gain temperatures. Also the V-cavity detuning investigation, as carried out in chapter 4, is conducted with a type-II VECSEL. The impact of the detuning is exposed and a range for an optimized detuning can be indicated. Finally, the results are summarized in section 6.6.

6.1 Type-II quantum well design

A pioneering work with respect to type-II QWs on GaAs was presented by Peter et al. [120]. In their report, a bilayer QW (BQW) consisting of $Ga(As_{1-x}Sb_x)/(Ga_{1-y}In_y)As/GaAs$ is presented. The antimony and indium contents are x = 23 % and y = 24 %. The layer thicknesses are 3 nm and 5 nm, respectively. A scheme of the band alignment is shown in Fig. 6.1 (left). It is illustrated that the antimony mainly effects the VBO, whereas the CBO is slightly positive. This is also confirmed by Gies et al., who observe a slightly positive CBO of 5.5 % [126]. Thus, the VBO is altered stronger in comparison with the (GaIn)As layer (cf. chapter 5). Consequently, the Ga(AsSb) layer serves as

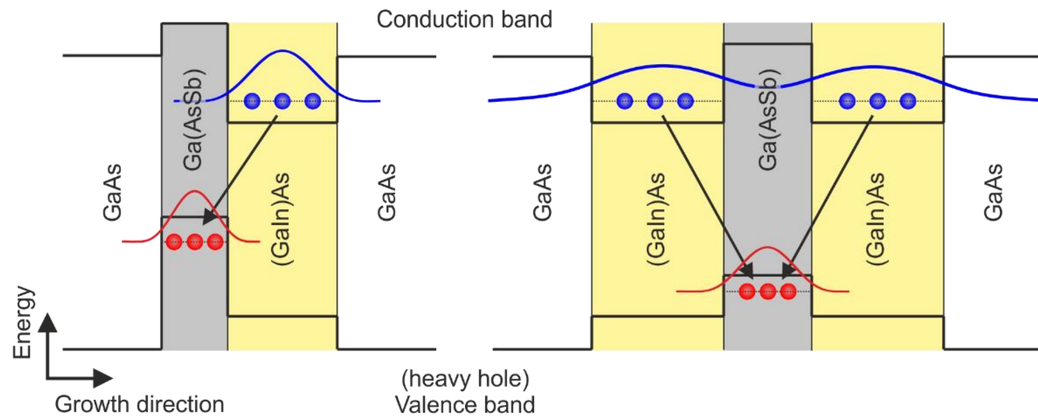

Figure 6.1. Scheme of the Ga(AsSb)/(GaIn)As/GaAs bilayer QW (left) and the corresponding "W"-QW, where the hole confining Ga(AsSb) layer is enclosed by (GaIn)As electron confining layers.

a hole confining potential well, whereas the (GaIn)As layer is confining the electrons. Due to an overlap of the probability density distributions of the given electron and hole states in the distinct layers, a radiative recombination can take place.

This principle is demonstrated in comparisons of the respective PL of the single QWs (SQWs) with the bilayer QW by Peter et al.. The peak wavelengths of the Ga(AsSb)/GaAs and (GaIn)As/GaAs SQWs at 77 K are 1140 nm and 1035 nm, which corresponds to photon energies of 1.09 eV and 1.20 eV, respectively. In contrast, a peak wavelength of 1190 nm is observed for the BQW (also at 77 K). The corresponding photon energy of 1.05 eV can only be related to a recombination of holes from the Ga(AsSb) well and electrons from the (GaIn)As well. In other words, two materials with larger band gap are combined to access a lower photon energy. It is also demonstrated that the emission wavelength of the BQW can be greatly altered by varying layer thicknesses as well as the antimony and indium contents. In this way, a peak wavelength of 1.33 µm (at room temperature) was measured for thicknesses of 4 nm and 7 nm as well as antimony and indium contents of $x = 33$ % and $y = 18$ % [120]. Peter et al. observe that the FWHM of the (GaIn)As/GaAs SQW is only 7 meV, while FWHM of 40 nm and 50 nm are observed for the Ga(AsSb)/GaAs SQW and the BQW, respectively. Similar observations have also been made by other works on the same material system [109, 127]. A feature of the type-II PL is a characteristic blue shift with increasing carrier density, which also will be discussed in the following section.

Room temperature lasing with the discussed design as gain medium was demonstrated by Ryu et al. and Klem et al. [124, 125]. At an emission wavelength of 1.2 µm an output power of 140 mW was observed from an edge-emitting diode laser [124]. A remarkable result of these works is that the lasing wavelength is significantly shorter than the peak wavelength of the electroluminescence, which illustrates the strength of the characteristic blue shift. Ryu et al. observe a blue shift of even 80 nm between low excitation density electroluminescence and laser operation. However, the low output power might be related to a weak overlap between the electron and hole probability density functions which results in a low transition probability.

Fortunately, the design can be significantly improved by embedding the Ga(AsSb) hole confining layer between two (GaIn)As electron confining layers as illustrated in Fig. 6.1 (right). Due to the "W" shaped band line-up of the conduction band, such design is also often referred to as "W"-QW. The design was initially proposed for materials based on InP substrate [117], but there are also experimental and theoretical studies for the GaAs system [127]. Dowd et al. performed PL studies,

which also demonstrate the wavelength flexibility of the design, as well as the characteristic carrier density dependent blue shift [128]. The theoretical works by Chow et al. are dedicated to the significant material gain blue shift with increasing carrier density [129, 130].

These studies suggest that the "W"-QW design can also serve as gain medium in VECSELs. It could not only enable the realization of more efficient devices beyond 1.2 µm, but applications could also benefit from the different characteristics of the material gain. To take this approach, it is reasonable to start with a design wavelength of about 1.2 µm. Nevertheless, to exploit the full advantage of the "W"-QWs, longer emission wavelengths are desired for the future. However, an increase of the design wavelength is also accompanied by several challenges. The access to longer wavelengths requires the realization of increased layer thicknesses which impair the thermal resistance (cf. Fig. 2.10). At the same time, it is desired to keep the 808 nm pump. Thus, also the quantum defect is increasing with the laser wavelength, too, and altogether the heating of the VECSEL becomes a major concern.

In a type-I QW, there are two parameters, namely its width and composition, which can be tuned while the design wavelength can be maintained. Assuming symmetry of the "W"-QW, there is the possibility to vary the widths and composition of two layers, namely the hole and the electron confining wells. Consequently, there are more design possibilities for one specific emission wavelength. These designs can yield significantly different gain values. Moreover, the band offsets play a more critical role for the emission wavelength, as the energy states of the hole wells depend on the band offsets of both, the (GaIn)As and the Ga(AsSb) wells. In this context, it is even more beneficial to apply a predictive theory for the modelling of the "W"-QW. The designs which are investigated in this thesis, are a result of the theoretical work by C. Berger [131]. It can be shown that the emission wavelength is 1188 nm, if even indium and antimony contents of 20 % are chosen as well as layer thicknesses of 6 nm and 4 nm, respectively. This design should yield promising gain amplitudes as high as 500/cm at a carrier density of $3 \times 10^{12}/\text{cm}^2$ and is hence the starting point of the present investigation.

6.2 Photoluminescence studies

Four representative MQW samples with ten QWs each are studied in the following. A report about the challenges of the MOVPE growth is provided by Fuchs et al. [132]. The samples' compositions are obtained from HR-XRD measurements and summarized in Tab. 6.1. Two samples contain the individual (GaIn)As/GaAs and Ga(AsSb)/GaAs QWs. As can be seen from Tab. 6.1, the indium and antimony concentrations are close to the desired value of 20 %. Also the layer thicknesses of 6.1 nm and 3.9 nm match the design. The determined optimized conditions for the growth of these

Table 6.1. Overview on the compositions and PL properties of the studied 10 × MQW samples.

	SQWs		"W"-QWs	
	(GaIn)As	Ga(AsSb)	Sample 6.1	Sample 6.2
QW thickn. (nm)	6.1	3.9	5.6 / 4.2 / 5.6	5.7 / 4.0 / 5.7
In conc. (%)*	21.3	–	21.7 / – / 21.7	21.6 / – / 21.6
Sb conc. (%)*	–	18.8	– / 17.3 / –	– / 21.3 / –
Peak wavelength (nm, eV)	1008.7, 1.229	1065.8, 1.163	1166.5, 1.063	1228.7, 1.009
FHWM (nm, meV)	13.4, 16.3	51.8, 57.1	56.3, 51.8	67.5, 55.8

*The accuracy of the In/Sb contents is ± 1.5 %.

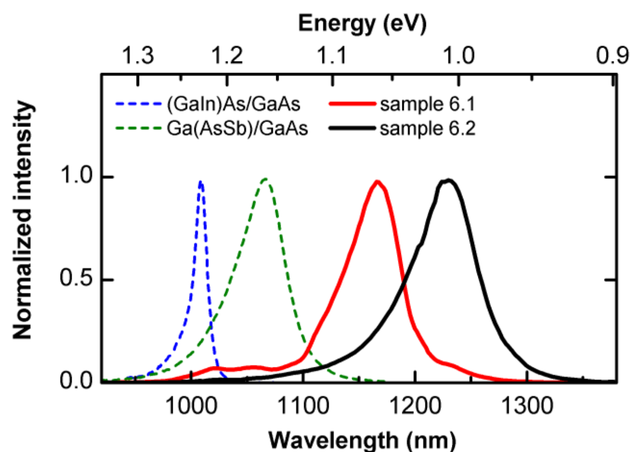

Figure 6.2. Comparison of the PL spectra from the (GaIn)As/GaAs and Ga(AsSb)/GaAs MQWs as well as the “W”-MQWs (samples 6.1 and 6.2).

QWs were used for the growth of the “W”-MQW samples. Two of these samples are studied here. They exhibit comparable indium contents and layer thicknesses but can be distinguished by the difference in their antimony contents (samples 6.1 and 6.2). Sample 6.1 exhibits an antimony content of 17. 3 %, while sample 6.2 exhibits a higher content of 21.3 %.

A regular PL measurement setup, also used in chapter 5.1, was used for the PL measurements. The excitation wavelength is 514 nm and the excitation intensity is 0.25 kW/cm² for all samples. A comparison of the obtained spectra is represented by Fig. 6.2. It illustrates the functionality of the “W”-QWs. The (GaIn)As/GaAs MQW exhibits the shortest peak wavelength of 1009 nm, the Ga(AsSb)/GaAs MQW has a peak wavelength of 1066 nm. In contrast, the “W”-MQWs exhibit peak wavelengths of 1167 nm (sample 6.1) and 1229 nm (sample 6.2). These findings are consistent with the aforementioned work by Peter et al. [120] and the difference in the photon energy between the constituting QWs and the “W”-QWs can only be understood in terms of type-II transitions between the spatially separated electron and hole states. Following this picture, it is also reasonable that an increased antimony concentration is related to longer emission wavelengths. Also similar observations are made concerning the linewidth. The narrowest spectrum is observed for the (GaIn)As/GaAs MQW (13 nm). The other spectra are clearly broadened with FWHM between 52 nm and 68 nm (cf. Tab. 6.1).

Comparing only the “W”-QWs, the spectra of samples 6.1 and 6.2 exhibit somewhat different shapes. The difference becomes apparent at the short-wavelength tail which is smooth in case of sample 6.2 but exhibits some weak local maxima at 1020 nm (1.215 eV) and 1060 nm (1.170 eV) in case of sample 6.1. Due to the lower antimony content in sample 6.1 the confinement potential of the holes within the center layer should be reduced. This should promote the recombination of charge carriers at higher states, such as the direct transition in the (GaIn)As electron wells. Please note that these states are different from the single QW because the effective well width ranges over the whole “W”-QW. This is especially the case for electrons, but also for higher hole-states, which are not confined in the Ga(AsSb) well. This should reduce the transition energy of the direct transitions in the “W”-QW in comparison to the (GaIn)As/GaAs SQW.

In order to identify the involved transitions, a thorough experiment–theory comparison was performed by Gies et al. [133]. The samples used for this experiment were cleaved from the same wafers as sample 6.1 and 6.2. Photomodulation reflectance (PR) spectroscopy was applied to experimentally locate the frequencies of transitions between electron and hole states. The obtained

PR spectra were compared to calculated spectra from a microscopic theory. The good agreement between experiment and theory finally enables an identification of the involved QW states. The result is that for both samples only indirect transitions can be excited with photon energies from 1.0 eV to 1.2 eV. In more detail, the peak wavelength corresponds to the e1–h1 transition, with e1 indicating the electron ground state and h1 the hole ground state. The observed transition energies of 1.066 eV and 1.010 eV by Gies et al. are also consistent with the photon energies in Tab. 6.1. Other observed indirect transitions are the e2–h2 transition (1.180 eV) in sample 6.1 as well as the e2–h2 (1.112 eV) and the e1–h3 (1.160 eV) transition in sample 6.2. These results imply that the higher h2 and h3 states are still confined in the (GaAs)Sb layer. However, in case of sample 6.1 the e1–h3 transition is predicted to be very weak which explains that it was not observed in the experiment. These results also explain the observed local maximum at 1.170 eV in sample 6.1, which coincides with the e2–h2 transition. Referring to Gies et al., the local maximum at 1.215 eV can be related to the lowest direct transition between the e1 and h4 states.

In order to further study the nature of the "W"-QW design, samples 6.1 and 6.2 are also investigated by power dependent PL measurements. As mentioned above, a characteristic blue shift of the PL with increasing carrier density was observed for optically and electrically excited type-II QWs [120, 124, 125]. It was also simulated that the blue shift is an inherent result of the charge separation and

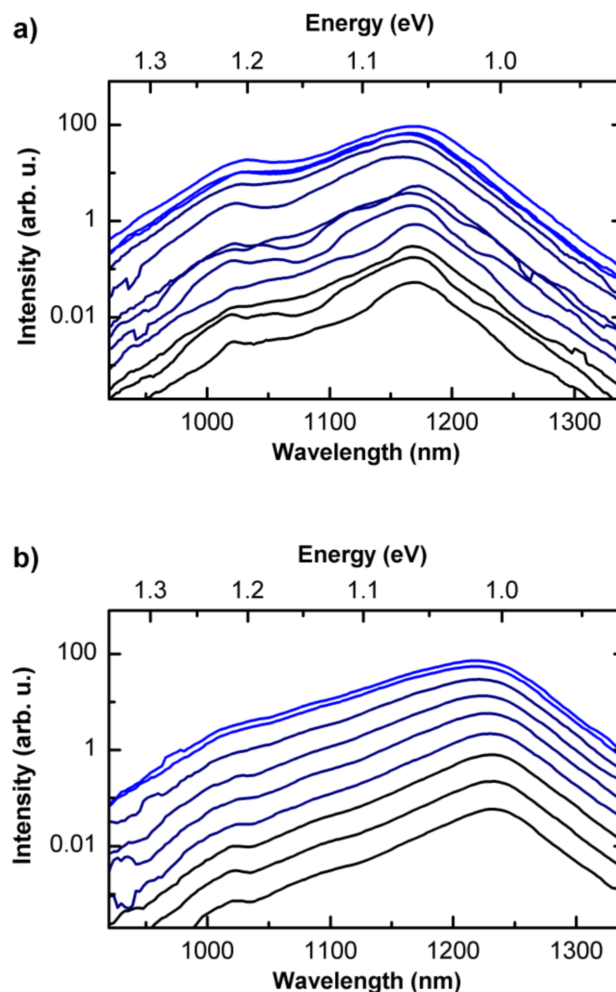

Figure 6.3. Power dependent photoluminescence measurements on a) sample 6.1 and b) sample 6.2.

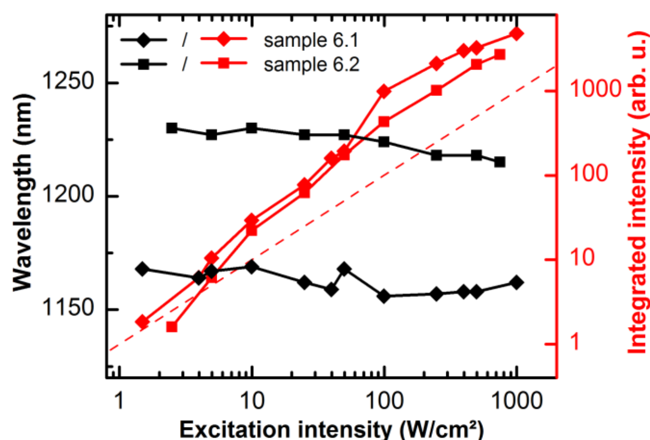

Figure 6.4. Peak wavelength (left axis) and integrated intensity (right axis) versus excitation density.

closely related carrier-induced band distortions [129]. In view of laser operation, such a blue shift is of great interest. The desired emission wavelength can only be obtained, if the magnitude of the blue shift is known. In particular, the detuning in resonant VECSELs is of major concern (cf. chapters 3 – 5). The choice of the "correct" detuning requires an exact knowledge of the power dependent material gain shift as a function of carrier density.

The spectra of the power dependent PL of samples 6.1 and 6.2 are shown in Fig. 6.3. The plot of the peak wavelength against the excitation density reveals a slight blue shift (cf. Fig. 6.4). It is therefore likely that the blue shift is somewhat compensated by simultaneous heating of the samples due to the large quantum defect of about 43 % between the 514 nm excitation and the ~1200 nm PL peak wavelength. The integrated intensity (right axis) shows no indication of a saturation of the PL intensity at the maximum excitation intensity of about 1 kW/cm², though. The dashed line indicates the slope of unity, which corresponds to the ideal emission without the effect of defect or Auger recombination. At low excitation densities, the slope of the measured data is somewhat higher than unity and which can be attributed to the influence of defect recombination at a low carrier density. At a higher density, the slope is close to the ideal value of one, which overall shows a good material quality. It should be noted that excitation intensities of about 1 kW/cm² are usual for VECSEL thresholds, as demonstrated in the previous chapters. An 808 nm pumped VECSEL furthermore exhibits a smaller quantum defect and a superior heat removal due to the flip-chip bonding onto a CVD diamond. Hence, a blue shift which is possibly compensated by heating in the PL measurement, could be much more significant in a VECSEL. The power dependent spectra are compared to a fully microscopic theory by Berger et al. [134]. A good agreement between experiment and theory is found. The theory also confirms a blue shift with increasing carrier density. Remarkably, gain values as high as 500/cm are predicted for both samples at a carrier density of 3×10^{12}/cm² which is the same order of magnitude as for type-I QWs.

As a last study prior to the application of the "W"-QW design in a VECSEL, the temperature dependent PL of sample 6.1 is studied. For this, the same setup as for the power dependent measurements is used but the sample is mounted in a helium cooled cryostat. The excitation density is set to 25 W/cm² and the temperature is varied from 11 K to 292 K. The recorded spectra are presented in Fig. 6.5 a). It is observed that the high-energy tail of the spectra is steep at the lowest temperatures. The slope decreases while the temperature is increased. This can be understood in terms of recombination of hot charge carriers in higher states. In contrast, the low energy tail, which

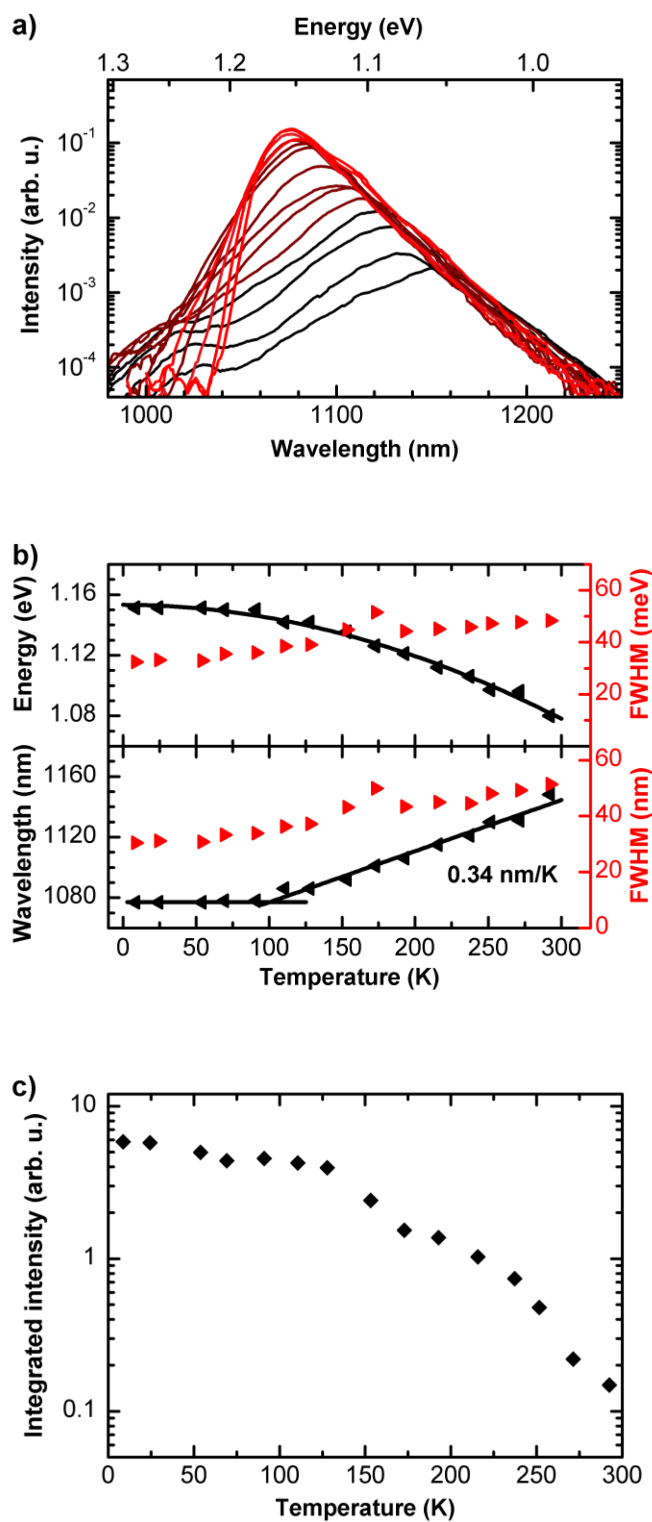

Figure 6.5. Temperature dependent PL of sample 6.1. a) Measured spectra, b) Evaluation of the FWHM and peak wavelengths on energy and wavelength scale, and c) integrated intensity.

correlates with the joint carrier density of states, exhibits a constant slope over temperature. The essentially linear increase of the FWHM with temperature is plotted on wavelength and energy scale in Fig. 6.5 b). The evaluation of the peak energy is also interesting. As discussed in section 3.3, the energy shift of type-I QWs can often be well described by the empirical Varshni equation [27, 67]. However, the energy shift could be different in case of the "W"-QW, since the individual (GaIn)As and Ga(AsSb) layers do not only have different Varshni parameters but also the band offsets may be altered differently with temperature [27]. The peak energies and wavelengths are also shown in Fig. 6.5 b). It is demonstrated that the energy shift can still be well described by a Varshni fit, which yields a band gap energy of E_0 = 1.153 eV at 0 K, as well as the Varshni constants α = 9.3 meV and β = 1083 K [27]. On wavelength scale, the shift can be well described by a constant rate of 0.34 nm/K. Interestingly, the shift rate is very similar to what is obtained for the type-I QWs (cf. chapters 3 – 5). To investigate these findings, measurements could be performed with the constituting (GaIn)As/GaAs and Ga(AsSb)/GaAs QWs and the Varshni-parameters could be compared. Figure 6.5 c) also shows the integrated intensity in dependence on temperature. It is demonstrated that the intensity is only decreased by less than two orders of magnitude, which is an indicator for a good material quality.

The conclusion of the PL measurements is that the "W"-QW design should be well suited for application as gain medium in a VECSEL. A comparison between theory and experiment shows that the present design is well-understood. In particular, remarkable gain values are predicted. However, the development of a first VECSEL device still remains a challenge, as is discussed in the following section.

6.3 VECSEL design and samples

The "W"-MQW samples 6.1 and 6.2 are very similar to a RPG structure which can be employed in a VECSEL. Only a few additional modifications are necessary to obtain a VECSEL design. The PL samples exhibit strain compensating Ga(AsP) separation layers between the "W"-QWs with phosphorus contents of 3 %. This is also suitable for 808 nm barrier-pumped VECSELs. However, the PL samples do not exhibit a cap layer. Its importance was demonstrated in the previous chapter. The cap layer is not only required as etch stop for the wet chemical etching in the flip-chip bonding process, but it also serves as a barrier to confine the charge carriers within the gain region. With respect to the low P-content Ga(AsP) barriers, a cap of $(Ga_{0.52}In_{0.48})P$ forms a suitable barrier for the charge carriers.

Moreover, the optical cap layer thickness and the separation of the QWs are a critical design parameter. As in the previous chapters, these layer thicknesses are adjusted to obtain a specific detuning for a given material gain peak wavelength. However, the "optimal" detuning is highly correlated to a multitude of parameters, most notably the pump intensity, the thermal resistance and the respective power and temperature dependent shift rates of the material gain. Indeed, it was demonstrated in chapter 4 that an "optimal" detuning can be determined both experimentally and theoretically, but these studies were based on advanced type-I VECSEL structures that had been developed over decades. In contrast, a type-II VECSEL has not been demonstrated before. Thus, threshold pump intensities and the corresponding theoretical carrier densities were not compared so far. Moreover, the strength of the carrier dependent blue shift of the material gain is not identified, which further complicates the prediction of an "optimal" detuning. Three different scenarios may be observed for the built up of material gain:

- Pump induced heating of the gain region overcompensates the blue shift. Consequently, the material gain peak wavelength is red shifted in comparison to the low excitation density PL.
- The blue shift is compensated by heating. No effective shift is observed between the low excitation density PL and the material gain peak wavelength.
- Material gain is build up at sufficiently low pump intensities which do not cause significant heating. The material peak wavelength is shifted blue in comparison to the low excitation density PL.

Depending on which scenario is present, the respective strategy for the detuning has to be chosen. If scenario one or two are present, the previously discussed strategies for type-I VECSELs apply. A vanishing or rather negative detuning is preferable to obtain a low laser threshold. However, if scenario three applies, the detuning should be chosen to be positive. Otherwise, material gain and confinement factor deviate from one another with increasing carrier density.

Fortunately, the previously discussed PL studies help to exclude the first scenario. Indeed, only a weak blue shift is observed in the power dependent PL measurements (cf. Figs. 6.3 and 6.4), but the quantum defect and thermal resistance are significantly larger in comparison with flip-chip bonded VECSEL chips. Samples 6.1 and 6.2 have not been bonded onto a diamond heat spreader, but the substrate side is glued onto the sample holder. Hence, the heat has to be removed through the 500 µm GaAs substrate. Also, the sample is excited at 514 nm which results in a quantum defect of 43 % instead of 33 % with 808 nm pump. If there is a compensation of the blue shift in the PL measurements, the observed blue shift should be significantly stronger in a VECSEL chip. Hence, it can be expected that rather scenario two or three will apply to type-II VECSELs.

Therefore, a reasonable design is based on either a vanishing or a positive detuning. However, there is another challenge concerning the realization of the VECSEL. In contrast to the samples from the previous chapters, the MOVPE growth of the VECSELs was performed in two different reactors. The cap layer and the DBR were grown in the same reactor as the samples from chapters 3 – 5. However, the gain region was grown in a smaller research-type reactor system [132, 134, 135]. A typical value for the relative deviation of layer thicknesses between two consecutively grown structures is about 2 %. This relates to an absolute deviation of the LCF of ± 15 nm with respect to the peak wavelength at 1200 nm. Therefore, it is difficult to accurately match a designed detuning. Moreover, there is some fluctuation in the PL peak of two consecutively grown “W”-MQWs in the small research-type reactor system.

The approach is hence, to grow multiple samples with the design for 1200 nm (both QW emission and LCF peak wavelength). Due to the fluctuations between the different epitaxy runs, it is likely that a set of samples with different detunings is obtained. In the following, three representative samples from the different epitaxy runs are investigated. The chip design is summarized in Fig. 6.6. It is very similar to the previously investigated type-I VECSELs (cf. Fig. 2.2). As discussed above, a 10 × “W”-MQW with Ga(AsP) strain compensating layers is grown as RPG. Table 6.2 summarizes the compositions of the realized “W”-QWs of the respective VECSEL samples 6.3 – 6.5. It can be seen that the previously investigated “W”-QW compositions of the PL samples could be reproduced. The indium contents of the electron wells are close to 20 % in all samples. The corresponding thicknesses vary between 4.8 nm and 6.1 nm. With regard to the hole wells, the antimony contents are about 24 % for sample 6.3 and about 20 % for samples 6.4 and 6.5. The hole well thicknesses are close to 4 nm for all samples. Based on the previous PL studies,

Table 6.2. Summary of the "W"-QW compositions of the realized type-II VECSELs.

	Sample 6.3	Sample 6.4	Sample 6.5
QW thickn. (nm)	4.8 / 3.5 /4.8	5.5 / 4.0 / 5.5	6.1 / 4.0 / 6.1
In conc. (%)*	19.6 / – / 19.6	20.3 / – / 20.3	20.0 / – / 20.0
Sb conc. (%)*	– / 24.1 / –	– / 19.8 / –	– / 20.3 / –

*The accuracy of the In/Sb contents is ± 1.5 %.

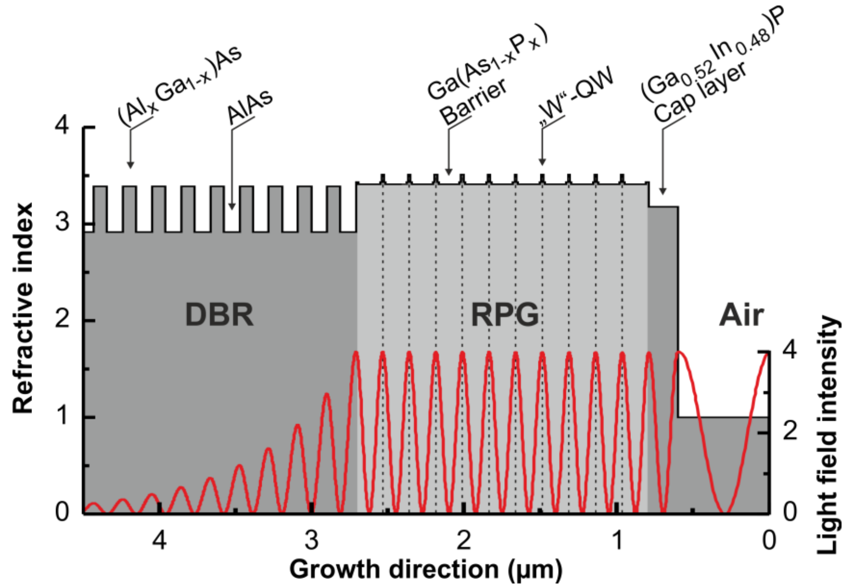

Figure 6.6. Design of a type-II VECSEL for the emission at 1.2 µm. The design is very similar to the type-I VECSELs in chapters 3 to 5 and as illustrated in Fig. 2.2. For a better illustration of the RPG region, only 9/22 pairs of the (AlGa)As/AlAs DBR are shown.

it must be expected that, due to the increased antimony concentration, the longest PL peak wavelength is observed for sample 6.3. Sample 6.4 and 6.5 have a very similar composition and should exhibit a comparable emission wavelength. As discussed, a $(Ga_{0.52}In_{0.48})P$ cap layer is grown as barrier for charge carriers as well as etch stop. The distributed Bragg mirror consists of 22 pairs of $\lambda/4$ $(Al_{0.20}Ga_{0.80})As/AlAs$ layers. Also the flip-chip approach is applied here, i.e. the structures are grown bottom-up and bonded onto a 350 µm thick CVD diamond as described in section 3. Related to the simulations in section 2.3, the thermal resistance of the resulting chip should be comparable to the previously investigated type-I samples. In the following sections, these three samples will be investigated, thoroughly.

6.4 Detuning studies

An overview on the reflectance measurements, edge PL measurements, as well as the transfer-matrix calculations is given in Fig. 6.7 for samples 6.3 and 6.4 as well as Fig. 6.8 for sample 6.5.

Interestingly, the *TDR spectra* have a different signature in comparison to type-I samples (cf. Figs. 6.7 a, a') and Fig. 6.8 a)). There are only poor absorption dips within the stop band. This is not per se related to an anti-resonant QW arrangement, i.e. when there is no strong overlap between the LCF and the QW absorption. It must be rather related to the reduced absorption of the type-II transitions. A maximum material absorption of about 1000/cm for the present “W”-QW design is predicted by theory [134]. On the basis of the measurements on the reference sample (type-I QWs), where a relative absorption of 60 % is observed, an absorption of 15480/cm can be calculated with

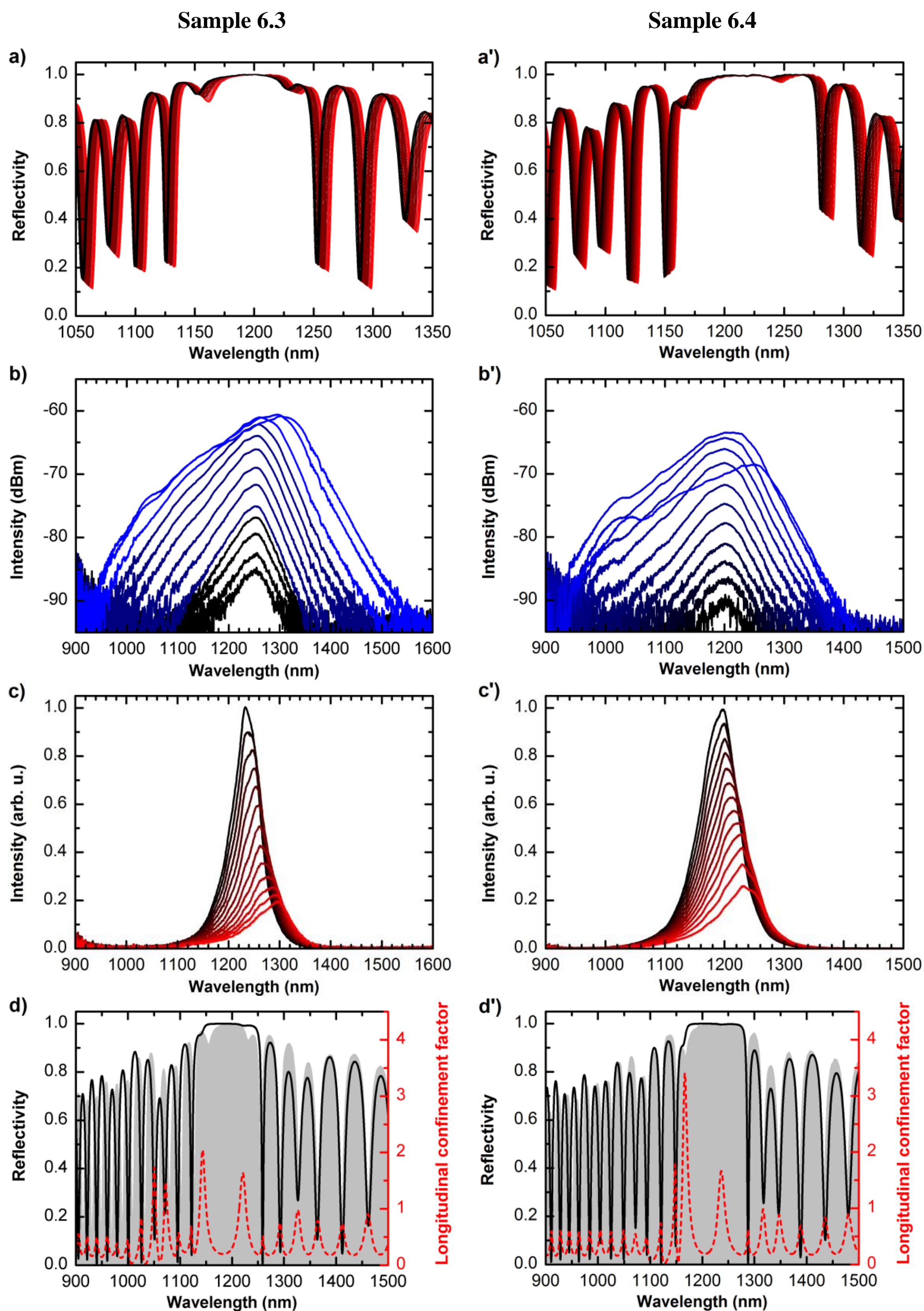

Figure 6.7. Overview on the studies of **samples 6.3 and 6.4**. The TDR measurements are shown in a, a'), the power and temperature dependent edge photoluminescence measurements in b, b') as well as c, c') and the transfer-matrix calculations of the reflectivity and confinement factor in d), and d').

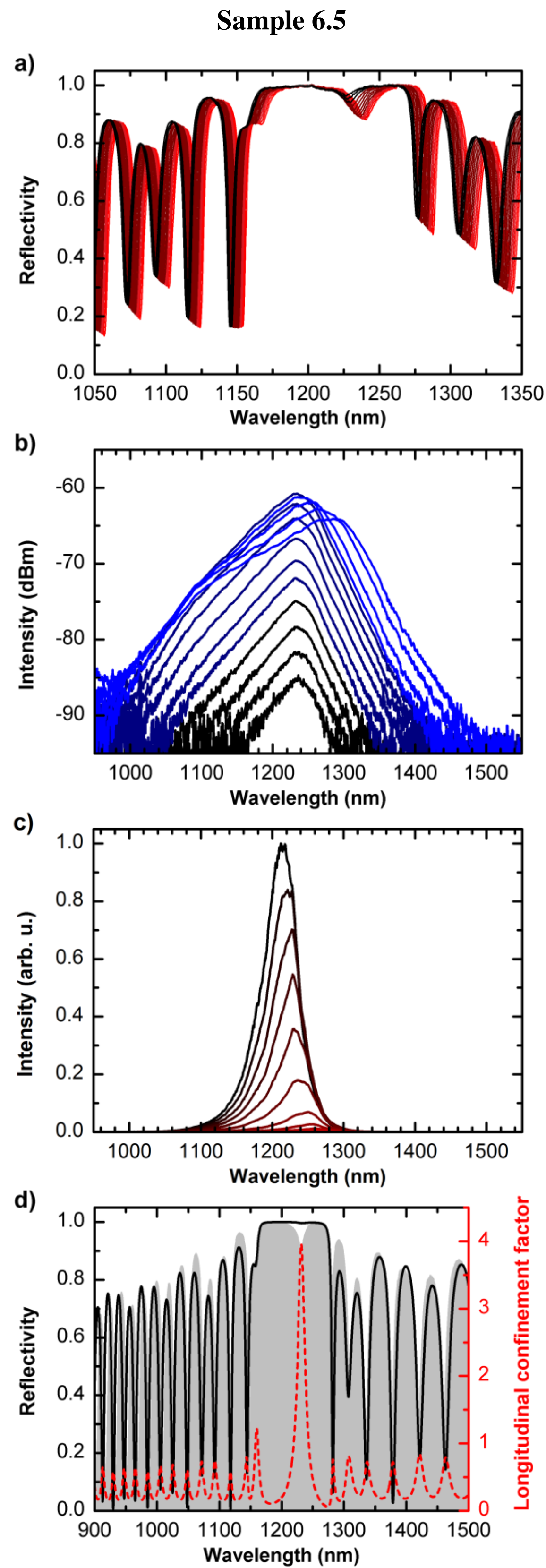

Figure 6.8. Overview on the studies of **sample 6.5**. The TDR measurements are shown in a), the power and temperature dependent edge photoluminescence measurements in b) as well as c) and the transfer-matrix calculations of the reflectivity and confinement factor in d).

Eqs. 3.3 and 3.4. Vice versa, a maximum relative absorption of 12 % can be obtained for the type-II QWs, assuming 10 × 16 nm thick resonantly aligned “W”-QWs and an LCF amplitude of 4. In case of type-I VECSELs, it could also be observed that absorption dips can occur within the stop band which cannot be related to the LCF maximum. An example of such behavior is provided by sample 4.1 where the absorption dip and the LCF do not coincide (cf. Fig. 4.6). Due to the significantly weaker but broader QW absorption of the type-II QWs, a different situation is present here. The absorption dips can be directly correlated with the maxima of the LCF in any case. For the interpretation of the temperature dependence, the shift rate of 0.08 nm/K of the micro-cavity resonance can be taken into account, as well as the above measured PL shift of 0.34 nm/K for the “W”-QW absorption.

Two absorption dips are observed within the stop band of *sample 6.3*. One is located between 1151 – 1161 nm, the other between 1227 – 1239 nm. These dips must relate to two distinct LCF maxima. The relative absorption of the first dip reaches a maximum of 12 % and the second a maximum of 4 %, respectively. Because these dips are ~ 80 nm apart, it is not possible that the first dip correlates to the theoretical maximum of the absorption from the e1–h1 type-II transition while absorption can still be observed at the other one. Referring to Gies et al., it can also not be related to a type-I transition [133]. It is more likely that the reflectivity of the stop band is not unity and then further reduced by the QW absorption of a higher type-II transition. This assumption is also supported considering the amplitude of the LCF maxima. In the present design the LCF maximum can only reach the theoretical maximum of 4, if it is aligned correctly close to the center of the stop band. The presence of two maxima within the stop band indicate that the respective LCF amplitudes are clearly reduced, as will be verified by the transfer-matrix calculations, later. Following this argumentation, the theoretical absorption maximum of a type-II transition cannot be achieved, if there are multiple absorption dips within the stop band. Overall, a more accurate location of the material absorption maximum can only hardly be identified from these spectra, since the second dip may be related to absorption at either the long-, or short-wavelength side of the maximum.

The situation is comparable in case of *sample 6.4,* i.e. two absorption dips are observed within the stop band. There must be a micro-cavity resonance at a wavelength between 1239 - 1248 nm, but there is also a more pronounced dip at the short wavelength edge of the stop band between 1164 – 1176 nm. At this point, it is not clear whether the latter occurs due to an artificial shape of the stop band edge, the presence of a micro-cavity resonance, or a combination of both. Also here, the interpretation of the signature is rather vague if the transfer-matrix calculations are not taken into account.

The interpretation should be clear in case of *sample 6.5* though. It exhibits only a single absorption dip at wavelengths between 1227 – 1241 nm. It can be expected that the light field is resonantly aligned and the LCF could also reach a maximum of 4. The depth of the dip is 4 % at -20°C heat sink temperature and reaches a maximum of 12 % at a temperature of 100°C which is the aforestated theoretical maximum. This can be interpreted as a TDR of a type-II VECSEL with small negative detuning.

In summary, it is difficult to approximate the detuning from the TDR measurements. In case of type-I VECSELs, good approximations could be achieved, but due to the broader and weaker absorption of type-II QWs, it is more difficult to locate the material absorption maximum. Still, the TDR measurements give accurate information about the location of the LCF maxima.

And yet, it is even unclear if the detuning can be determined by the *measurement of the edge PL.* The characteristic intensity dependent blue shift of the PL from the type-II QWs could prevent the

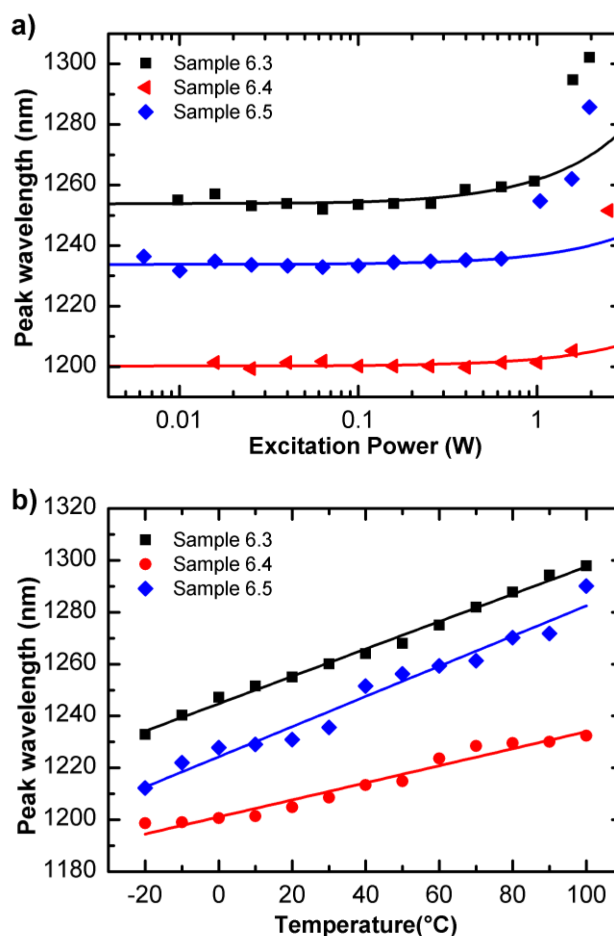

Figure 6.9. a) PL peak wavelength versus excitation power recorded at 20°C, b) peak wavelength versus temperature for samples 6.3 – 6.4. The excitation power is 100 mW.

specification of a low excitation intensity peak wavelength. To evaluate this, the peak wavelengths are extracted from Figs. 6.7 b, b', c, c') and Figs. 6.8 b, c) and plotted versus power and temperature in Figs. 6.9 a) and 6.9 b). Fortunately, the power dependent peak wavelength of all three samples can be described by a linear fit over two orders of magnitude (cf. Fig. 6.9 a)). Consequently, a definite specification of a low excitation density peak wavelength is possible and which is 1254 nm, 1201 nm, and 1234 nm for samples 6.3 – 6.5, respectively. These values enable the determination of the detuning relating to Eq. 2.7. At excitation powers above 1 W, a different slope is observed, which must be related to the heating of the samples. Hence, these values are not considered in the linear regression.

Figure 6.9 b) illustrates the evaluation of the peak wavelength of the temperature dependent measurement. The data can also be described by a linear function, which results in temperature shift rates of 0.53 nm/K, 0.33 nm/K, and 0.58 nm/K for samples 6.3 – 6.5, respectively. However, there is some fluctuation around the linear fit which can be attributed to the altering shape of the spectra with varying temperature (cf. Figs. 6.7 c, c') and Fig. 6.8 c)). More specifically, they can be related to the presence of Fabry–Pérot resonances from the samples, which have a different temperature shift rate than the PL. In case of the type-I VECSELs, it was possible to avoid such fluctuations by slight adjustments of the angle between sample and the detection path (cf. Fig. 3.9). However, this was not successful in the present case of the type-II samples. Therefore, it is meaningful to indicate an error for the peak wavelength. A good measure for the error is the maximum deviation between

Table 6.3. Summary of the detuning determinations on the type-II VECSELs.

	PL peak (nm)	LCF peak (nm)	Detuning (nm)
Sample 6.3	1254 ± 3	1220	+ 34 ± 3
Sample 6.4	1201 ± 3	1168	+ 33 ± 4
Sample 6.5	1234 ± 8	1232	+ 2 ± 8

the respective linear regression and the measured peak wavelengths. The resulting errors are ± 3 nm, ± 4 nm, and ± 8 nm with increasing sample number, respectively. These errors must also be considered for the indication of the low excitation density peak PL which is used for the determination of the detuning.

As last step to complete the detuning studies, the transfer-matrix calculations are performed to fit the room temperature reflectance and simulate the LCF. The results are illustrated in Figs. 6.7 d, d') and Fig. 6.8 d). As in the previous chapters, the simulations are based on the thicknesses and compositions of the RPG obtained from HR-XRD measurements. The DBR layer thickness and the cap layer thickness are used as fitting parameters. The peak wavelengths of the LCF are summarized in Tab. 6.3. As expected, there is a good agreement of the LCF peak wavelengths with the absorption dips. In particular, also the dip at 1168 nm in sample 6.4 can be related to absorption and is not an artefact of the stop band edge.

Based on the acquired data, actually two detunings can be indicated for each sample, because there are two micro-cavity resonances within the stop band region. As mentioned above, it is expected that a detuning close to zero or even a positive detuning are required for lasing. Hence, it is only reasonable to indicate the detuning corresponding to the closest LCF peak at the short-wavelength side of the PL peak wavelength. The results are summarized in Tab 6.3. Sample 6.3 and 6.4 exhibit a positive detuning between + 29 nm and + 37 nm. Sample 6.5 exhibits detuning between -6 nm and + 10 nm.

6.5 Laser studies

For the laser studies, samples 6.3 – 6.5 are arranged one-by-one in a linear cavity. As in the previous chapters, a large pump spot is used to simplify the alignment, obtain a low thermal resistance, and decent output powers. Different mirrors are available for the emission wavelength at about 1.2 µm. In order to demonstrate laser operation of a type-II VECSEL for the first time, the mirror with the lowest transmissivity of 0.2 % is chosen. If laser operation can be accomplished, mirrors with transmissivities of up to 1.5 % can be used to optimize the performance.

With *sample 6.3* no laser threshold is achieved at holder temperatures above 5°C. At 5°C, however, lasing of an optically pumped type-II VECSEL is demonstrated for the first time. The output power is below 100 mW, but can be significantly enhanced by a reduction of the heat sink temperature (cf. Fig. 6.10). At heat sink temperatures of -15°C and below, the output powers exceed even 1 W. However, this power level is mainly attributed to the large pump spot size of 980 µm × 1100 µm which enables an application of high pump powers. The laser slope efficiency is below 3 %. Threshold intensities between 1.5 – 3.5 kW/cm² are observed (cf. Fig. 6.10 (right panel)), with the lowest threshold related to the heat sink temperature of -20°C. An exemplary spectrum is shown in the inset of Fig. 6.10. It was recorded at a temperature of -20°C and close to threshold. Remarkably, the laser wavelength is ~30 nm shorter than the low density edge PL peak wavelength at -20°C.

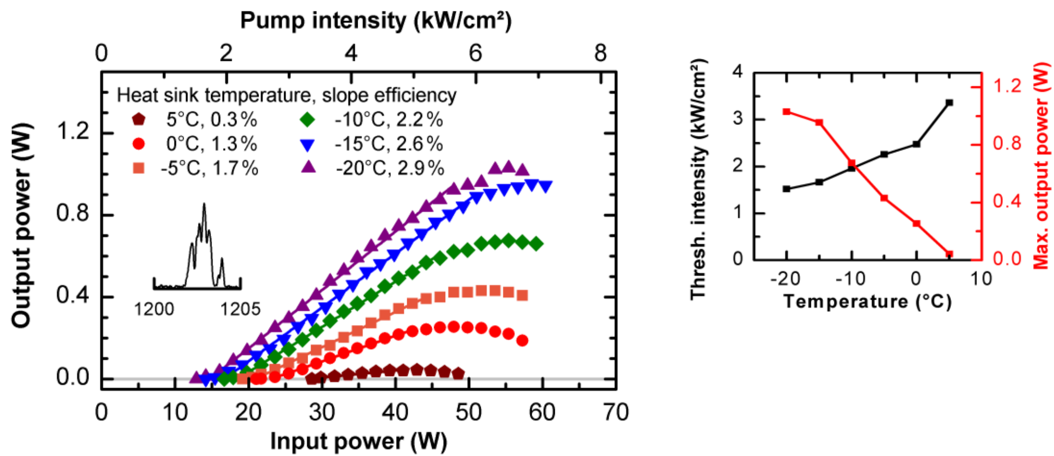

Figure 6.10. Power curves of **sample 6.3** for heat sink temperatures between -20°C to 5°C and with a 0.2 % output coupler. The inset shows an exemplary laser spectrum close to threshold. The threshold intensity and maximum output powers in dependence on the heat sink are summarized at the right hand side.

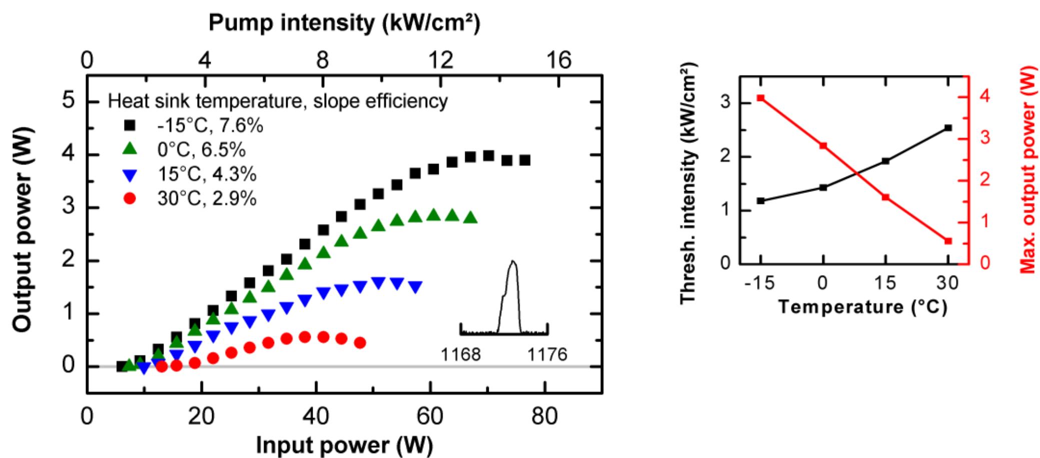

Figure 6.11. Power curves of **sample 6.4** for heat sink temperatures between -15°C to 30°C and with a 0.7 % output coupler. The inset shows an exemplary laser sprecrum close to threshold. The threshold intensity and maximum output powers in dependence on the heat sink are summarized at the right hand side.

Moreover, it does not exactly correlate to a peak of the LCF but to its short-wavelength tail. The question can be raised, whether lasing is based on a type-II transition. A comparison with the identified transitions by Gies et al. reveals that the closest type-I transition should not be beyond 1050 nm. Therefore, lasing can only be related to a type-II transition. Due to the weak transition probabilities between other type-II transitions, it is most likely that lasing is based on the e1–h1 transition [133]. This implies that the difference between the PL and lasing wavelength is actually due to a significant blue shift of the material gain. As a whole, the demonstration of output powers in excess of 1 W from a type-II VECSEL at the first attempt is a remarkable result. Taking into account that the structure is not optimized proves that the "W"-QW design is promising for the applications in VECSELs.

Next, *sample 6.4* is investigated. In contrast to sample 6.3, lasing is readily achieved even at room temperature. Also, lasing can be achieved not only with the 0.2 % mirror, but with the available 1.5 % output coupler, too. However, it is found that the best performance is achieved with a 0.7 % out-coupling mirror. The power curves with this mirror are presented in Fig. 6.11. Output powers of up to 1.2 W and 0.6 W are achieved at heat sink temperatures of 15°C and 30°C, respectively, which clearly demonstrates first room temperature operation of a type-II VECSEL. In comparison with sample 6.3, sample 6.4 clearly exhibits superior performance even though the pump spot size has been decreased to 750 µm × 870 µm. At -15°C a slope efficiency of up to 7.6 % is observed and a maximum output power of 4 W is achieved. Furthermore, the laser thresholds are between 1.2 kW/cm² and 2.5 kW/cm² which is also an improvement in comparison with sample 6.3 (cf. Fig. 6.11 (right panel)). An exemplary laser spectrum is recorded close to threshold and at a heat sink temperature of -15°C (cf. inset of Fig. 6.11). The laser wavelength at 1172 nm can be clearly correlated to the maximum of the LCF. As in the previous sample, the laser wavelength is ~30 nm shorter than the PL peak wavelength. At a heat sink temperature of -15°C, the PL peak is at 1199 nm and the LCF peak is at 1164 nm (cf. Fig. 6.9 a) and Tab. 6.3).

Interestingly, no lasing is achieved with *sample 6.5* in a linear cavity and with heat sink temperatures above 5°C, although the previous studies suggest that this is the most promising sample. It exhibits a LCF maximum close to the theoretical maximum of 4 at the center of the stop band. In contrast to the previous samples, its detuning is rather negligible (+ 2 ± 8 nm). This must be the main reason for the malfunction of this device, as samples 6.3 and 6.4 operate with a significant positive detuning. Fortunately, a positive detuning can be obtained for sample 6.5 by an arrangement of a V-cavity with the chip as folding mirror as demonstrated in chapter 4. It is anticipated that lasing is accomplished this way. This will be demonstrated and used for detuning studies later.

As intermediate summary of this chapter, the functionality of type-II VECSELs at 1.2 µm is demonstrated. Watt level output powers are observed which is a remarkable result. Although the laser threshold is already comparable to type-I VECSELs at 1000 nm (cf. chapters 3 and 4) and at 1180 nm [136], the slope efficiency of less than 10 % is rather low. However, the detuning studies show that the realized laser structures can be improved. The LCF reaches only a maximum of about 2 in case of sample 6.3. Sample 6.4 features an improved LCF amplitude, but it is located very close to the edge of the stop band which may involve a reduced reflectivity. An optimization of these parameters should decrease the laser thresholds and increase the slope efficiencies as well as output powers. It has to be expected that the samples do not exhibit an ideal detuning. The studies show clearly, that the devices require a positive detuning which is in contrast to the established type-I VECSELs (cf. chapters 3 – 5). Yet, the optimal detuning for type-II VECSELs is not known. The

remaining part of this chapter is, thus, dedicated to a more detailed study of the laser properties and its optimization.

Wavelength dependence, thermal resistance, and thermal roll-over

While the power curves of sample 6.4 were measured, the respective laser spectra were recorded simultaneously. These spectra are shown in false color plots for each heat sink temperature in Fig. 6.12. A continuous power dependent red shift is observed although a blue shift of the material gain must be present due to the compensation of the large positive detuning. At the peak output power, a maximum wavelength of 1182 nm is observed at all heat sink temperatures. Also, a temperature dependent red shift is observed which becomes visible at the laser thresholds. The threshold is at a wavelength of 1172 nm at -15°C and 1176 nm at 30°C heat sink temperature, respectively. The power and temperature dependences indicate that the maximum of the modal gain is dominated by the LCF. Considering the temperature shift rate of 0.08 nm/K, gain temperatures of 70°C are present at a wavelength of 1172 nm, and a gain temperature of 195°C at a wavelength of 1182 nm, respectively. These values seem to be unrealistically high in comparison to typical gain temperatures of type-I VECSELs. However, this approximation does not take into account that the maximum modal gain may not exactly be formed at the LCF peak. A more accurate analysis of the gain temperatures could be obtained by a thermal resistance measurement.

As discussed in section 3.5, an accurate determination of the gain temperatures can be performed with the shift-rate method. The only conditions for the applicability of this approach are linear power and temperature shift rates of the laser wavelength. In other words, the shift-rate approach can be applied, if Eq. 3.7 can be fitted to the experimental data. Based on the assumption that the

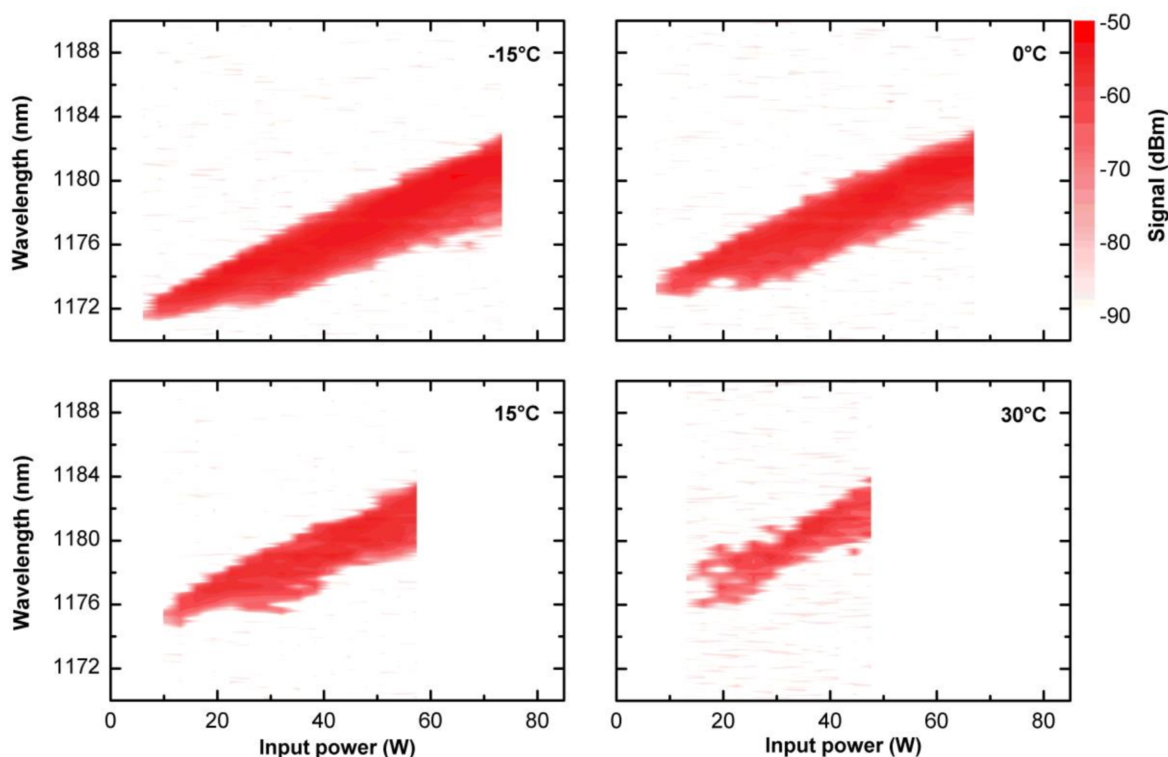

Figure 6.12. False color plots of the spectra which were recorded simultaneous to the power curves in Fig. 6.11.

maximum modal gain is clamped to the vicinity of the LCF peak, the maximum wavelength of each spectrum should correspond to the maximum gain temperature which is located at the center of the pump spot. Consequently, the procedure for the evaluation of the spectra should not be different to type-I VECSELs. Here, a signal drop of 10 dB at the long-wavelength side is chosen to define the maximum emission wavelength. The evaluated wavelengths against the dissipated power are shown as symbols in Fig. 6.13. Already, the data illustrates a linear behavior of the emission wavelength with both pump power and heat sink temperature. The small deviations between the measurement data and the fit with Eq. 3.7 confirm this finding. Hence, the fitting parameters can be extracted to determine the thermal resistance. A summary of the parameters is provided by Tab. 6.4. A thermal resistance of 1.57 K/W can be calculated with the linear shift rates of 0.16 nm/W and 0.10 nm/K. The pump spot size is, as mentioned above 750 µm × 870 µm. Normalization to a flat-top beam profile with the measured super-Gaussian order of m = 3.00 and Eq. 2.12 yields a thermal resistance of 1.59 K/W, respectively. This value agrees well with the simulation (cf. Fig. 2.10). Again, the error of the measurement can be determined assuming a scattering loss of 0.57 % and using Eq. 3.11. It is noteworthy that the error is reasonable, although the scattering losses are very similar to the output coupling of 0.7 %, because the output powers are low in comparison to the pump powers. Hence, the correction only affects a small fraction of the dissipated powers. As result the maximum thermal resistance should not exceed a value of 1.71 K/W, or 1.73 K/W for a flat-top pump profile, respectively. The highlight of the thermal resistance measurement are the determined gain temperatures (cf. Fig. 6.13, right axis). The threshold gain temperature at a heat sink temperature of 15°C is only 26 – 28°C. Furthermore, the roll-over temperature can be determined with help of the power curves. Two laser spectra which are closest to the point of roll over are indicated by the filled symbols. The dashed line indicates their average wavelength of 1182.2 nm and the gray area indicates an error bar of ± 1 nm due to the flat maximum of the power curve. Correspondingly, the roll-over occurs at temperatures of 90 ± 10°C, or 95 ± 10°C assuming the

Table 6.4. Summary of the thermal resistance measurement on sample 6.4

	$\partial\lambda/\partial P_D$	$\partial\lambda/\partial T$	λ_0	R_{th}	R_{th}/f	$T_{thr}^{15°C}$	T_{ro}
Measured	0.1568 nm/W	0.1004 nm/K	1173.2 nm	1.56 K/W	1.58 K/W	26°C	90°C
P_D corr.	0.1641 nm/W	0.0958 nm/K	1173.1 nm	1.71 K/W	1.73 K/W	28°C	95°C

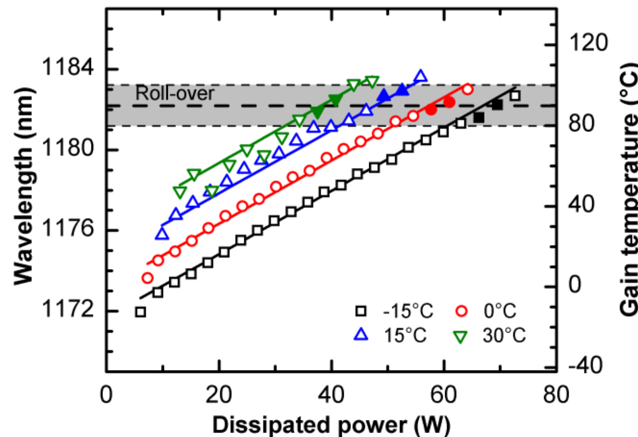

Figure 6.13. Thermal resistance measurement of sample 6.4. Symbols indicate the maximum wavelength which is extracted from the laser spectra (cf. Fig. 6.12) at a signal drop of -10 dBm. Filled symbols indicate the wavelengths which have been recorded close to the roll-over. The lines show the fit by Eq. 3.7.

scattering losses, respectively. In comparison to the reference sample in chapter 3 the gain temperature is hence somewhat lower at the roll-over. The rise of temperature at threshold is very comparable, though. Eventually, this prototype of a type-II VECSEL represents a low threshold device but suffers from an early separation of material gain and LCF maximum.

An interesting finding is also that the red shift of the maximum wavelength is still maintained beyond the roll-over. To investigate this behavior, the beam profile at the roll-over point is measured. For this, a fiber with a core diameter of 105 µm is mounted onto a x–y-translation stage (cf. Fig. 6.14). The fiber is connected to a power meter which only detects the transmitted light from the fiber. In this way, the intensity distribution of the VECSEL beam can be scanned. Moreover, a beam splitter is used to guide a part of the beam intensity to a power meter which detects the integrated intensity of the whole spot, respectively.

In a first measurement, the fiber is placed exactly at the center of the laser beam. Then, the pump power is varied in a range around the roll-over. The resulting power curves for the center or the whole spot are depicted in the top panel of Fig. 6.15 a). It is revealed that the center and the integrated intensity actually exhibit two distinct maxima. The maximum is achieved earlier at the center of the spot while the roll-over of the whole spot is delayed. Simultaneously, laser spectra were recorded for each data point in the power curve. Its 10 dB long- and short-wavelength signal drops are shown in the bottom panel of Fig. 6.15 a). As observed in the thermal resistance measurement, the wavelength is increasing linearly although the integrated intensity is already decreasing. This can be explained by the power curve of the center which is still not zero, i.e. the performance is locally decreased due to excessive heat, but lasing is still maintained. However, the power at the center reaches zero very close to the end of the viewed range and at this point, also the maximum emission wavelength is not further increasing. The linear increase of the minimum wavelength can also be related to a linear increase of the gain temperature at the edge of the pump spot. This also explains that the maximum and minimum wavelength converge before the laser shuts off.

The explained interpretation can be visualized by *a second measurement*, where the fiber is translated to scan the beam profile in x- and y-direction. This measurement is performed at the beginning and at the end of the presented power curves from Fig. 6.15 a). The top and bottom panel of Fig. 6.15 b) show the profiles before and after roll-over, respectively. The x-axis of the graphs is scaled to the pump size. It is observed that the beam profile follows the pump distribution before thermal roll-over. After roll-over, a donut profile is observed which demonstrates that at least the

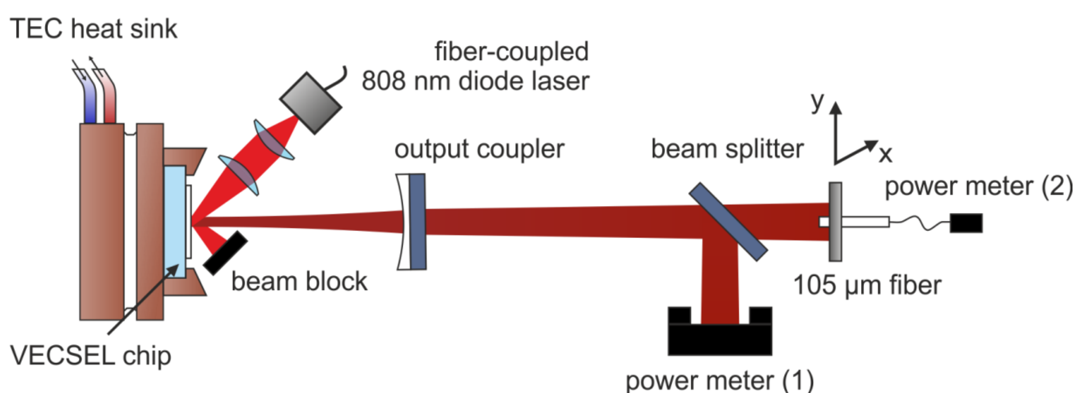

Figure 6.14. Scheme of the setup for the studies on the roll-over behavior of the type-II VECSEL

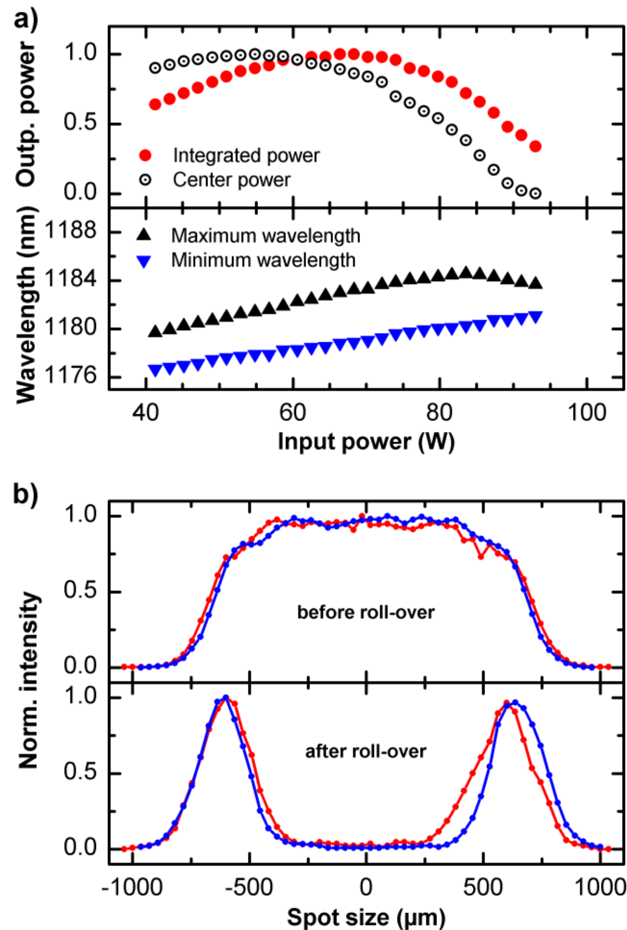

Figure 6.15. Results of the roll-over studies. a) Integrated intensity and center intensity against input power (top panel) as well as maximum and minimum emission wavelength against input power (bottom panel). b) Beam profiles in x- and y-direction before (top panel) and after roll-over (bottom panel).

TEM_{00} mode is not lasing anymore, while higher transverse laser modes at the cooler edge of the pumped region still remain. In summary, the roll-over behavior in multiple-transverse mode operation is identical to what is observed in type-I VECSELs with a similar pump profile [44]. The observed roll-over in the power curves of sample 6.4 can also be referred to as a thermal roll-over (cf. Fig. 6.11). And in retrospect to the thermal resistance measurement, the maximum gain temperature can be extracted from the maximum wavelengths, which can even be found outside the gray region (cf. Fig. 6.13). The highest measured wavelength is 1183.6 nm, which corresponds to a maximum gain temperature of 104°C, or 110°C assuming the scattering losses of 0.57 %, respectively.

Detuning dependences of a type-II VECSEL

The next study is dedicated to the detuning of type-II VECSELs. As mentioned above, sample 6.5 is not functioning in a linear cavity, but can be used for the V-cavity investigation as introduced in chapter 4. A plane mirror with a reflectivity of > 99.9 % is used as one end mirror. Its distance from the VECSEL chip is 28 mm. Different mirrors are used for the other end of the cavity in a distance of 35 mm to the chip. Their radius of curvature is -100 mm, the relating transmissivities will be indicated in the following discussion. This time, an 808 nm pump laser with output powers of up to 35 W is used for the experiment. The FWHM pump spot size is 350 × 360 nm and is larger than the

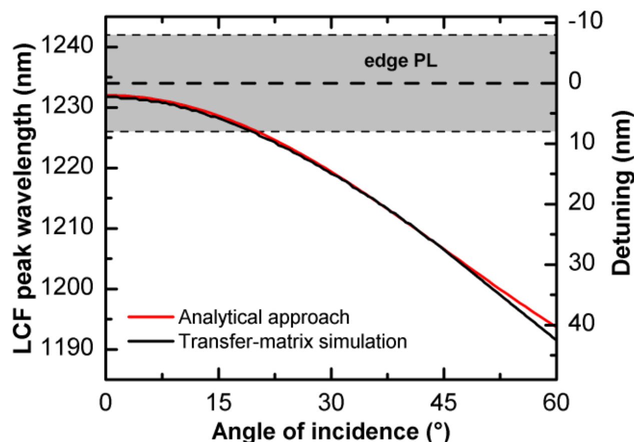

Figure 6.16. Calculation of the LCF peak wavelength in dependence on the cavity angle. The right axis indicates the detuning with respect to the edge PL peak wavelength which is indicated as dashed line. The gray area is the error bar from the edge PL measurement.

$1/e^2$ diameter of 240 µm of the TEM_{00} mode at the chip at small cavity angles. However, at an angle of 45° the $1/e^2$ diameter of the elliptical TEM_{00} mode is 340 µm, which is close to the FWHM of the pump spot. The heat sink temperature is held at 20°C throughout the experiment. According to Tab. 6.3, the room temperature detuning of sample 6.5 is + 2 ± 8 nm and the LCF peak is located at 1232 nm. Applying a transfer-matrix calculation to evaluate the shift of the LCF in dependence on the cavity angle yields an accessible range of detuning from + 2 ± 8 nm to + 42 ± 8 nm for angles between 0° and 60° (cf. Fig. 6.16). Also, the good agreement between a transfer-matrix calculation and the analytical approach is illustrated.

In the experiment, the angles 15°, 30°, and 45° are arranged which corresponds to detunings of + 6 nm, + 13 nm, and + 25 nm, respectively. At each angle, power curves and the corresponding laser spectra are measured with different output couplers, i.e. the curved mirror is exchanged. The complete set of measurements is shown in Fig. 6.17.

At an angle of 15°, lasing can be demonstrated with the 0.2 % out-coupling mirror (cf. Fig. 6.17 a)). Output powers of up to 75 mW are achieved. However, it is noteworthy that the output power is pump limited, because a maximum power of 21 W can be applied, also considering that 30.0 % of the pump light is reflected from the chip. The emission wavelength is between 1208 – 1218 nm. Remarkably, the wavelength does not correlate to the LCF peak at 1228 nm. At 1208 nm, the LCF is close to unity which indicates that the lasing wavelength is rather close to the material gain peak. This implies once more a blue shift of the material gain until threshold is achieved. However, as soon as laser operation is observed, a red shift of the emission wavelength is present, presumably due to heating as for the previous samples.

At the angle of 30°, lasing is observed even with a 1.0 % mirror. Consequently, also higher output powers of up to 300 mW can be achieved (cf. Fig. 6.17 b)). The emission wavelength is 1217 – 1220 nm, which stands for a significantly smaller wavelength range in comparison to the 15° angle. The wavelength can be furthermore related to the LCF peak which should dominate the modal gain and, thus, explains the reduced temperature sensitivity. At high pump powers, above 17 W, even a slight blue shift is observed which indicates that the material gain is still built up at the short-wavelength side of the LCF peak. This is also in agreement with the measurement at 15°. Furthermore, power curves are recorded with a 0.7 % and a 0.3 % mirror (cf. Figs. 6.17 c, d)).

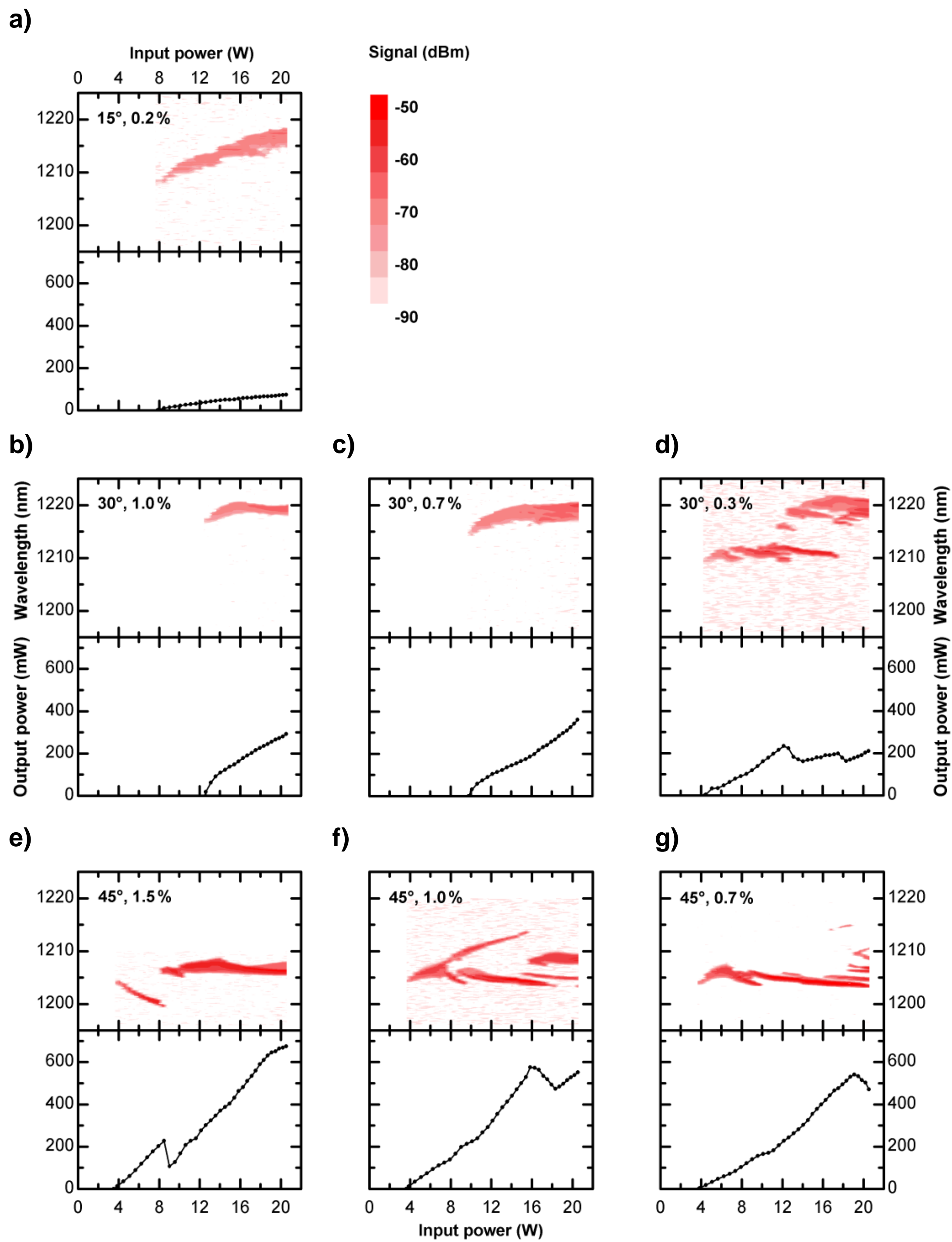

Figure 6.17. Measurements of the output power and laser spectra of **sample 6.5** in dependence on the input power and for the different cavity angles of a) 15°, b, c, d) 30°, and e, f, g) 45°. The transmissivities of the employed output couplers are indicated at each plot.

The maximum output power of 360 mW is observed with the 0.7 % mirror. Due to the reduced roundtrip loss, the threshold is reduced in comparison with the 1.0 % mirror and the threshold wavelength is decreased to 1215 nm. With the 0.3 % mirror, the threshold density and wavelength are further reduced. Interestingly, there is a splitting of the laser spectrum which can be explained by a competition of lasing between the material gain peak at 1210 nm position and the LCF peak at 1220 nm. The split up of the modal gain also damps the power curve.

The best performance is observed *at the angle of 45°*, where even the highest available output coupler of 1.5 % can be employed. The pump limited output power with the 1.5 % mirror is 670 mW (cf. Fig. 6.17 e)). In comparison to the 15° and 30° the threshold is further reduced. Interestingly, the laser spectrum shows a clear blue shift in the beginning. Probably, the laser threshold is achieved before the material gain shifts red due to heat. Above pump powers of 6 W, the laser wavelength is located close to the LCF peak wavelength, which is at 1207 nm. Furthermore, output couplers with 1.0 % and 0.7 % are employed (cf. Figs. 6.17 f, g)). The thresholds are similar to the 1.5 % mirror arrangement, but the laser spectra and output powers change significantly. Above input powers of 6 W the laser spectra split in different manners. However, lasing is observed at the LCF peak throughout the power curve. The split of the modal gain again causes a break down of the power curves.

The results from the detuning investigation are summarized in Table 6.5. There is a clear correlation between the detuning and all monitored laser quantities. The output powers are increased and thresholds are clearly reduced with an increase of the detuning. A comparison between the 15° and the 45° angle shows that the output power could be increased by almost one order of magnitude. The threshold is halved, although the intra-cavity losses are about eight times higher with the 1.5 % mirror. Overall, there is an excellent agreement between the calculations of the LCF peak wavelength with the laser wavelengths at the 30° and 45° angles. The poor laser performance at the 15° angle is explained by anti-resonant lasing, i.e. there is no good overlap of the LCF peak and the material gain peak. The improved overlap between the LCF and gain peak in case of the 30° and 45° angles is also demonstrated by the maximum output coupling. The higher cavity losses can be compensated which is also a direct demonstration of an increased modal gain. It is noteworthy that the best performance at the 45° angle is achieved with the 1.5 % mirror. No higher output coupler was available and the optimum output coupling could be even higher. The results also show that there must be two different regimes concerning the power dependent gain shift. Up to a certain pump level, the material gain shifts blue. This explains the necessity of a positive detuning for efficient laser operation. However, the laser spectra of sample 6.4 clearly shift red. The laser spectra of sample 6.5 in the 15° cavity also indicate a clear red shift, the strength of which cannot be correlated to the shift of the LCF. At the other angles, a splitting of the spectra is observed, but signatures appear always at the long-wavelength side.

Table 6.5. Summary of the detuning investigation.

Cavity angle	LCF peak wavelength	Detuning	Threshold density*	Max. output power	Max. mirror transmissivity
15°	1228 nm	+ 6 ± 8 nm	7.9 kW/cm²	~75 mW	0.2 %
30°	1219 nm	+ 13 ± 8 nm	4.4 kW/cm²	~360 mW	1.0 %
45°	1207 nm	+ 25 ± 8 nm	3.7 kW/cm²	~670 mW	> 1.5 %

*with lowest mirror transmissivity

The main point derived from these results is the great dependence of the laser performance on detuning. The results show that a room temperature detuning above + 25 ± 8 nm is preferable for the present QW design. This confirms the results which are obtained from samples 6.3 and 6.4, which both have a detuning of about + 33 nm. However, it is of importance that the specified range of preferable detuning only applies to the investigated QW design, because the blue shift depends on the carrier separation which is essentially depending on the thickness of the hole well. Hence, a different QW design can affect the optimal magnitude of the required detuning.

High beam quality TEM_{00} mode operation

While the previous investigations have dealt with the type-II VECSELs in multiple-transverse mode operation, this section is dedicated to the operation in TEM_{00} mode. A high beam quality is one of the key features of VECSELs and is required for most applications, e.g. if single-frequency, mode-locked operation, or intra-cavity frequency conversion is desired. Therefore, the performance and beam quality of the device is investigated if pump spot and cavity arrangement are optimized for TEM_{00} operation with a high beam quality.

In order to investigate the output characteristics in TEM_{00} operation, sample 6.4 is arranged in a linear cavity with a curved mirror (-100 mm radius of curvature) and a cavity length of 68 mm. This configuration is very similar to the arrangement in the previous sections 6.5 and 6.6. The best performance was observed with 0.7 % transmissivity which is also chosen here. The elliptical pump spot exhibits FWHM of 220 µm and 250 µm, respectively, which is comparable to the $1/e^2$ diameter of the TEM_{00} mode.

The power curve of the VECSEL operating in TEM_{00} mode and at a heat sink temperature of 15°C is shown in Fig. 6.18 (top panel). A maximum output power of 410 mW is achieved, which is approximately a quarter of the previously achieved output power in multi-transverse mode (at 15°C

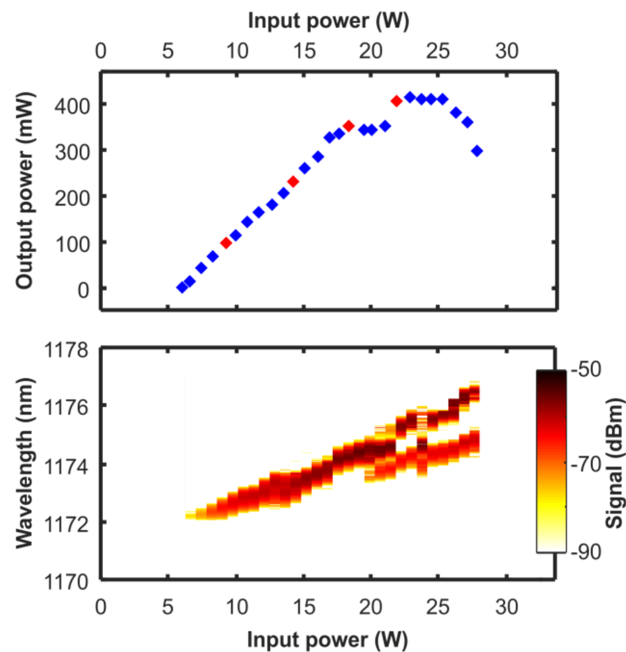

Figure 6.18. Power curve (top panel) and laser spectra (bottom panel) for sample 6.4 in TEM_{00} mode operation.

heat sink temperature with the 750 × 870 µm large pump spot size). The laser spectrum for each point of the power curve was recorded as shown in Fig. 6.18 (bottom panel). A threshold wavelength of 1172 nm is observed and the highest wavelength is 1177 nm. Close to the roll-over, a drop of the output power is observed which is accompanied by the initiation of two-color emission. This can be attributed to a competition between the TEM_{00} mode and the TEM_{01} or TEM_{10} mode where a part of the laser mode is located at the cooler border of the pump spot. This explains the second wavelength peak at shorter wavelengths which differs from the otherwise linear trend with a slope of 0.16 nm/W.

At the four highlighted data points in the power curve, the M^2 values are determined according to ISO 11146 [137]. A camera is built onto a linear translation stage. A lens with a focal length of 10 cm is arranged in front of the stage to focus the laser beam along the translation axis. The camera is moved through the focus of the beam while the beam profile is recorded in equidistant steps. According to ISO 11146 the D4σ sigma in x-direction is evaluated from the recorded profiles by the integral form

$$D4\sigma = 4\sqrt{\frac{\int_{-\infty}^{\infty}\int_{-\infty}^{\infty} I(x,y)(x-\bar{x}^2)\,dx\,dy}{\int_{-\infty}^{\infty}\int_{-\infty}^{\infty} I(x,y)\,dx\,dy}} \tag{6.1}$$

with the intensity of the beam along the x- and y-coordinates $I(x,y)$ and the centroid of the beam profile in x-direction

$$\bar{x} = \frac{\int_{-\infty}^{\infty}\int_{-\infty}^{\infty} I(x,y)\,x\,dx\,dy}{\int_{-\infty}^{\infty}\int_{-\infty}^{\infty} I(x,y)\,dx\,dy}. \tag{6.2}$$

The D4σ sigma width in y-direction is calculated accordingly. It can be followed from Eq. 6.1 that, due to the quadratic term in the numerator, the influence of the wings of the beam is weighted and even a low intensity at the wings can have a great impact on the M^2. Hence, for a correct M^2 determination, it is important to record the beam profile with the highest available dynamic range

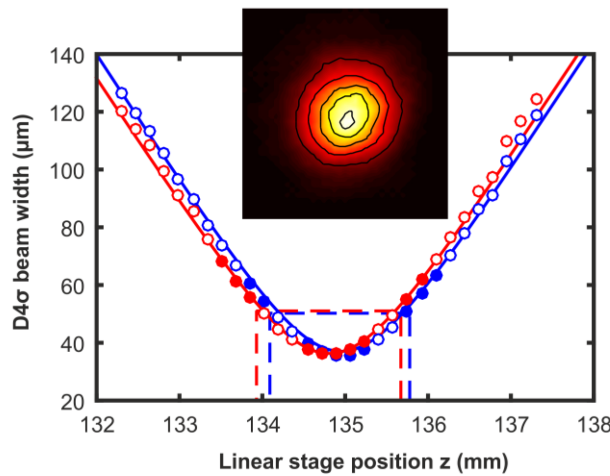

Figure 6.19. Exemplary M^2 measurement at an output power of 100 mW. The filled symbols of measured data for the x- (blue) and y-direction (red) indicate the data which is used for the fit with Eq. 6.3 (solid lines). The inset illustrates the beam profile.

Table 6.6. Results of the M² measurements at the different output powers.

Output power (mW)	M_x^2	M_y^2
100	1.09	1.13
230	1.18	1.18
350	1.19	1.19
410	2.01	1.59

and with lowest possible noise. To reduce the noise, a long pass filter is employed to cut off stray light from the ambient and the 808 nm pump laser. Furthermore, gain and brightness are adjusted carefully in order to account for the change of the intensity along the optical axes and to exploit the full dynamic range of the camera. After the measurement, the laser beam was blocked and a reference picture was recorded to determine the camera noise which is subtracted from the beam profile measurements. An exemplary M² measurement is presented for the output power of 100 mW in Fig. 6.19 which shows the D4σ beam width versus the CCD camera position in the beam profiler for both the x- (blue) and y-axis (red). Five filled points each in- and outside the Rayleigh length, which is indicated by the dashed lines, mark the data for the fitting procedure as it is required of the M² determination according to the ISO specifications. The solid lines show the best fit of these data points by equation

$$\sigma^2(z) = \sigma_0^2 + M^4 \left(\frac{\lambda}{\pi\sigma_0}\right)^2 (z - z_0)^2 \,, \tag{6.3}$$

where $\sigma(z)$ and σ_0 are the $D4\sigma$ beam width at position z and at the beam waist, respectively. The wavelength λ = 1174 nm is the average wavelength of the laser spectra in Fig. 6.18.

The almost circular beam profile is presented in the inset of Fig. 6.19. The gradient of the intensity is accentuated by black solid lines which indicate equal intensities. Moreover, the M² is measured at output powers of 230 mW, 350 mW, and 410 mW, respectively. A summary of the measurements is depicted in Tab. 6.6. Overall, an excellent beam quality with M² < 1.2 is observed up to an output power of 350 mW. However, close to the thermal roll over a flickering of the beam profile is observed which is also an indication of competition between the fundamental and a higher-order transverse mode. The elevated M² values at 410 mW output power are consistent with this assumption. It is noteworthy that the output power can be increased by a reduction of the heat sink temperature. At a similar arrangement and at a heat sink temperature of 0°C, 550 mW of maximum output power are achieved, respectively.

6.6 Summary and outlook

A novel VECSEL design for the emission beyond 1.2 µm was presented in this experimental chapter. The design is based on "W"-QWs which were modeled by a microscopic theory [131, 134]. In such type-II QWs, electrons and holes are spatially separated in materials with large band gap but can recombine spatially indirect with reduced transition energies. Hence, this concept can be employed to overcome fundamental strain limitations of conventional type-I designs.

As preliminary study, the functionality of the concept was experimentally proven by means of PL measurements on MOVPE grown samples [132, 134]. It was observed that the long-wavelength emission from the type-II QWs can be clearly distinguished from the short-wavelength emission

from the constituting type-I QWs. The characteristic property of the PL known from literature could be confirmed, i.e the blue shift with increasing carrier density. Moreover, the good agreement between experimental and calculated PL spectra was used as a basis for further studies. In particular, significant material gain could be predicted by Berger et al. which demonstrates the applicability of the "W"-QW design as gain medium in a laser [134].

On this basis, a prototype of a type-II VECSEL was designed and realized. Different samples were flip-chip bonded and investigated. As in the previous chapters, the detuning studies were performed which yield a complete picture of the sample's capabilities. With all three samples lasing could be demonstrated and, remarkably, output powers at Watt level could be achieved. Their different performance and emission wavelengths can be explained by the results from the detuning studies. For instance, sample 6.3 exhibits an LCF maximum of only 2, which reduces the possible modal gain. Concerning the amplitude of the LCF, sample 6.4 is clearly improved, but the LCF peak is placed close to the edge of the stop band. It is likely that a reduced reflectivity is present at this location, which may introduce significant reflection losses. Sample 6.5 exhibits an ideal LCF amplitude, but does not operate in a linear cavity. This sample was used to demonstrate the significance of the detuning. Instead of a negative detuning in type-I VECSELs, a positive detuning is required to compensate for the blue shift of the material gain. In contrast to sample 6.4, samples 6.3 and 6.5 exhibit an emission wavelength even beyond 1200 nm which cannot be accessed with the conventional (GaIn)As/GaAs design. This is a first indication of the wavelength capabilities of type-II VECSELs which arise from slight modifications of the QW design. The results obtained with sample 6.4 can also be found in [135].

To demonstrate the applicability of type-II VECSELs for mode-locking, frequency-conversion, or single-frequency operation, sample 6.4 was chosen to investigate the performance in TEM_{00} operation. Output powers as high as 350 mW were observed with an excellent beam profile and an $M^2 < 1.2$. In the future these results can be improved with an optimized type-II VECSEL structure.

The investigations show that the performance of the type-II VECSEL can be significantly enhanced if a sample could be realized with

- an LCF maximum of 4 and which is located at the center of the stop band and
- with a positive detuning in a range between 18 nm to 37 nm.

The suggested range is based on the studies with sample 6.4 in a linear cavity, with a detuning of $+ 33 \pm 4$ nm, and with sample 6.5, which showed the best performance at an angle of 45° with the detuning of $+ 25 \pm 8$ nm. It can be anticipated that a chip with these optimizations enables Watt level output powers at room temperature while the pump spot diameter can be further reduced. The improved modal gain will facilitate the introduction of intra-cavity elements, such as saturable absorber mirrors for mode-locking, nonlinear crystals for frequency-doubling into the visible regime, or birefringent filters for single-frequency operation. Indeed, with regard to type-I VECSELs at 1180 nm, the performance of the type-II VECSEL is inferior, but this should reverse beyond 1.2 µm. It is predicted by a microscopic theory, that slight modifications of the "W"-QW design studied here, can yield a similar gain amplitude at 1.3 µm [131]. The feasibility of the MOVPE growth of such "W"-QWs was already demonstrated [132]. Taking into account, that the quantum defect and thermal resistance are increasing with the laser wavelength, an optimized type-II VECSEL may still deliver Watt level output powers at a wavelength of 1.3 µm and beyond.

7. Summary and outlook

Novel material systems and quantum well (QW) structures are one of the key elements of VECSEL research to increase the available performance and wavelength range to a broader range of applications. This thesis summarizes experimental investigations on different QW designs for use as gain medium in barrier-pumped GaAs-based vertical-external-cavity surface-emitting lasers (VECSELs). The applied experimental methods are introduced in chapter 3. Not only basic parameters are acquired, such as threshold densities, slope efficiencies and output powers. More important in context of a detailed device analysis are more hidden parameters. In resonant VECSELs, as are studied in this thesis, the detuning is one of these important parameters. It is demonstrated that a combination of temperature dependent reflectance (TDR) and edge photoluminescence (PL) measurements as well as transfer-matrix calculations can be used to determine the detuning accurately. Moreover, a new setup for gain measurements is proposed and realized. This kind of setup can be used to explore the pump power dependent evolution of the modal gain of VECSEL chips at various wavelengths. A power limiting factor in VECSELs is also the thermal resistance. Three different measurement techniques are summarized and discussed. An important outcome of these measurements is particularly the gain temperature, which can be specified in dependence on heat sink temperature and pump power. Overall, the combination of all measurements yields a complete picture of a VECSEL and can be used to identify and explain performance limitations, which can have manifold reasons, such as a poor chip quality, an unfavorable detuning, a poor thermal resistance, or, if these factors can be excluded, a weak material gain. Chapter 3 does not only introduce these experimental methods, but also demonstrates the methods by means of a well-established sample at 1 µm emission wavelength. Consequently, a complete experimental study is provided for this sample, which serves as a reference for comparisons with other chips.

Chapter 4 is dedicated to the impact of the detuning on the device performance. A V-cavity arrangement with the VECSEL chip as folding mirror is suggested and verified to manipulate the sample's detuning by altering the cavity angle. An increase of the folding angle results in a blue shift of the micro-cavity resonance. This can be understood in terms of a simple model which considers the phase of a plane wave reflected from a Fabry–Pérot etalon. However, using transfer-matrix calculations, it can be shown that this simple model yields an accurate approximation of the angle dependent micro-cavity shift. Due to the blue shift of the longitudinal confinement factor (LCF) with an increase of the cavity angle, a sample with relatively large negative detuning is required for the detuning studies. With such sample, the negative detuning can be decreased by an increase of the cavity angle. A large negative detuning is presumably found in high-power VECSELs, because it should delay the thermal roll-over. Such high-power sample (sample 4.1), which was recently used for the demonstration of 23 W single-frequency operation, is studied to determine and confirm the large negative detuning of -40 nm. It is found that the threshold densities, output powers, and emission wavelengths can be greatly altered by the manipulation of the detuning. While the detuning is changed from -37 nm to -20 nm, the thresholds are decreased by a factor of about 2.5. In contrast, the maximum output power is decreased by a factor of two. Also the emission wavelength is greatly affected, but which gives access to a great tunability from 1016 nm to 1051 nm. The results are also consistent with the reference sample, which exhibits a detuning of -14 nm and an even lower threshold. As a conclusion, the reference sample can be seen as "low threshold" device, while the sample 4.1 is in fact optimized for high output powers. However, the investigated range of detuning was limited by the applicable angle. To expand the

range and investigate even smaller, or larger detuning, further samples could be investigated in the future. The respective "optimal" detunings for lowest thresholds or highest output powers could be identified. For instance, the reference sample could be used to explore detunings from -14 nm to ~5 nm. A sample with a detuning of -60 nm could be used to explore the ideal detuning for high-power operation. In future studies, also VECSELs based on other gain materials could be investigated. An example is carried out in chapter 6 with the type-II VECSEL. Additionally, it could be interesting to investigate the detuning dependences of quantum dot VECSELs.

In chapter 5, VECSELs for the emission between 920 nm – 950 nm are studied. In contrast to barrier-pumped VECSELs at higher wavelength, such as 1 µm and beyond, the QW depth is of concern. Applying a similar QW design, as studied in chapters 3 – 4, to a wavelength of 920 nm – 930 nm by only adapting the indium content, would result in conduction band and valance band offset (CBO, VBO) energies in the order of magnitude of k_bT at room temperature. According to the quasi-Fermi distribution, a significant amount of carriers could thermally escape from such shallow quantum wells. To avoid that, an alternative design with thin Ga(AsP) barriers is investigated. At the same time, the regular QW design from chapters 3 and 4 is used for a VECSEL with 950 nm emission wavelength. It is discussed, that the 920 nm – 930 nm VECSELs and the 950 nm VECSEL should exhibit very similar CBOs and VBOs. Accordingly, a very similar performance is expected from these different devices. However, an interesting result is, that decent laser operation can only be demonstrated with the 950 nm VECSEL. The striking difference between the samples is demonstrated by their different output powers: while 35 W can be obtained from the 950 nm sample, only 500 mW are observed for the 930 nm sample. However, the detailed studies, in accordance with chapter 3, show that this is not a matter of the chip quality, or thermal resistance. Moreover, the amplitude of the LCF and the detuning are even better for the 920 nm – 930 nm samples in comparison with the 950 nm sample. As a conclusion, the material gain of the 920 – 930 nm samples must be significantly reduced in comparison with the 950 nm sample and the reference sample at 1 µm, respectively. The evolution of the pump intensity dependent gain measurements show a very weak bleaching of the 920 – 930 nm QWs, which could be related to a poor capture of the charge carriers from the barriers. To investigate this, time resolved pump and probe measurements could be performed on the different QW designs in the future. In this way, the time constants for the carrier capture could be identified and compared to the QW ground state life-times. Also, alternative QW designs can be studied in order to investigate the influence of the barriers. One possibility is to arrange the Ga(AsP) strain compensating layers in the center of the QW (AlGa)As separation layers, which then also serve as barriers. Due to the low indium concentration and strain, the number of QWs can also be significantly increased to increase the material gain. However, an important result of chapter 5 is also, that the 950 nm VECSEL can be significantly improved. The investigated sample is not perfectly resonant, i.e. the LCF only exhibits an amplitude of 2 instead of the ideal value of 4. This optimization doubles the modal gain which should also suppress the observed lateral lasing. Consequently, the output powers and thresholds should be significantly enhanced.

The last part of the thesis, chapter 6, deals with the concept of type-II QWs. The (GaIn)As/Ga(AsSb)/(GaIn)As "W"-QW design, modeled by a microscopic theory for the emission at about 1.2 µm, is investigated in PL studies. The radiative type-II transition is confirmed by a comparison of the constituting single quantum wells (SQWs) and the "W"-QW PL. Power dependent PL measurements also indicate a carrier density dependent blue shift of the emission wavelength. It is discussed that this effect is important for the realization of a type-II VECSEL, as it determines the required detuning. Taking up the PL investigations, three VECSEL samples are realized and investigated in accordance to chapter 3. Two samples operate in a linear cavity and

first laser operation of a type-II VECSEL is demonstrated. The difference in the performance of these samples, one with an output power of 1.2 W, the other one with a remarkable power of 4 W, can be related to the amplitudes of the different LCFs. A comparison between the laser emission wavelength and the detuning studies, i.e. the peak wavelength of the LCF and the PL, reveals, that there is a significant blue shift of the material gain prior to the achievement of the laser threshold. For the two mentioned samples, detunings of > + 30 nm are determined, which is entirely different from which is required for type-I VECSELs. Moreover, one of the samples is exploited for a detailed investigation of the laser properties. It is found that the laser wavelength exhibits a red shift which depends linearly on pump power and heat sink temperature. On this basis, the thermal resistance is determined which also reveals the gain temperatures. The low rise of the gain temperature at the laser threshold suggests that the present detuning is already close to an optimum for the investigated QW design. This is also confirmed with the V-cavity experiment. The detuning of the third type-II sample is close to zero in a linear cavity, where no laser operation is observed. However, the detuning is increased in a V-cavity and with the chip as a folding mirror as demonstrated in chapter 4. Lasing can be achieved at an angle of 15° and, furthermore, the performance is greatly enhanced with the 30° and 45° angles. At the 45° angle, however, the detuning is again close to the detuning of the other samples in a linear cavity. As last studies, also the transverse mode properties of the type-II VECSEL are studied. In multimode operation, it is demonstrated that the roll-over behavior is not different from type-I VECSELs, i.e. the power from the center is depleted first, followed by the outer areas. Thus, the roll-over behavior is also closely related to the heat distribution which is dictated by the pump spot profile. In TEM_{00} operation, an output power of up to 350 mW is observed with an M^2 of < 1.2.

In the future, an optimized type-II VECSEL can be manufactured as suggested in chapter 6. Such an optimized device should exhibit an improved modal gain and higher output powers which is important for future applications. For instance, the use of an intra-cavity birefringent filter, nonlinear crystal, or semiconductor SAM for single-frequency operation, frequency-conversion, or mode-locked operation involves inherent intra-cavity losses which must be compensated. Still, the investigation of these fields with a type-II VECSEL is of great interest. Moreover, the results suggest that efficient VECSELs can be realized at emission wavelengths even beyond 1.3 µm. As mentioned, it is predicted, that the increase of the emission wavelength is not at a cost of the material gain in this versatile QW design.

Bibliography

[1] T. H. Maiman, "Stimulated Optical Radiation in Ruby," *Nature*, vol. 187, no. 4736, pp. 493–494, 1960.

[2] A. Javan, W. R. Bennett, and D. R. Herriott, "Population inversion and continuous optical maser oscillation in a gas discharge containing a He-Ne mixture," *Phys. Rev. Lett.*, vol. 6, no. 3, 1961.

[3] Z. I. Alferov, "Nobel Lecture: The double heterostructure concept and its applications in physics, electronics, and technology," *Rev. Mod. Phys.*, vol. 73, no. 3, p. 767, 2001.

[4] J. P. Van der Ziel, R. Dingle, R. C. Miller, W. Wiegmann, and W. A. Nordland, "Laser oscillation from quantum states in very thin GaAs−$Al_{0.2}Ga_{0.8}As$ multilayer structures," *Appl. Phys. Lett.*, vol. 26, no. 8, p. 463, 1975.

[5] W. T. Tsang, C. Weisbuch, R. C. Miller, and R. Dingle, "Current injection GaAs-$Al_xGa_{1-x}As$ multi-quantum-well heterostructure lasers prepared by molecular beam epitaxy," *Appl. Phys. Lett.*, vol. 35, no. 9, p. 673, 1979.

[6] M. Grabherr, "New applications boost VCSEL quantities: recent developments at Philips," presented at the SPIE Photonics West: Vertical-cavity surface-emitting lasers XIX, San Francisco, USA, 2015, p. 938102.

[7] J. A. Tatum, "Evolution of VCSELs," presented at the SPIE Photonics West: Vertical-cavity surface-emitting lasers XVIII, San Francisco, USA, 2014, p. 90010C.

[8] O. G. Okhotnikov, *Semiconductor Disk Lasers: Physics and Technology*. Wiley-VCH, 2009.

[9] A. Rahimi-Iman, "Recent advances in VECSELs," *J. Opt.*, vol. 18, no. 9, p. 93003, 2016.

[10] M. Kuznetsov, F. Hakimi, R. Sprague, and A. Mooradian, "High-power (> 0.5-W CW) diode-pumped vertical-external-cavity surface-emitting semiconductor lasers with circular TEM_{00} beams," *IEEE Photon. Technol. Lett.*, vol. 9, no. 8, pp. 1063–1065, 1997.

[11] A. C. Tropper and S. Hoogland, "Extended cavity surface-emitting semiconductor lasers," *Prog. Quantum Eletron.*, vol. 30, no. 1, pp. 1–43, 2006.

[12] U. Keller and A. C. Tropper, "Passively modelocked surface-emitting semiconductor lasers," *Phys. Rep.*, vol. 429, no. 2, pp. 67–120, 2006.

[13] S. Calvez, J. E. Hastie, M. Guina, O. G. Okhotnikov, and M. D. Dawson, "Semiconductor disk lasers for the generation of visible and ultraviolet radiation," *Laser Photon. Rev.*, vol. 3, no. 5, pp. 407–434, 2009.

[14] M. A. Gaafar, A. Rahimi-Iman, K. A. Fedorova, W. Stolz, E. U. Rafailov, and M. Koch, "Mode-locked semiconductor disk lasers," *Adv. Opt. Photonics*, vol. 8, no. 3, p. 370, 2016.

[15] K.-S. Kim *et al.*, "920-nm Vertical-External-Cavity Surface-Emitting Lasers With a Slope Efficiency of 58% at Room Temperature," *IEEE Photon. Technol. Lett.*, vol. 19, no. 20, pp. 1655–1657, 2007.

[16] M. Schmid, S. Benchabane, F. Torabi-Goudarzi, R. Abram, A. I. Ferguson, and E. Riis, "Optical in-well pumping of a vertical-external-cavity surface-emitting laser," *Appl. Phys. Lett.*, vol. 84, no. 24, p. 4860, 2004.

[17] N. Schulz *et al.*, "Resonant optical in-well pumping of an (AlGaIn)(AsSb)-based vertical-external-cavity surface-emitting laser emitting at 2.35 µm," *Appl. Phys. Lett.*, vol. 91, no. 9, p. 91113, 2007.

[18] T. Wunderer *et al.*, “In-well pumping of InGaN/GaN vertical-external-cavity surface-emitting lasers,” *Appl. Phys. Lett.*, vol. 99, no. 20, p. 201109, 2011.

[19] E. Kantola, T. Leinonen, S. Ranta, M. Tavast, J.-P. Penttinen, and M. Guina, “1180nm VECSEL with 50 W output power,” presented at the SPIE Photonics West: Vertical-external-cavity surface-emitting lasers V, San Francisco, USA, 2015, p. 93490U.

[20] B. Heinen *et al.*, “106 W continuous wave output power from a vertical-external-cavity surface-emitting laser (VECSEL),” *Electron. Lett.*, vol. 48, no. 9, p. 516, 2012.

[21] T.-L. Wang *et al.*, “Quantum design strategy pushes high-power vertical-external-cavity surface-emitting lasers beyond 100 W,” *Laser Photonics Rev.*, vol. 6, no. 5, pp. L12–L14, 2012.

[22] Verdi Series, Coherent Inc., https://coherent.com/products/index. cfm?1851/Verdi-G-Series, last access on 10/21/2016.

[23] E. Kantola, T. Leinonen, S. Ranta, M. Tavast, and M. Guina, “High-efficiency 20 W yellow VECSEL,” *Opt. Express*, vol. 22, no. 6, p. 6372, 2014.

[24] L. A. Coldren, S. W. Corzine, and M. L. Masanovic, *Diode Lasers and Photonic Integrated Circuits*, 2nd ed. John Wiley & Sons, 2012.

[25] P. S. Zory, *Quantum Well Lasers*. Academic Press, 1993.

[26] B. E. A. Saleh and M. C. Teich, *Fundamentals of photonics*. Wiley-Interscience, 2007.

[27] I. Vurgaftman, J. R. Meyer, and L. R. Ram-Mohan, “Band parameters for III–V compound semiconductors and their alloys,” *J. Appl. Phys.*, vol. 89, no. 11, p. 5815, 2001.

[28] S. Hasegawa, A. Tanaka, and T. Sukegawa, “Optical-absorption coefficient near the fundamental absorption edge of GaAsP,” *J. Appl. Phys.*, vol. 55, no. 8, p. 3188, 1984.

[29] A. R. Zakharian, J. Hader, J. V. Moloney, S. W. Koch, P. Brick, and S. Lutgen, “Experimental and theoretical analysis of optically pumped semiconductor disk lasers,” *Appl. Phys. Lett.*, vol. 83, no. 7, p. 1313, 2003.

[30] J. V. Moloney, J. Hader, L. Fan, M. Fallahi, S. W. Koch, and W. Stolz, “Closed-loop design of a semiconductor laser,” presented at the SPIE Photonics West: Integrated Optics: Devices, Materials, and Technologies XI, San Jose, USA, 2007, p. 64750M–14.

[31] S. W. Koch, J. Hader, and J. V. Moloney, “Microscopic VECSEL modeling,” presented at the SPIE Photonics West: Vertical-external-cavity surface-emitting lasers IV, San Francisco, USA, 2014, p. 896603.

[32] J. Hader *et al.*, “Predictive Microscopic Modeling of VECSELs,” *IEEE J. Quantum Electron.*, vol. 46, no. 5, pp. 810–817, 2010.

[33] A. R. Zakharian, J. Hader, J. V. Moloney, and S. W. Koch, “VECSEL threshold and output power-shutoff dependence on the carrier recombination rates,” *IEEE Photon. Technol. Lett.*, vol. 17, no. 12, pp. 2511–2513, 2005.

[34] D. Waldburger *et al.*, “High-power 100 fs semiconductor disk lasers,” *Optica*, vol. 3, no. 8, p. 844, 2016.

[35] S. Sprengel, A. Andrejew, F. Federer, G. K. Veerabathran, G. Boehm, and M.-C. Amann, “Continuous wave vertical cavity surface emitting lasers at 2.5 μm with InP-based type-II quantum wells,” *Appl. Phys. Lett.*, vol. 106, no. 15, p. 151102, 2015.

[36] S. Kaspar *et al.*, “Linewidth Narrowing and Power Scaling of Single-Frequency 2.X μm GaSb-Based Semiconductor Disk Lasers,” *IEEE J. Quantum Electron.*, vol. 49, no. 3, pp. 314–324, 2013.

[37] D. Al Nakdali *et al.*, “Analysis of optical scattering losses in vertical-external-cavity surface-emitting lasers,” *Appl. Phys. B*, vol. 120, no. 1, pp. 41–46, 2015.

[38] D. Al Nakdali *et al.*, “High-Power Operation of Quantum-Dot Semiconductor Disk Laser at 1180 nm,” *IEEE Photon. Technol. Lett.*, vol. 27, no. 10, pp. 1128–1131, 2015.

[39] M. Butkus *et al.*, “High-power quantum-dot-based semiconductor disk laser,” *Opt. Lett.*, vol. 34, no. 11, pp. 1672–1674, 2009.

[40] J. Hader *et al.*, “On the measurement of the thermal impedance in vertical-external-cavity surface-emitting lasers,” *J. Appl. Phys.*, vol. 113, no. 15, p. 153102, 2013.

[41] T.-L. Wang *et al.*, “Strategies for power scaling VECSELs,” presented at the SPIE Photonics West: Vertical-external-cavity surface-emitting lasers II, San Francisco, USA, 2012, p. 824209.

[42] A. J. Kemp *et al.*, “Heatspreader-Based Thermal Management in VECSELs: Thermal Lensing in Microchip Devices,” presented at the OSA Conference on Advanced Solid-State Photonics, Vienna, AUT, 2005, p. MB34.

[43] B. Heinen, F. Zhang, M. Sparenberg, B. Kunert, M. Koch, and W. Stolz, “On the Measurement of the Thermal Resistance of Vertical-External-Cavity Surface-Emitting Lasers (VECSELs),” *IEEE J. Quantum Electron.*, vol. 48, no. 7, pp. 934–940, 2012.

[44] B. Heinen, C. Möller, K. Jandieri, B. Kunert, M. Koch, and W. Stolz, “The Thermal Resistance of High-Power Semiconductor Disk Lasers,” *IEEE J. Quantum Electron.*, vol. 51, no. 5, pp. 1–9, 2015.

[45] A. J. Maclean, R. B. Birch, P. W. Roth, A. J. Kemp, and D. Burns, “Limits on efficiency and power scaling in semiconductor disk lasers with diamond heatspreaders,” *J. Opt. Soc. Am. B*, vol. 26, no. 12, pp. 2228–2236, 2009.

[46] K. Pierscinski, D. Pierscinska, M. Bugajski, C. Manz, and M. Rattunde, “Influence of the intracavity heatspreader on the VECSEL temperature,” presented at the Int. Conference on Mixed Design of Integrated Circuits and Systems, Lodz, Poland, 2009, pp. 355–360.

[47] W. Xie, Y. Kwon, W. Hu, and F. Zhou, “Thermal modeling of solid state lasers with super-Gaussian pumping profiles,” *Opt. Eng.*, vol. 42, no. 6, pp. 1787–1794, 2003.

[48] H. Nadgaran and P. Elahi, “The analytical investigation of the super-Gaussian pump source on the thermal, stress and thermo-optics properties of double-clad Yb:glass fiber lasers,” *Pramana*, vol. 65, no. 1, pp. 95–105, 2005.

[49] H. Lindberg, M. Strassner, E. Gerster, J. Bengtsson, and A. Larsson, “Thermal management of optically pumped long-wavelength InP-based semiconductor disk lasers,” *IEEE J. Sel. Top. Quantum Elec.*, vol. 11, no. 5, pp. 1126–1134, 2005.

[50] I. A. Bronstein, K. A. Semendjajew, G. Musiol, and H. Mühlig, *Taschenbuch der Mathematik*, 6th ed. 2005.

[51] A. Chernikov *et al.*, “Influence of the spatial pump distribution on the performance of high power vertical-external-cavity surface-emitting lasers,” *Appl. Phys. Lett.*, vol. 97, no. 19, p. 191110, 2010.

[52] O. Svelto and D. C. Hanna, *Principles of lasers*, 4th ed. Plenum Press, 1998.

[53] S. Hoogland *et al.*, “Passively mode-locked diode-pumped surface-emitting semiconductor laser,” *IEEE Photon. Technol. Lett.*, vol. 12, no. 9, pp. 1135–1137, 2000.

[54] K. G. Wilcox *et al.*, “4.35 kW peak power femtosecond pulse mode-locked VECSEL for supercontinuum generation,” *Opt. Express*, vol. 21, no. 2, pp. 1599–1605, 2013.

[55] A. Laurain *et al.*, “Colliding pulse mode locking of vertical-external-cavity surface-emitting laser,” *Optica*, vol. 3, no. 7, p. 781, 2016.

[56] L. Kornaszewski, G. Maker, G. P. A. Malcolm, M. Butkus, E. U. Rafailov, and C. J. Hamilton, "SESAM-free mode-locked semiconductor disk laser," *Laser Photon. Rev.*, vol. 6, no. 6, pp. L20–L23, 2012.

[57] Y. F. Chen, Y. C. Lee, H. C. Liang, K. Y. Lin, K. W. Su, and K. F. Huang, "Femtosecond high-power spontaneous mode-locked operation in vertical-external cavity surface-emitting laser with gigahertz oscillation," *Opt. Lett.*, vol. 36, no. 23, pp. 4581–4583, 2011.

[58] M. Gaafar *et al.*, "Harmonic self-mode-locking of optically pumped semiconductor disc laser," *Electron. Lett.*, vol. 50, no. 7, p. 551, 2014.

[59] A. R. Albrecht, Y. Wang, M. Ghasemkhani, D. V. Seletskiy, J. G. Cederberg, and M. Sheik-Bahae, "Exploring ultrafast negative Kerr effect for mode-locking vertical external-cavity surface-emitting lasers," *Opt. Express*, vol. 21, no. 23, p. 28801, 2013.

[60] M. Gaafar *et al.*, "Self-mode-locking semiconductor disk laser," *Opt. Express*, vol. 22, no. 23, p. 28390, 2014.

[61] C. H. Tsou, H. C. Liang, C. P. Wen, K. W. Su, K. F. Huang, and Y. F. Chen, "Exploring the influence of high order transverse modes on the temporal dynamics in an optically pumped mode-locked semiconductor disk laser," *Opt. Express*, vol. 23, no. 12, p. 16339, 2015.

[62] A. Rantamaki, A. Chamorovskiy, J. Lyytikainen, and O. Okhotnikov, "4.6-W Single Frequency Semiconductor Disk Laser With 75-kHz Linewidth," *IEEE Photon. Technol. Lett.*, vol. 24, no. 16, pp. 1378–1380, 2012.

[63] F. Zhang *et al.*, "A 23-watt single-frequency vertical-external-cavity surface-emitting laser," *Opt. Express*, vol. 22, no. 11, p. 12817, 2014.

[64] T. Kim *et al.*, "2 W continuous wave operation of optically pumped blue VECSEL with frequency doubling," presented at the SPIE Photonics West: Vertical-external-cavity surface-emitting lasers X, 2006, p. 61320K.

[65] H. Kahle, R. Bek, M. Heldmaier, T. Schwarzbäck, M. Jetter, and P. Michler, "High optical output power in the UVA range of a frequency-doubled, strain-compensated AlGaInP-VECSEL," *Appl. Phy. Express*, vol. 7, no. 9, p. 92705, 2014.

[66] M. Scheller, J. M. Yarborough, J. V. Moloney, M. Fallahi, M. Koch, and S. W. Koch, "Room temperature continuous wave milliwatt terahertz source," *Opt. Express*, vol. 18, no. 26, pp. 27112–27117, 2010.

[67] Y. P. Varshni, "Temperature dependence of the energy gap in semiconductors," *Physica*, vol. 34, no. 1, pp. 149–154, 1967.

[68] K. L. Shaklee, "Direct determination of optical gain in semiconductor crystals," *Appl. Phys. Lett.*, vol. 18, no. 11, p. 475, 1971.

[69] K. L. Shaklee, R. E. Nahory, and R. F. Leheny, "Optical gain in semiconductors," *J. Lumin.*, vol. 7, pp. 284–309, 1973.

[70] B. W. Hakki, "cw degradation at 300°K of GaAs double-heterostructure junction lasers. II. Electronic gain," *J. Appl. Phys.*, vol. 44, no. 9, p. 4113, 1973.

[71] B. W. Hakki and T. L. Paoli, "Gain spectra in GaAs double−heterostructure injection lasers," *J. Appl. Phys.*, vol. 46, no. 3, p. 1299, 1975.

[72] D. T. Cassidy, "Technique for measurement of the gain spectra of semiconductor diode lasers," *J. Appl. Phys.*, vol. 56, no. 11, p. 3096, 1984.

[73] C. Ellmers *et al.*, "Measurement and calculation of gain spectra for (GaIn)As/(AlGa)As single quantum well lasers," *Appl. Phys. Lett.*, vol. 72, no. 13, p. 1647, 1998.

[74] M.-L. Ma *et al.*, "Measurement of gain characteristics of semiconductor lasers by amplified spontaneous emissions from dual facets," *Opt. Express*, vol. 21, no. 8, p. 10335, 2013.

[75] S. Haupt, M. Furitsch, H. Lindberg, I. Pietzonka, U. Strauss, and G. Bacher, "Measurement of Gain and Device Performance of a 1050-nm Vertical External Cavity Surface Emitting Laser," *IEEE J. Quantum Electron.*, vol. 49, no. 3, pp. 380–385, 2013.

[76] C. Borgentun, J. Bengtsson, and A. Larsson, "Direct measurement of the spectral reflectance of OP-SDL gain elements under optical pumping," *Optics Express*, vol. 19, no. 18, pp. 16890–16897, 2011.

[77] C. R. Head, K. G. Wilcox, A. P. Turnbull, O. J. Morris, E. A. Shaw, and A. C. Tropper, "Saturated gain spectrum of VECSELs determined by transient measurement of lasing onset," *Opt. Express*, vol. 22, no. 6, p. 6919, 2014.

[78] M. Mangold *et al.*, "VECSEL gain characterization," *Opt. Express*, vol. 20, no. 4, pp. 4136–4148, 2012.

[79] C. Lammers *et al.*, "Gain spectroscopy of a type-II VECSEL chip," *arXiv preprint arXiv:1608.05250*, Appl. Phys. Lett., accepted 2016.

[80] A. Kalinger, "Charakterisierung des optischen Gewinns von Halbleiter-Scheibenlasern," Master Thesis, Philipps-Universität Marburg, 2016.

[81] E. Kühn, A. Thränhardt, C. Bückers, S. W. Koch, J. Hader, and J. V. Moloney, "Numerical study of the influence of an antireflection coating on the operating properties of vertical-external-cavity surface-emitting lasers," *Journal of Applied Physics*, vol. 106, no. 6, p. 63105, 2009.

[82] A. J. Kemp *et al.*, "Thermal Management in 2.3-µm Semiconductor Disk Lasers: A Finite Element Analysis," *IEEE J. Quantum Elec.*, vol. 44, no. 2, pp. 125–135, 2008.

[83] D. Burns *et al.*, "Recent developments in high-power short-wave mid-infrared semiconductor disk lasers," presented at the SPIE Photonics West: Solid State Lasers XVIII: Technology and Devices, San Jose, CA, USA, 2009, pp. 719311–13.

[84] T. Schwarzbäck, M. Eichfelder, W.-M. Schulz, R. Roßbach, M. Jetter, and P. Michler, "Short wavelength red-emitting AlGaInP-VECSEL exceeds 1.2 W continuous-wave output power," *Appl. Phys. B*, vol. 102, no. 4, pp. 789–794, 2011.

[85] E. Hecht, *Optik*. Addison-Wesley, 1989.

[86] M. A. Afromowitz, "Thermal conductivity of $Ga_{1-x}Al_x$ As alloys," *J. Appl. Phys.*, vol. 44, no. 3, p. 1292, 1973.

[87] B. Heinen, *Wärmetransport in optisch gepumpten Hochleistungs-Halbleiter-Scheibenlasern*, 1st ed. Göttingen: Cuvillier Verlag, 2014.

[88] A. Pourhashemi, R. M. Farrell, D. A. Cohen, J. S. Speck, S. P. DenBaars, and S. Nakamura, "High-power blue laser diodes with indium tin oxide cladding on semipolar (2021) GaN substrates," *Appl. Phys. Lett.*, vol. 106, no. 11, p. 111105, 2015.

[89] J.-Y. Kim *et al.*, "Efficient blue lasers based on gain structure optimizing of vertical-external-cavity surface-emitting laser with second harmonic generation," *J. Appl. Phys.*, vol. 101, no. 3, p. 33103, 2007.

[90] F. Schill, U. R. Zimmer, and J. Trumpf, "Visible spectrum optical communication and distance sensing for underwater applications," presented at the Australian Conference on Robotics and Automation, Canberra, AUS, 2004, pp. 1–8.

[91] E. T. Yu, J. O. McCaldin, and T. C. McGill, *Solid State Physics*. San Diego: Academic Press, 1992.

[92] T. G. Andersson, Z. G. Chen, V. D. Kulakovskii, A. Uddin, and J. T. Vallin, "Photoluminescence and photoconductivity measurements on band-edge offsets in strained molecular-beam-epitaxy-grown InGaAs/GaAs quantum wells," *Phys. Rev. B*, vol. 37, no. 8, p. 4032, 1988.

[93] L. P. Ramberg *et al.*, "Lattice-strained heterojunction InGaAs/GaAs bipolar structures: Recombination properties and device performance," *J. Appl. Phys.*, vol. 61, no. 3, p. 1234, 1987.

[94] K. F. Huang, K. Tai, S. N. G. Chu, and A. Y. Cho, "Optical studies of InGaAs/GaAs strained-layer quantum wells," *Appl. Phys. Lett.*, vol. 54, no. 20, p. 2026, 1989.

[95] J.-P. Reithmaier, R. Höger, H. Riechert, A. Heberle, G. Abstreiter, and G. Weimann, "Band offset in elastically strained InGaAs/GaAs multiple quantum wells determined by optical absorption and electronic Raman scattering," *Appl. Phys. Lett.*, vol. 56, no. 6, p. 536, 1990.

[96] Y. Zou *et al.*, "Characterization and determination of the band-gap discontinuity of the InGaAs/GaAs pseudomorphic quantum well," *Appl. Phys. Lett.*, vol. 58, no. 6, p. 601, 1991.

[97] S. Niki, C. L. Lin, W. S. C. Chang, and H. H. Wieder, "Band-edge discontinuities of strained-layer InGaAs/GaAs heterojunctions and quantum wells," *Appl. Phys. Lett.*, vol. 55, no. 13, p. 1339, 1989.

[98] S.-H. Pan *et al.*, "Photoreflectance study of narrow-well strained-layer InGaAs/GaAs coupled multiple-quantum-well structures," *Phys. Rev. B*, vol. 38, no. 5, p. 3375, 1988.

[99] Y. Zhang *et al.*, "Design and comparison of GaAs, GaAsP and InGaAlAs quantum-well active regions for 808-nm VCSELs," *Opt. Express*, vol. 19, no. 13, pp. 12569–12581, 2011.

[100] G. Bacher *et al.*, "Influence of barrier height on carrier dynamics in strained In_x Ga_{1-x} As/GaAs quantum wells," *Physical Review B*, vol. 43, no. 11, p. 9312, 1991.

[101] G. Bacher, C. Hartmann, H. Schweizer, T. Held, G. Mahler, and H. Nickel, "Exciton dynamics in InGaAs/GaAs quantum-well heterostructures: Competition between capture and thermal emission," *Phys. Rev. B*, vol. 47, no. 15, pp. 9545–9555, 1993.

[102] M. Vening, D. J. Dunstan, and K. P. Homewood, "Thermal quenching and retrapping effects in the photoluminescence of $In_yGa_{1-y}As/GaAs/Al_xGa_{1-x}As$ multiple-quantum-well structures," *Phys. Rev. B*, vol. 48, no. 4, p. 2412, 1993.

[103] A. P. Ongstad, M. L. Tilton, E. J. Bochove, and G. C. Dente, "Carrier spillover at 300, 195, and 77 K in InGaAs and GaAs single quantum wells," *J. Appl. Phys.*, vol. 80, no. 5, p. 2866, 1996.

[104] J. Hader *et al.*, "VECSEL Optimization Using Microscopic Many-Body Physics," *IEEE J. Sel. Top. Quantum Elec.*, vol. 17, no. 6, pp. 1753–1762, 2011.

[105] C. Hessenius, M. Fallahi, J. Moloney, and R. Bedford, "Lateral lasing and ASE reduction in VECSELs," presented at the SPIE Photonics West: Vertical-external cavity surface emitting lasers, San Francisco, USA, 2011, p. 791909.

[106] T. Töpper *et al.*, "High-power 2.0 µm semiconductor disk laser—Influence of lateral lasing," *Appl. Phys. Lett.*, vol. 100, no. 19, p. 192107, 2012.

[107] J. Hader, J. V. Moloney, S. W. Koch, and W. W. Chow, "Microscopic modeling of gain and luminescence in semiconductors," *IEEE J. Select. Topics Quantum Electron.*, vol. 9, no. 3, pp. 688–697, 2003.

[108] K.-S. Kim, Y.-H. Cho, B.-D. Choe, W. G. Jeong, and H. Lim, "Determination of Al mole fraction for null conduction band offset in $In_{0.5}Ga_{0.5}P/Al_xGa_{1-x}As$ heterojunction by photoluminescence measurement," *Appl. Phys. Lett.*, vol. 67, no. 12, p. 1718, 1995.

[109] D. Schlenker, T. Miyamoto, Z. Chen, F. Koyama, and K. Iga, "Growth of highly strained GaInAs/GaAs quantum wells for 1.2 µm wavelength lasers," *J. Cryst. Growth*, vol. 209, no. 1, pp. 27–36, 2000.

[110] E. Murphy, "The semiconductor laser: Enabling optical communication," *Nat. Photon.*, vol. 4, no. 5, pp. 287–287, 2010.

[111] G. P. Agrawal, *Fiber-Optic Communication Systems*, vol. 222. John Wiley & Sons, 2012.

[112] J. A. Zuclich, D. J. Lund, and B. E. Stuck, “Wavelength dependence of ocular damage thresholds in the near-IR to far-IR transition region: Proposed revisions to MPEs,” *Health Phys.*, vol. 92, no. 1, pp. 15–23, 2007.

[113] A. R. Albrecht *et al.*, “Multi-watt 1.25 μm quantum dot VECSEL,” *Electron. Lett.*, vol. 46, no. 12, pp. 856–857, 2010.

[114] V.-M. Korpijarvi, E. L. Kantola, T. Leinonen, R. Isoaho, and M. Guina, “Monolithic GaInNAsSb/GaAs VECSEL Operating at 1550 nm,” *IEEE J. Sel. Top. Quantum Electron.*, vol. 21, no. 6, pp. 480–484, 2015.

[115] S. T. Keller, A. Sirbu, V. Iakovlev, A. Caliman, A. Mereuta, and E. Kapon, “8.5 W VECSEL output at 1270 nm with conversion efficiency of 59 %,” *Opt. Express*, vol. 23, no. 13, p. 17437, 2015.

[116] A. Rantamäki, J. Rautiainen, A. Sirbu, A. Mereuta, E. Kapon, and O. G. Okhotnikov, “1.56 μm 1 watt single frequency semiconductor disk laser,” *Opt. Express*, vol. 21, no. 2, pp. 2355–2360, 2013.

[117] J. R. Meyer, C. A. Hoffman, F. J. Bartoli, and L. R. Ram-Mohan, “Type-II quantum-well lasers for the mid-wavelength infrared,” *Appl. Phys. Lett.*, vol. 67, no. 6, p. 757, 1995.

[118] N. Tansu and L. J. Mawst, “Design analysis of 1550-nm GaAsSb-(In)GaAsN type-II quantum-well laser active regions,” *IEEE J. Quantum Electron.*, vol. 39, no. 10, pp. 1205–1210, 2003.

[119] J.-Y. Yeh *et al.*, “Long wavelength emission of InGaAsN/GaAsSb type-II ‘W’ quantum wells,” *Appl. Phys. Lett.*, vol. 88, no. 5, p. 51115, 2006.

[120] M. Peter *et al.*, “Realization and modeling of a pseudomorphic (GaAsSb-InGaAs)/GaAs bilayer-quantum well,” *Appl. Phys. Lett.*, vol. 67, no. 18, p. 2639, 1995.

[121] R. Kaspi, A. Ongstad, G. C. Dente, J. Chavez, M. L. Tilton, and D. Gianardi, “High power and high brightness from an optically pumped InAs/InGaSb type-II midinfrared laser with low confinement,” *Appl. Phys. Lett.*, vol. 81, no. 3, p. 406, 2002.

[122] C. L. Felix *et al.*, “High-temperature 4.5 μm type-II quantum-well laser with Auger suppression,” *IEEE Photon. Technol. Lett.*, vol. 9, no. 6, pp. 734–736, 1997.

[123] C. H. Chang *et al.*, “Low-Threshold Short-Wavelength Infrared InGaAs/GaAsSb ‘W’-Type QW Laser on InP Substrate,” *IEEE Photon. Technol. Lett.*, vol. 27, no. 3, pp. 225–228, 2015.

[124] J. F. Klem, O. Blum, S. R. Kurtz, I. J. Fritz, and K. D. Choquette, “GaAsSb/InGaAs type-II quantum wells for long-wavelength lasers on GaAs substrates,” *J. Vac. Sci. Technol., B*, vol. 18, no. 3, p. 1605, 2000.

[125] S.-W. Ryu and P. D. Dapkus, “Room temperature operation of type-II GaAsSb/InGaAs quantum well laser on GaAs substrates,” *Electron. Lett.*, vol. 38, no. 12, pp. 564–565, 2002.

[126] S. Gies *et al.*, “Band offset in (Ga,In)As/Ga(As,Sb) heterostructures,” *arXiv preprint arxiv:1610.03699 (submitted 2016).*

[127] M. Kudo, K. Ouchi, J. Kasai, and T. Mishima, “Low-lattice-strain long-wavelength GaAsSb/GaInAs type-II quantum wells grown on GaAs substrates,” *Jpn. J. Appl. Phys.*, vol. 41, no. 10A, p. L1040, 2002.

[128] P. Dowd *et al.*, “Long wavelength (1.3 and 1.5 μm) photoluminescence from InGaAs/GaPAsSb quantum wells grown on GaAs,” *Appl. Phys. Lett.*, vol. 75, no. 9, p. 1267, 1999.

[129] W. W. Chow, O. B. Spahn, H. C. Schneider, and J. F. Klem, “Contributions to the large blue emission shift in a GaAsSb type-II laser,” *IEEE J. Quantum Electron.*, vol. 37, no. 9, pp. 1178–1182, 2001.

[130] W. W. Chow and H. C. Schneider, “Charge-separation effects in 1.3 µm GaAsSb type-II quantum-well laser gain,” *Appl. Phys. Lett.*, vol. 78, no. 26, p. 4100, 2001.

[131] C. Berger, “Microscopic Theory of Semiconductor Laser Material Systems,” PhD thesis, Philipps-Universität Marburg, 2016.

[132] C. Fuchs, A. Beyer, K. Volz, and W. Stolz, “MOVPE growth of (GaIn)As/Ga(AsSb)/(GaIn)As type-II heterostructures on GaAs substrate for near infrared laser applications,” *J. Cryst. Growth*, accepted 2016.

[133] S. Gies *et al.*, “Excitonic transitions in highly efficient (GaIn)As/Ga(AsSb) type-II quantum-well structures,” *Appl. Phys. Lett.*, vol. 107, no. 18, p. 182104, 2015.

[134] C. Berger *et al.*, “Novel type-II material system for laser applications in the near-infrared regime,” *AIP Advances*, vol. 5, no. 4, p. 47105, 2015.

[135] C. Möller *et al.*, “Type-II vertical-external-cavity surface-emitting laser with Watt level output powers at 1.2 µm,” *Appl. Phys. Lett.*, vol. 108, no. 7, p. 71102, 2016.

[136] S. Ranta, M. Tavast, T. Leinonen, N. Van Lieu, G. Fetzer, and M. Guina, “1180 nm VECSEL with output power beyond 20 W,” *Electron. Lett.*, vol. 49, no. 1, pp. 59–60, 2013.

[137] ISO 11146 Lasers and laser-related equipment – Test methods for laser beam parameters – Beam width, divergence, angle and beam propagation factor, 1999.

List of contributions

Publications

B. Heinen, C. Möller, K. Jandieri, B. Kunert, M. Koch, and W. Stolz, "The Thermal Resistance of High-Power Semiconductor Disk Lasers," IEEE J. Quantum Electron. **51**, 1–9 (2015).

C. Fuchs, C. Berger, C. Möller, M. J. Weseloh, S. Reinhard, J. Hader, J. V. Moloney, S. W. Koch, and W. Stolz, "Electrical injection type-II (GaIn)As/Ga(AsSb)/(GaIn)As single W-quantum well laser at 1.2 µm," Electron. Lett. **55**, 1875-1877 (2016).

C. Berger, C. Möller, P. Hens, C. Fuchs, W. Stolz, S. W. Koch, A. Ruiz Perez, J. Hader, and J. V. Moloney, "Novel type-II material system for laser applications in the near-infrared regime," AIP Adv. **5,** 47105 (2015).

C. Jansen, S. Priebe, C. Möller, M. Jacob, H. Dierke, M. Koch, and T. Kurner, "Diffuse Scattering From Rough Surfaces in THz Communication Channels," IEEE Trans. Terahertz Sci. Technol. **1**, 462–472 (2011).

C. Lammers, M. Stein, C. Berger, C. Möller, C. Fuchs, A. Ruiz Perez, A. Rahimi-Iman, J. Hader, J. V. Moloney, W. Stolz, S. W. Koch, and M. Koch, "Gain spectroscopy of a type-II VECSEL chip," Appl. Phys. Lett. **109**, 232107 (2016).

C. Möller, F. Zhang, C. Fuchs, C. Berger, A. Rehn, A. Ruiz Perez, A. Rahimi-Iman, J. Hader, M. Koch, J. V. Moloney, S. W. Koch, and W. Stolz, "Fundamental transverse mode operation of a type-II vertical-external-cavity surface-emitting laser at 1.2 µm," (*accepted* 2016)

C. Möller, C. Fuchs, C. Berger, A. Ruiz Perez, M. Koch, J. Hader, J. V. Moloney, S. W. Koch, and W. Stolz, "Type-II vertical-external-cavity surface-emitting laser with Watt level output powers at 1.2 µm," Appl. Phys. Lett. **108**, 71102 (2016).

F. Zhang, B. Heinen, M. Wichmann, C. Möller, B. Kunert, A. Rahimi-Iman, W. Stolz, and M. Koch, "A 23-watt single-frequency vertical-external-cavity surface-emitting laser," Opt. Express **22**, 12817 (2014).

F. Zhang, M. Gaafar, C. Möller, W. Stolz, M. Koch, and A. Rahimi-Iman, "Dual-Wavelength Emission From a Serially Connected Two-Chip VECSEL," IEEE Photon. Technol. Lett. **28**, 927–929 (2016).

F. Zhang, C. Möller, W. Stolz, A. Rahimi-Iman, S. W. Koch and M. Koch, "Impact of detuning on the performance of VECSELs," (*submitted* 2016)

M. Gaafar, C. Möller, M. Wichmann, B. Heinen, B. Kunert, A. Rahimi-Iman, W. Stolz, and M. Koch, "Harmonic self-mode-locking of optically pumped semiconductor disc laser," Electron. Lett. **50**, 551 (2014).

M. Gaafar, D. A. Nakdali, C. Möller, K. A. Fedorova, M. Wichmann, M. K. Shakfa, F. Zhang, A. Rahimi-Iman, E. U. Rafailov, and M. Koch, "Self-mode-locked quantum-dot vertical-external-cavity surface-emitting laser," Opt. Lett. **39**, 4623 (2014).

M. Gaafar, P. Richter, H. Keskin, C. Möller, M. Wichmann, W. Stolz, A. Rahimi-Iman, and M. Koch, "Self-mode-locking semiconductor disk laser," Opt. Express **22**, 28390 (2014).

R. Gente, C. Jansen, R. Geise, O. Peters, M. Gente, N. Krumbholz, C. Möller, S. Busch, and M. Koch, "Scaled Bistatic Radar Cross Section Measurements of Aircraft With a Fiber-Coupled THz Time-Domain Spectrometer," IEEE Trans. Terahertz Sci. Technol. **2**, 424–431 (2012).

Conferences

A. Rahimi-Iman, M. Gaafar, D. Al Nakdali, C. Möller, F. Zhang, M. Wichmann, M. Khaled Shakfa, K. A Fedorova, W. Stolz, E. U Rafailov, and M. Koch, "Recent Advances in the Field of Vertical-External-Cavity Surface-Emitting Lasers," SPIE Photonics West: Vertical-exernal-cavity surface-emitting lasers, San Francisco, USA, 02/2016

A. Rahimi-Iman, M. Gaafar, M. Vaupel, C. Möller, F. Zhang, D. Al-Nakdali, K. A. Fedorova, W. Stolz, E. U. Rafailov, and M. Koch, "Self-mode-locked semiconductor disk laser," International Conference on Laser Optics, St. Petersburg, Russia; 06/2016

A. Rahimi-Iman, M. Gaafar, D. Al Nakdali, C. Möller, F. Zhang, M. Wichmann, M. Khaled Shakfa, K. A Fedorova, W. Stolz, E. U Rafailov, and M. Koch, "Recent Advances in the Field of Vertical-External-Cavity Surface-Emitting Lasers," SPIE Photonics West: Vertical-exernal-cavity surface-emitting lasers, San Francisco, USA, 02/2015

C. Lammers, M. Stein, M. Fey, C. Fuchs, C. Möller, A. Ruiz-Perez, C. Berger, A. Rahimi-Iman, J. Hader, J. V. Moloney, S. W. Koch, W. Stolz, and M. Koch, "Time-resolved gain spectroscopy on type-I and type-II VECSEL chips," CLEO: Applications and Technology, San Jose, USA, 01/2016

C. Möller, C. Berger, C. Fuchs, A. Ruiz Perez, S. W. Koch, J. Hader, J. V. Moloney, and W. Stolz, "1.2µm emitting VECSEL based on type-II aligned QWs," SPIE Photonics West: Vertical-exernal-cavity surface-emitting lasers, San Francisco, USA, 03/2016

F. Zhang, M. Gaafar, C. Möller, W. Stolz, M. Koch, and A. Rahimi-Iman, "A serially-connected two-chip VECSEL for dual-wavelength emission," International Conference on Laser Optics, St. Petersburg, Russia, 06/2016

F. Zhang, M. Gaafar, C. Möller, W. Stolz, M. Koch, and A. Rahimi-Iman, "A serially-connected two-chip VECSEL for dual-wavelength emission with high intracavity power," SPIE LASE, San Francisco, USA, 03/2016

F. Zhang, B. Heinen, C. Möller, M. Wichmann, B. Kunert, A. Rahimi-Iman, W. Stolz, and M. Koch, "22W Single-Frequency Vertical-External-Cavity Surface-Emitting Laser," CLEO: Science and Innovations, San Jose, USA, 06/2014

F. Zhang, B. Heinen, C. Möller, M. Wichmann, B. Kunert, A. Rahimi-Iman, S. W. Koch, W. Stolz, and M. Koch, „Single-Frequency Vertical-External-Cavity Surface-Emitting Laser Exceeding 23 W," Asia Communications and Photonics Conference (ACP), Shanghai, China, 11/2014

M. Gaafar, C. Möller, M. Wichmann, B. Heinen, B. Kunert, A. Rahimi-Iman, W. Stolz, and M. Koch, "Passively harmonically self-mode-locked Vertical- External-Cavity Surface-Emitting Laser (VECSEL)," CLEO: Applications and Technology; San Jose, USA, 06/2014

M. Wichmann, C. Möller, M. Stein, A. Rahimi-Iman, S. W. Koch, W. Stolz, and M. Koch, "Power dependent measurements of the emission bandwidth of a vertical-external-cavity surface-emitting laser driven terahertz source," International Conference on Infrared, Millimeter, and THz Waves, Tucson, USA, 09/2014